Radio exploration of the transient sky: Binary mergers and peculiar core-collapse supernovae

by

Arvind Balasubramanian, BS-MS Dual Degree, Masters in Physics

A Dissertation

In

Physics

Submitted to the Graduate Faculty
of Texas Tech University in
Partial Fulfillment of
the Requirements for
the Degree of

DOCTOR OF PHILOSOPHY

Approved

Dr. Alessandra Corsi
Chairperson of the Committee

Dr. Joseph D. Romano

Dr. Varun Bhalerao

Dr. Andrew Whitbeck

Dr. Mark Sheridan
Dean of the Graduate School

August 2022

ACKNOWLEDGMENTS

I begin by expressing my gratitude to my gurus and parents for their blessings and constant support during the course of this thesis.

Dr. Alessandra Corsi, my advisor, has been a great inspiration to me. I have learnt a lot from Dr. Corsi through the course of this degree and it has opened a window into the fascinating universe of radio transients for me. I would also like to thank Dr. Joseph Romano, Dr. Andrew Whitbeck, Dr. Varun Bhalerao and Dr. Eugenio Aulisa for sparing their precious time to serve on my thesis committee and provide me with their valuable guidance.

Lastly, I would like to thank my wonderful colleagues and friends from our department (Manuel, Binod, Zach Cardenas, Zach Brown, Imtiaz, Bilal, Paul, Kavitha, Matteo). It has been an amazing time having fun conversations and playing the occasional game of chess with all of you.

STATEMENTS

Observations and discussion sections in Chapters 2 and 4 are borrowed from published works Balasubramanian et al. (2021b), Balasubramanian et al. (2022) (in review for ApJL) and Balasubramanian et al. (2021a) for which I was the first author. Chapter 3 contains brief discussions of additional projects/publications I have contributed to.

TABLE OF CONTENTS

ABSTRACT

Astrophysical transients are a class of variable sources often associated with some of the most cataclysmic phenomena in the universe, such as compact object (neutron stars and black holes) mergers and explosions of massive stars. Observations over the last few decades have shown that the radio sky is very dynamic on short timescales. Radio studies of transients uniquely unveil key information on the physics at play in these events, as well as important clues on the properties of their surroundings. For example, radio observations of extreme transients are an effective tool to probe particle acceleration in relativistic shocks; characterize the properties (such as speed and energy) of their ejecta; study the mass loss history of pre-supernova progenitors; constrain the density of the insterstellar medium (ISM) in which fast ejecta expand and/or the structure and density of the circumstellar environment; distinguish engine-powered relativistic transients from non-relativistic ones powered by strong circumstellar interaction; and provide hints on the equation of state of neutron stars. Hence, radio observations bring us a complementary view of the transient universe to that obtained through observations at other wavelengths of the electromagnetic spectrum, or via other messengers (such as gravitational waves). This thesis focuses on the detailed study of a few radio transients that are related to the birth of compact objects, either via the merger of other compact objects in binary systems, or via massive star explosions. Specifically, I focus on: (i) GW170817, the first binary neutron star merger to be observed in both gravitational waves and electromagnetic waves, and the late-time search for a kilonova radio afterglow as a tool to characterize the nature of the compact object left over after the merger; (ii) Radio follow-up observations of candidate binary neutron stars mergers identified during the latest observing run of ground-based gravitational wave detectors; (iii) SN 2004dk, a stripped-envelope core-collapse supernova representative of the class of radio-loud massive star explosions in which radio observations can disentangle relativistic ejecta powered by a compact object engine, from non-relativistic strong circumstellar interaction related to the pre-supernova progenitor mass loss history.

LIST OF TABLES

LIST OF FIGURES

Acronyms

BBH	binary black hole
BH	black hole
BNS	Binary neutron star
CSM	circum-stellar medium
EM	electromagnetic
GRB	gamma-ray burst
GW	gravitational wave
ISM	inter-stellar medium
LIGO	Laser Interferometer Gravitational wave Observatory
NS	neutron star
NSBH	neutron star black hole
RMS	root mean square
SN	supernova, pl: SNe
SNR	signal-to-noise-ratio
SSA	Synchrotron Self Absorption
UTC	coordinated universal time

Table of Units

$1\,\mathrm{Jy} = 10^{-26}\,\mathrm{W\,m^{-2}\,Hz^{-1}}$ (Flux density)

$1\,''$ = 1 arcsec = $\frac{1}{3600}$ deg

MJD = Modified Julian Date = No. of days since midnight on November 17, 1858

CHAPTER 1
INTRODUCTION

The term “transient” in the astrophysical context is used to refer to sources that evolve over short timescales - from fractions of seconds to sometimes a few years, as opposed to the longer timescales that characterize e.g., the steady evolution of stars and galaxies (millions to tens of billions of years). Time domain astronomy is a branch of astronomy which deals with the study of the temporal evolution of transient astronomical sources.

Space-based high-energy (X-ray and gamma-ray) instruments such as the Vela Satellites, BATSE, BeppoSAX, *Fermi*, *Swift*, and *Chandra* have played a key role in discovery and characterization of the type of transients that are the subject of this Thesis (see e.g., Charles and Shaw, 2013; Strong et al., 1974; Fishman et al., 1994; de Pasquale et al., 2006; Paciesas et al., 2012; Krimm et al., 2013). The development of CCD (charge-coupled device) technology in the later half of the 20th century and the ability to manufacture efficient and cost effective large CCDs has ushered in a new era for time domain optical astronomy (Charles and Shaw, 2013). This has assisted in the building of telescopes with larger fields of view to monitor larger regions of the sky with a faster cadence (short times between consecutive observations). Nowadays, the study of transients is not just limited to high energy or optical astronomy, with observations from other wavelengths of the electromagnetic (EM) spectrum, as well as other messengers (gravitational waves, GWs, and neutrinos), contributing vital information about the physics at play in these interesting phenomena. The 2020 decadal astronomy survey has declared time-domain astronomy as a priority science area for the next decade (National Academies of Sciences and Medicine, 2021).

Observations of changing objects in the radio sky began with the discovery of pulsating radio sources now termed pulsars. The study of the transient radio sky, in particular, can provide us with invaluable information on the physics at play in some of the most cataclysmic phenomena in the universe. Non-thermal radio emission is particularly well suited for studying fast explosions, and more generally for probing relativistic particles embedded in regions of strong (amplified) magnetic fields (e.g., Bower et al., 2007; Mooley et al., 2013a; Lacy et al., 2020, and references therein). Radio observations at frequencies of a few GHz are also not affected by extinction (the absorption and scattering of electromagnetic radiation by gas and dust), and can provide information that complements optical observations (e.g., Mooley et al., 2016). Radio transients can be broadly classified into two categories based on their emission properties:

- Incoherent or slow transients (minutes to days to years): explosive and accreting sources like supernovae (SNe), gamma ray bursts (GRBs) and counterparts to gravitational wave (GW) sources.
- Coherent or fast transients (milliseconds to seconds): objects like rotating radio transients (RRATs) and fast radio bursts (FRBs).

This Thesis focuses on transients belonging to the first class above (incoherent, slow) and they have been hypothesized to be linked, or directly observed in association with GRBs.

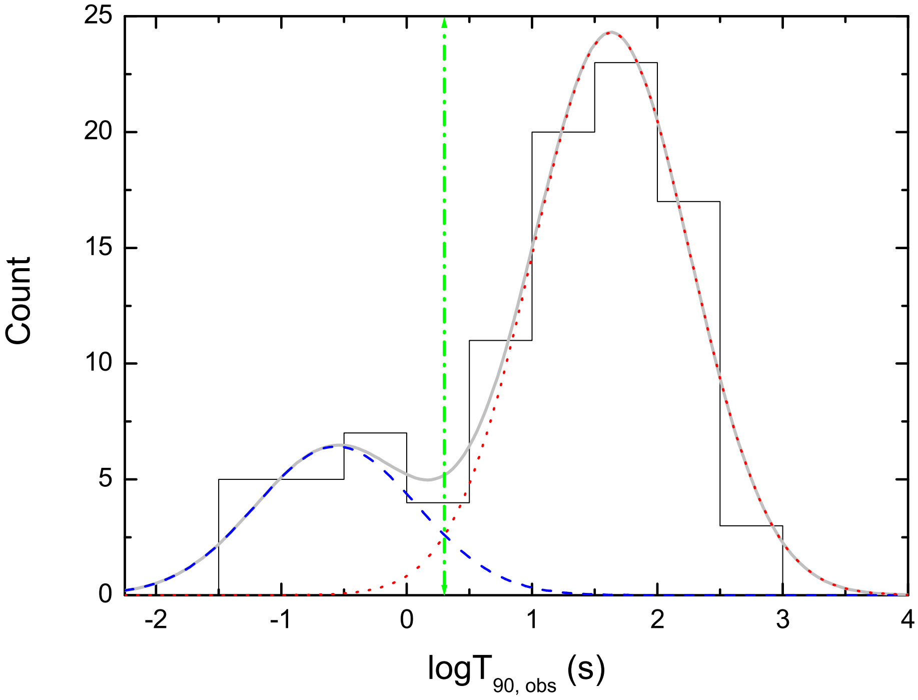

Figure 1.1. Bimodal distribution of the duration ($T_{90,obs}$) of gamma-ray flashes from GRBs observed by the *Swift* observatory. The vertical line is at $T_{90} = 2\,\mathrm{s}$. Figure from Zhang and Choi (2008).

GRBs are some of the most energetic explosions known in the universe, associated with bright flashes of gamma-rays followed by emission in radio-to-X-ray wavelengths from the interaction of the ejecta with the surrounding interstellar medium, known as the afterglow emission (see Mészáros, 2006; Piran, 2004). The duration of the observed gamma-ray emission from GRBs follows a bimodal distribution (e.g., Zhang and Choi, 2008): short GRBs of gamma-ray flash duration $\lesssim 2\,\mathrm{s}$ and long GRBs of gamma-ray flash duration of $\gtrsim 2\,\mathrm{s}$ (see Figure 1.1). Figure 1.1 shows the histogram of the duration ($T_{90,obs}$, duration between when the GRB emits 5% of its total flux to 95%) of GRBs as seen by the *Swift* observatory. While the duration of the gamma-ray flash may not be intrinsic to GRBs, there are attempts to provide physical reasons for the two different categories by referring to different progenitor mechanisms (see Figure 1.2).

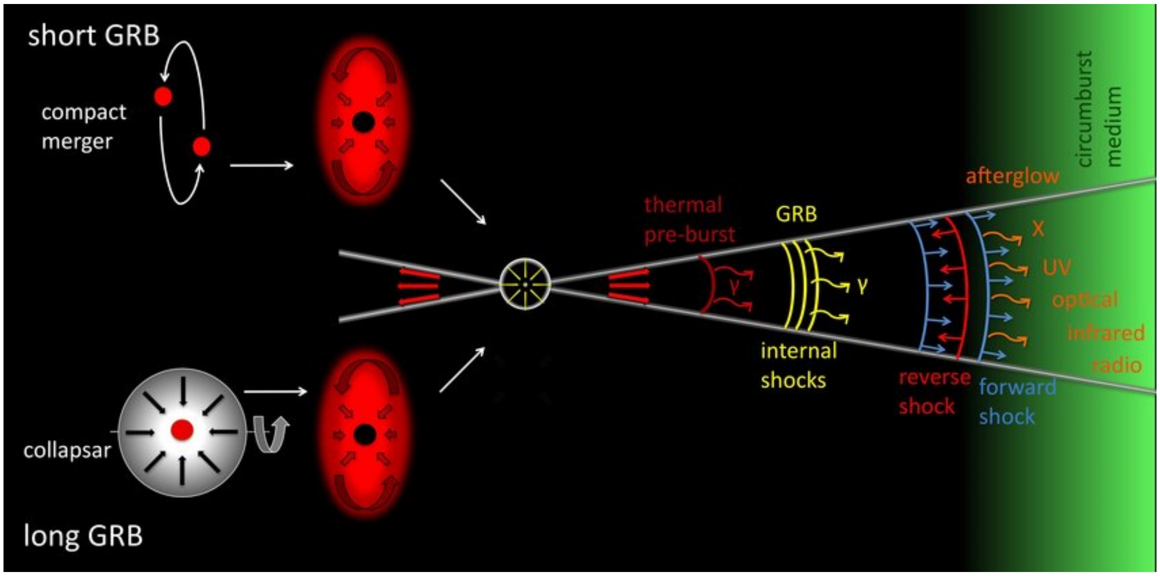

Figure 1.2. The two possible progenitors of GRBs : merger of compact objects resulting in short GRBs and core-collapse SNe resulting in long GRBs. Figure from Gomboc (2012).

The consensus is that the short GRBs are emitted from merging compact objects and long GRBs are emitted from the collapse of a massive star (core-collapse SNe). GW170817, the first confirmed compact object merger to be observed with both gravitational waves and electromagnetic waves, verified that mergers of compact objects emit short GRBs (see Chapter 2). SNe are classified based on their origin (thermonuclear vs core-collapse) and certain features in their spectra. Figure 1.3 shows a flow chart describing the classification method of SNe. The objects of interest here are the core-collapse SNe. They are called core-collapse because the core of the star contracts after sequentially burning its H, He, C, Ne, O and Si layers as the energy of the fusion can no longer counteract gravity. As the star contracts, shock waves that move outward through the stellar material are produced. These shock waves rip apart the star resulting in the SN, leaving behind a highly dense remnant. On the other hand, thermonuclear explosions occur when the fusion to heavier elements heats the core, causing an explosion without collapse of the core.

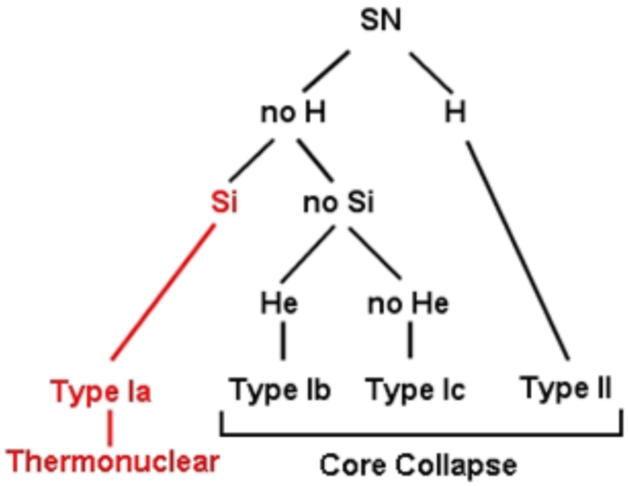

Figure 1.3. Classification of Supernovae. Chart adapted from https://astronomy.swin.edu.au/cosmos/s/supernova+classification.

A rare fraction of core-collapse SNe also power long GRBs with bright radio afterglows (e.g., Chevalier, 1998; Soderberg et al., 2006; Chandra and Frail, 2012; Corsi et al., 2016, and references therein). It is still not clear what separates these special SNe from regular core-collapse SNe.

Many fundamental questions remain unanswered about the physics of GRBs. The general picture is that the catastrophic event (merger or SN) causes a release of large amounts of energy in one or a combination of the following forms: radiation, thermal energy and electromagnetic energy. The right portion of Figure 1.2 shows the well accepted "fireball" model for gamma-ray bursts. During the expansion of the plasma, most of the thermal energy is transferred to baryons, accelerating them to relativistic speeds. If the outflow is not homogeneous, then the expanding plasma is stratified in to several shells, with faster shells on the inside colliding with external slower shells to cause internal shocks. The emission of non-thermal radiation from these shocks is termed as the prompt GRB emission. The exact physical mechanism of this emission is still an active area of research. Eventually, these shocks interact with the material in the surrounding medium producing non-thermal emission (like sychrotron radiation), which is referred to as the EM afterglow emission (see Appendix A for a discussion on synchrotron afterglow radiation). This model also predicts that the emission should fade over time depending on various physical parameters of the matter surrounding the progenitor (e.g., density of the medium, magnetic field strength) and the progenitor itself (e.g., energy injected in the jet). The central engine that drives the GRB can theoretically be a black hole with an accretion disk or a rapidly spinning magnetar (neutron star endowed with strong magnetic fields). The energy dissipation and particle acceleration mechanisms are not fully understood. The reader is referred to Gomboc (2012) for a more complete review of GRBs and open questions regarding them.

1.1 Scientific justification and goals of this work

The goal of this Thesis is to use GHz radio observations of a variety of astrophysical transients to understand the underlying physics and help constrain relevant emission models for their progenitors and ejecta. Specifically, this work focuses on compact object mergers of neutron stars (NSs) and black holes (BHs), and on stripped-envelope core-collapse supernovae (also referred to as type Ibc SNe). As discussed above, these two rather different classes of astrophysical sources share a common observational feature: at least a fraction of them have been associated with GRBs (e.g., Chandra and Frail, 2012). In this context, this thesis is organized as follows:

1. Chapter 2 discusses the radio observations of the binary NS merger, GW170817, that I carried out in Balasubramanian et al. (2021b, 2022), with the goal of better characterizing the properties of its ejecta. Such studies will improve our understanding of binary NS mergers, their ejecta, and remnants. Specifically, the late-time radio follow-up of GW170817 provides clues into the nature of the merger remnant and the equation of state (EoS) of NSs, as well as into particle acceleration theory in relativistic and non-relativistic regimes (e.g., Chevalier, 1998; Sironi et al., 2015, and references therein).

2. Chapter 3 describes my contributions to searches for radio counterparts of selected compact binary merger candidates detected during the third observing run (O3) of LIGO (e.g., Abbott et al., 2020a), to constrain the physics

of their progenitors and ejecta, and their link to short GRBs (Bhakta et al., 2021, Hinna et al. in prep, GW190814 paper in prep). The radio follow-up of O3 LIGO candidate binary merger events was aimed at hunting for other EM+GW discoveries, to further understand the zoo of possible EM counterparts to GWs and inform future searches for such counterparts in upcoming GW observing runs.

3. Chapter 4 describes the work I have carried out on a peculiar stripped-envelope core-collapse SN, SN 2004dk (Balasubramanian et al., 2021a). This work sheds light on the pre-SN mass-loss history, and clarifies the origin of its radio emission as related to interaction of the SN shock waves with the circumstellar medium (CSM) rather than an off-axis GRB jet. The study of radio emission from core-collapse SNe like SN 2004dk is particularly important to understand the pre-SN evolution of massive stars by tracking the mass-loss histories of their progenitors (e.g., Soderberg et al., 2005; Wellons et al., 2012; Palliyaguru and Corsi, 2019; Palliyaguru et al., 2019). This, in turn, can potentially help us understand the dividing line between ordinary core-collapse SNe and long-duration GRBs (Chevalier, 1998; Soderberg et al., 2006; Chandra and Frail, 2012; Corsi et al., 2016). In the future, with more sensitive GW detectors such as Cosmic Explorer (see Reitze et al., 2019a, and references therein), extreme stripped-envelope core-collapse SNe may become sources of interest also for multi-messenger studies (see Reitze et al., 2019b, and references therein).

1.2 A brief introduction to radio interferometry

This section briefly describes the fundamentals of radio interferometry as discussed in Marr et al. (2015). The resolution of a telescope scales as $\theta \sim \lambda/D$ in the diffraction limit, where λ is the wavelength of observation and D is the diameter of the collecting area of the detector. Optical telescopes generally have resolution of the order of 1 arcsec. If we require similar resolution while observing at $\lambda = 10\,\mathrm{cm}$ (radio wavelength), we will require a dish or diameter 20 km! It is not practical to build and maneuver such a large dish to make our high resolution observations. So, an idea to use smaller radio dishes that act in unison to function as a virtual large dish was envisioned. This collection of radio dishes is called a radio interferometer. There are many such radio interferometers in operation around the world (e.g., Janksy Very Large Array, ASKAP). The process of imaging a source using a radio interferometer is known as aperture synthesis or synthesis imaging.

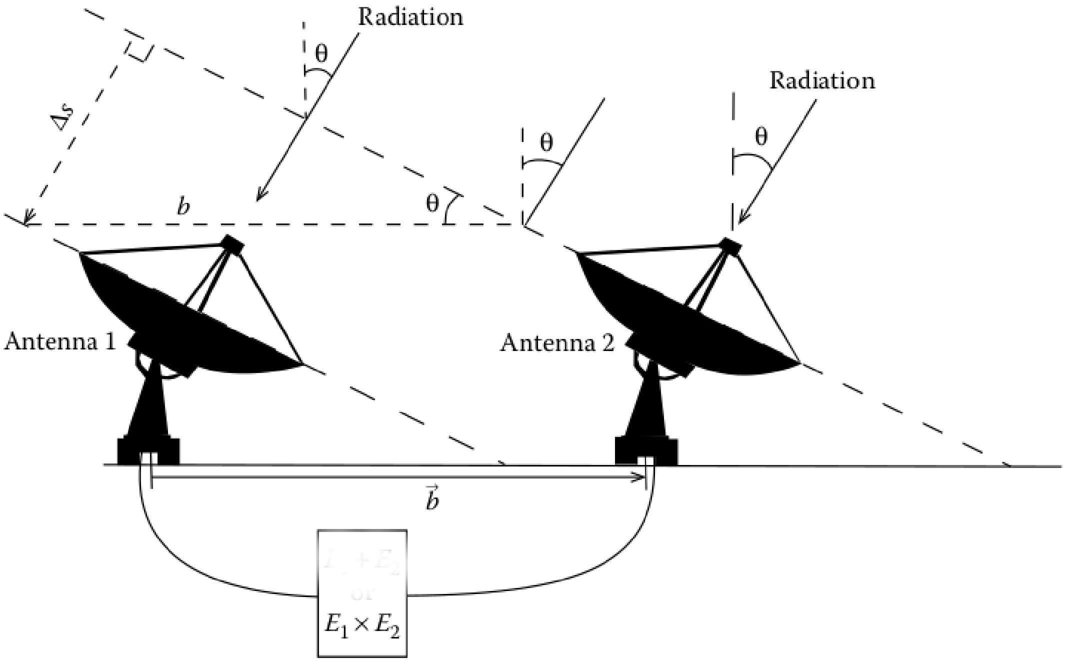

Figure 1.4. Two element interferometer observing a distant point source. Figure from Marr et al. (2015) chapter 5.

I will first discuss the simple case of a two element interferometer. Figure 1.4 shows two antennae, separated by a distance b (baseline), that are observing a distant point source. The data collected by the two dishes (electric fields) are sent to a cross-correlator (box at the bottom of Figure 1.4). The cross-correlator multiplies the electric fields and performs a time average over an integration time (much greater than $1/\nu$ where ν is the observation frequency) and outputs a detected power. The power can be calibrated and converted to flux density (energy per unit area, per unit time, per unit frequency) by observing a flux calibrator (a source that has a known flux density). Let us assume a point source shining at an angle θ to the vertical, as shown in Figure 1.4. The electric fields of frequency ν as seen by

Antenna 1 and Antenna 2 at time t can be expressed as

$$E_1 = E_0 cos(2\pi\nu t) \qquad\qquad E_2 = E_0 cos(2\pi\nu(t+\tau)) \tag{1.1}$$

where τ is the time delay between the receipt of radiation in Antenna 1 and Antenna 2.

$$\tau = \frac{\Delta s}{c} = \frac{b\,\sin\theta}{c} = \frac{b\,\sin\theta}{\lambda\nu} \tag{1.2}$$

Because of the rotation of the earth, the position of the source changes with time as $\theta = \omega_E t$, where ω_E is the angular rotation rate of the earth. So, the time average of the product of E_1 and E_2 is

$$\langle E_1 E_2 \rangle_{Int.time \gg 1/\nu} = \frac{E_0^2}{2}\cos\left(2\pi\frac{\mathrm{b}\,\sin\theta}{\lambda}\right) = \frac{\mathrm{E}_0^2}{2}\cos\left(2\pi\frac{\mathrm{b}\,\sin(\omega_\mathrm{E}\mathrm{t})}{\lambda}\right) \tag{1.3}$$

So, the response of the interferometer to a point source oscillates with time and this response is called the fringe function. This response (R) can then be calibrated and will result in the amplitude of the fringe function being equal to the flux density (F_ν) of the point source.

$$R = F_\nu \cos\left(2\pi\frac{\mathrm{b}\,\sin(\omega_\mathrm{E}\mathrm{t})}{\lambda}\right) \tag{1.4}$$

For a point source located at a small angle $\Delta\Phi$ away from the reference $\theta = \omega_E t$, the response is

$$R = F_\nu \cos\left(2\pi\frac{\mathrm{b}\,\sin(\omega_\mathrm{E}\mathrm{t})}{\lambda} + \Delta\Phi\right) = \mathrm{F}_\nu \cos\left(2\pi\frac{\mathrm{b}\,\sin(\omega_\mathrm{E}\mathrm{t})}{\lambda} + 2\pi\frac{\mathrm{b}\Delta\theta}{\lambda}\right) \tag{1.5}$$

If the telescope can track the reference point, then the first time dependent part of the above equation goes away. Then, the response R is called the visibility function $V_{b/\lambda}$ (a function of b/λ), the flux density F_{nu} is called the visibility amplitude V_A and the phase of the cosine term is called the visibility phase Φ_V.

$$V_{b/\lambda} = F_\nu \cos\left(2\pi\frac{\mathrm{b}\Delta\theta}{\lambda}\right) = \mathrm{V_A}\,\cos\Phi_\mathrm{V} \tag{1.6}$$

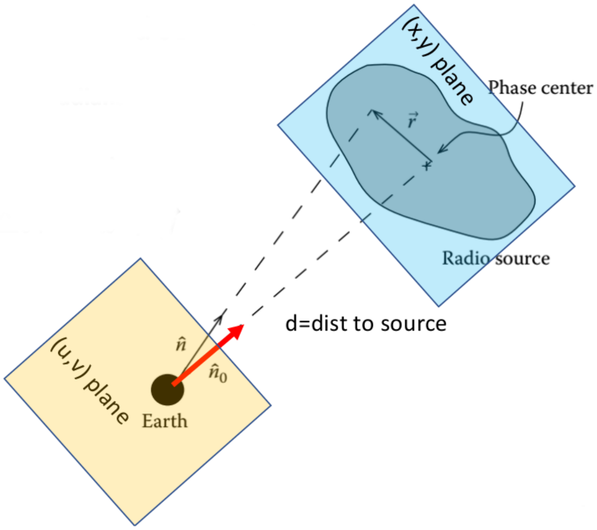

Figure 1.5. The observer plane (u,v) and the source plane (x,y) for a general extended source

The data from any astrophysical object is stored as these visibities. This response can be generalized to case where we are observing an extended object with the baseline vector rotating as function of time due to the rotation of the earth. The visibility (a function of baseline) is the Fourier transform of the sky intensity (function of position on the sky). The visibility is a function on a u (b_x/λ), v(b_y/λ) (baselines on the u,v plane), while the brightness of the source I_ν is a function of x,y (positions on the sky). The final generalized visibility function can be written as

$$V(u,v) = \int\int I_{nu}(x,y)\, e^{2\pi i(ux+vy)}\, dx\, dy \tag{1.7}$$

The observed visibilities can then be converted to brightness as a function of position on the sky I_ν using an inverse Fourier transformation. In practice, we need to have a well sampled u,v plane to perform the inverse Fourier transformation. By utilising the motion of the earth and a large number of antennas, we will be able to sample the u,v plane adequately. The holes in the u-v plane are the reason for artifacts in the final image. The Fourier transform of sampled visibilities yields the true sky brightness convolved with the point spread function, i.e., the “dirty image” is the true image convolved with the “dirty beam”. There are algorithms (e.g., CLEAN algorithm, see Högbom (1974)) that perform a deconvolution of the dirty image to finally give us a map of the sky brightness.

1.3 The Karl G. Jansky Very Large Array (VLA)

The Karl G. Jansky Very Large Array (VLA[1]) is one of the most sensitive radio telescopes currently operating on the Earth. It is a radio interferometer located in Socorro, New Mexico, composed of 27 radio dishes in a Y-shaped configuration that operate in unison to behave like one large virtual dish. These dishes can be moved around to form four different configurations, A through D, with A being the most extended configuration and D being the most compact. Extended configurations allow for large baselines, helping to study the small-scale structure of sources by improving the resolution. On the other hand, compact configurations assist in studying large-scale structures [2]. This instrument is sensitive to radio emission in frequencies ranging from 74 MHz to 45 GHz.

Figure 1.6. The Janksy Very Large Array. Image credits : NRAO/AUI/NSF

---

[1] http://www.vla.nrao.edu/

[2] https://science.nrao.edu/facilities/vla/docs/manuals/oss/performance/resolution

Most observations discussed in this thesis have been obtained from approved programs on the VLA (20A-185, 20B-208, 21B-057, 22A-168, 22A-463; PI: Balasubramanian).

CHAPTER 2
LATE TIME RADIO FOLLOW-UP OF GW170817

2.1 Background

GW events such as the collision of compact objects (e.g., NS-NS mergers) are proposed to be accompanied by emission from across the electromagnetic (EM) spectrum. GW170817 was one such event, the first NS-NS merger to be observed in both GWs (Abbott et al., 2017b) and light by many observatories all around the world (e.g., Coulter et al., 2017; Troja et al., 2017; Margutti et al., 2017a; Hallinan et al., 2017). GW170817 enabled the EM community to test various theoretical predictions made about such mergers over the last 40 years (Metzger, 2017).

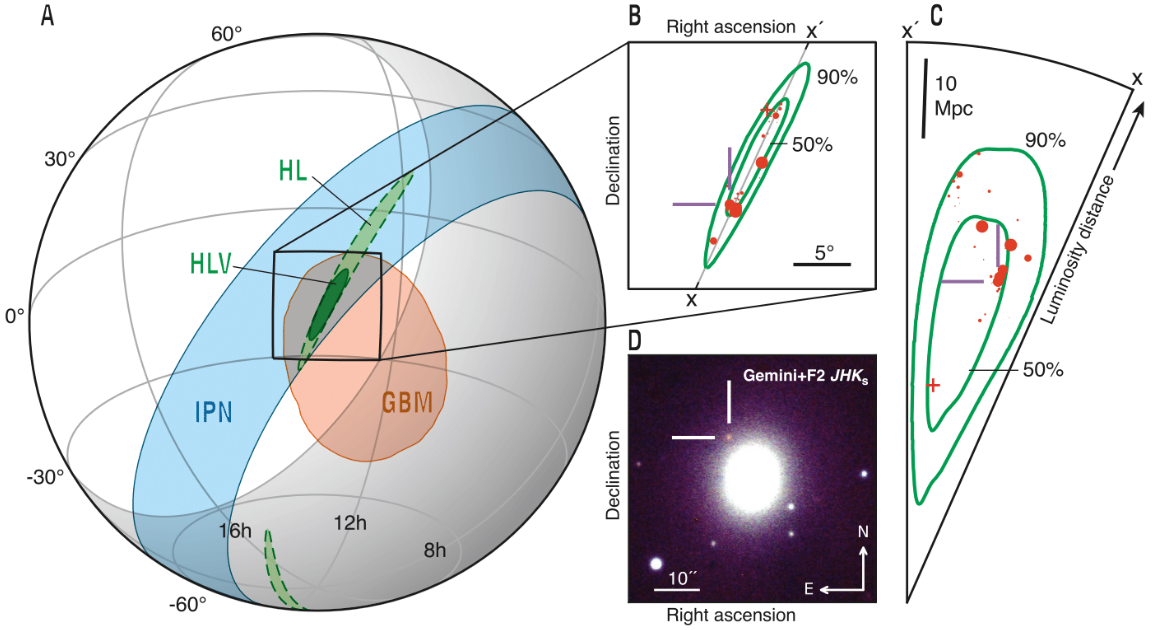

Figure 2.1. Schematic showing the combined effort of localizing GW170817. *A :* localization patches of GW170817 and associated GRB from LIGO (light green), LIGO and Virgo (dark green) and *Fermi* (orange). *B and C :* three-dimensional position of discovered counterpart. *D :* Optical image showing the GW170817 counterpart along with the central bright host galaxy, NGC 4993. Figure from Kasliwal et al. (2017).

GW170817 was discovered at 12:41:04 UTC on 2017 August 17. The GW detection was followed almost immediately (~ 2 s after the merger) by a GRB, confirming that EM waves and GWs travel at the speed of light in vacuum (to better than 1 part in $\approx 10^{16}$, see Abbott et al., 2017c). As the GW localization areas are generally large, the astronomical community began a search for the host galaxy (see Abbott et al., 2017c). The source was located to be associated with the galaxy NGC 4993 by the Swope Supernova team (Coulter et al., 2017), which prompted immediate follow-up observations in wavelength bands across the spectrum.

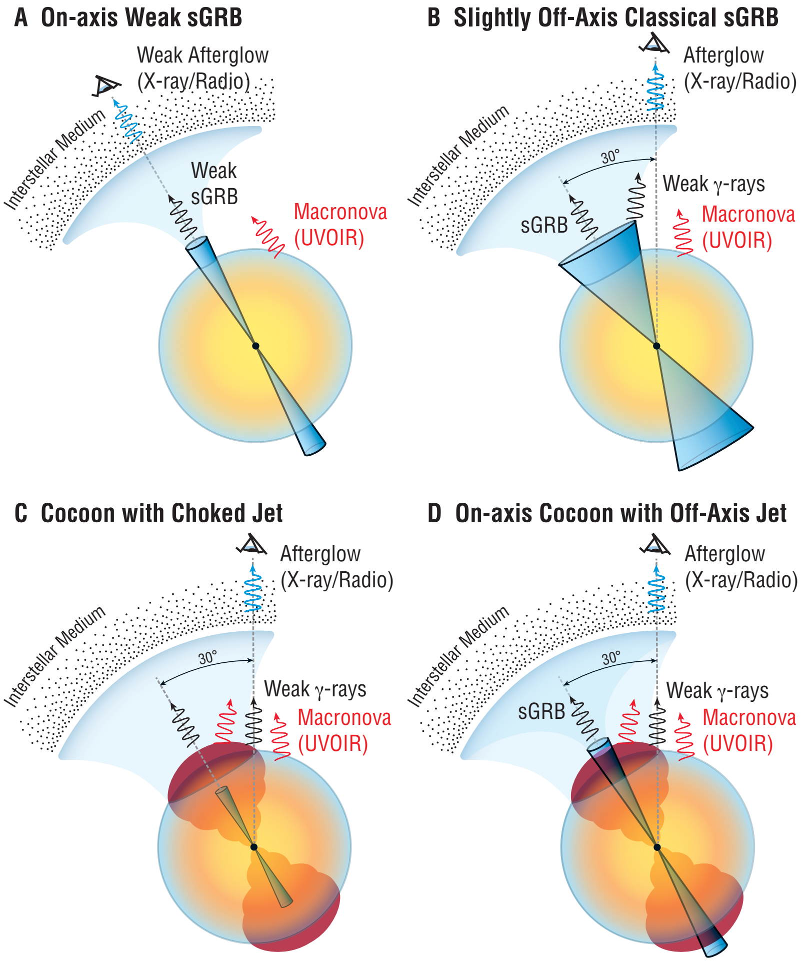

Figure 2.2. Initial proposed models for GW170817. UVOIR refers to UV optical IR emission.Figure from Kasliwal et al. (2017).

Observations of the quasi-thermal UV/optical/IR emission (dubbed kilonova) from the GW170817 slow ($\sim 0.1c - 0.3c$), neutron-rich, isotropic, ejecta were successful in verifying that mergers of NSs in binaries are production sites of heavy elements such as gold and platinum (e.g., Kasliwal et al., 2017; Kasen et al., 2017; Pian et al., 2017; Metzger, 2017). Subsequently, a delayed non-thermal afterglow was also observed in the X-rays (radio) at $\approx 9\,$days ($\approx 12\,$days) after the merger (e.g., Troja et al., 2017; Haggard et al., 2017; Margutti et al., 2017a; Hallinan et al., 2017).

NS-NS mergers have been theorized to be progenitors of short GRBs as discussed above. Given the early electromagnetic emission, astronomers began thinking of models that could explain the observations. Figure 2.2 shows a representation of some such models. In the case of GW170817, it was very unlikely that we are looking into the axis of a weak (low luminosity) short GRB (Model A in Figure 2.2) given that the mass of the ejected material in the direction of the jet deduced from the UV/optical/IR observations were larger than expected. If we were observing a wide short GRB from a direction off the jet axis (Model B in Figure 2.2), the delayed emission in radio and x-ray wavelengths cannot be explained as the non-thermal emission is expected to be seen earlier if the jet slows down sufficiently. So, it was more likely that the jet was surrounded by intermediate velocity ejecta, termed the *cocoon*. As the non-thermal emission continued to rise, it was yet to be determined if the jet was strong enough to have bored through the cocoon and interact with the interstellar medium (ISM) to produce non-thermal emission or not.

Continued radio monitoring of the jet+cocoon emission helped in confirming that the jet was structured with the velocity of the ejecta varying as a function of angle from the jet axis (deduced from the slow rise of the jet+ cocoon emission leading up to the peak, see Figure 2.3) and that the relativistic jet successfully bore through the cocoon (Corsi et al., 2018; Dobie et al., 2018; Alexander et al., 2017; Margutti et al., 2018; Mooley et al., 2018b,d; Hajela et al., 2019; Mooley et al., 2018a; Lazzati et al., 2018; Ren et al., 2020). The jet+cocoon emission can be modeled by the smooth-broken power law model (see Makhathini et al., 2021, and references therein) where, the flux density at a time t and at an observation frequency ν is given by:

$$F(t,\nu) = 2^{1/s}\left(\frac{\nu}{3\,\mathrm{GHz}}\right)^{\beta} F_p \left[\left(\frac{t}{t_p}\right)^{-s\alpha_1} + \left(\frac{t}{t_p}\right)^{-s\alpha_2}\right]^{-1/s} \tag{2.1}$$

where F_p is the peak flux density, t_p is the epoch at which the light curve peaks, s is the smoothness parameter, β is the spectral power law index, α_1 and α_2 represent the power-law index of rise and decay of the light curve.

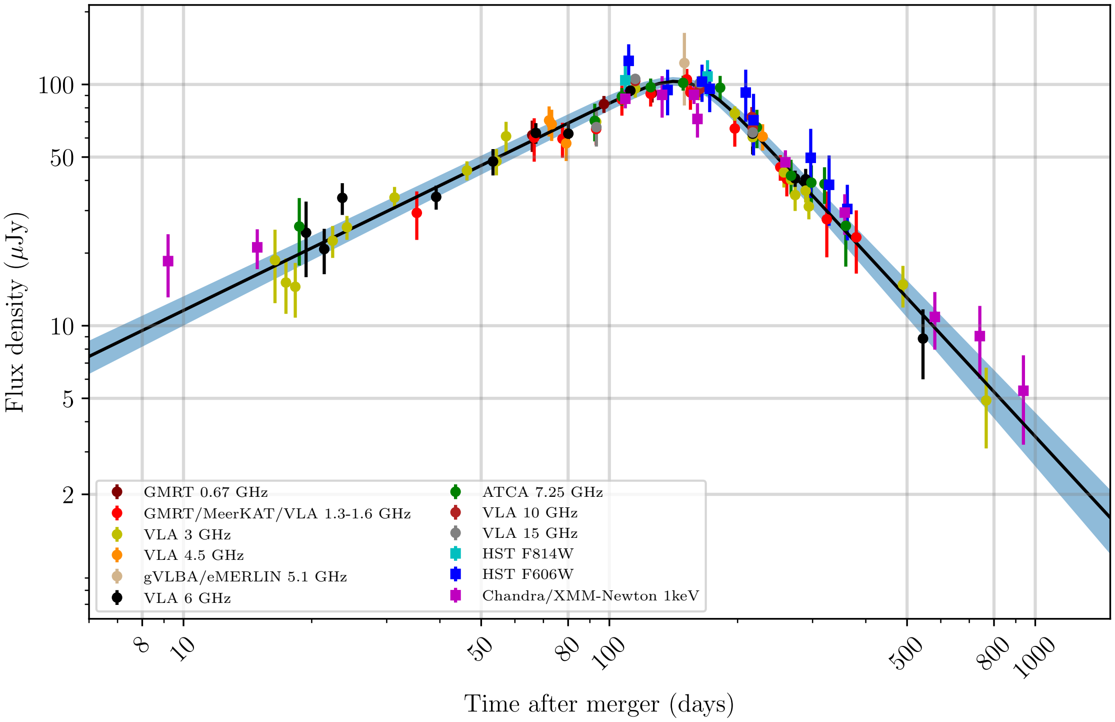

Figure 2.3. Panchromatic light curve of the non-thermal jet+cocoon emission. Figure from Makhathini et al. (2021).

Figure 2.3 shows the multi-wavelength observations of the jet+cocoon emission (all following the same spectral power law index of -0.584!) along with the best fit smooth-broken power law model and the $1\,\sigma$ uncertainty region (see Appendix B).

As seen above, all observational evidence points to Model D in Figure 2.2. The radio observations also helped constrain physical parameters like the angle of observation, jet opening angle and the density of the interstellar medium (Mooley et al., 2018a). At ≈ 2 years since merger, the radio emission from the structured jet has faded below sensitivities that can be achieved with a few hours of observation with the VLA (Makhathini et al., 2021). Several theoretical scenarios, however, predict the possible emergence of detectable electromagnetic emission associated with the afterglow of the kilonova ejecta itself at late times ($\sim$ a few years since merger. See e.g., Nakar and Piran, 2011; Piran et al., 2013; Hotokezaka and Piran, 2015; Kathirgamaraju et al., 2019; Hotokezaka et al., 2018; Margalit and Piran, 2020). Indeed, numerical simulations show that during the NS-NS merger, a modest fraction of a solar mass is ejected from the system, and the total ejecta mass and velocity distribution of such ejecta depend on the total mass, mass ratio, and the nuclear equation of state (EoS) of the compact objects in the binary. While optical-UV observations are mostly sensitive to the low-end of the ejecta velocity distribution, radio (and X-rays) can probe the fastest moving ejecta tail, shedding light on whether NS-NS ejecta are broadly distributed in energy and velocity (as simulations seem to suggest) and providing indirect constraints on the nuclear EoS.

2.2 Search for GW170817 kilonova afterglow 3.5 years after merger

Motivated by the above theoretical/simulated predictions of the kilonova afterglow, we carried out late time observations of the GW170817 field with the VLA. In our publication Balasubramanian et al. (2021b), we discuss the following observations of GW170817 that we carried out at the epoch of 3.5 years after the merger.

2.2.1 Observations

Radio observations of the GW170817 field were carried out with the VLA on the dates listed in Table 2.1 at S band (2–4 GHz, nominal central frequency of 3 GHz) with the array in its B (September 2020) and A configurations (December 2020 - February 2021). These are the most extended configurations of the VLA, which allows us to get the highest resolution images. Each observation was calibrated in `CASA` (McMullin et al., 2007b) using the automated VLA calibration pipeline. The calibrated data were then manually inspected for further radio frequency interference (RFI) excision. We interactively imaged each observation using the `CASA` task `tclean` with one Taylor term (`nterms=1`) and robust weighting (`robust=0.5`), and derived the rms measurements (root-mean-square flux density) using `imstat`. Table 2.1 lists the rms sensitivity reached in each observation, estimated within a region of 20 synthesized beams around the position of GW170817 (α = 13h09m48.069s, $\delta = -23$d22m53.39s, J2000; Mooley et al., 2018a). We find no significant ($> 3\times$rms) excess in a region of one synthesized beam around the position of GW170817 in any of the individual images. Next, we co-added and interactively imaged as above (`nterms=1` and `robust=0.5`) all A-configuration 3 GHz VLA observations listed in Table 2.1. An rms of 1.3 μJy was reached at 2.8 GHz (Table 2.2) within a region of size approximately equal to 20 synthesized beams centered on the position of GW170817. Within one synthesized beam centered on the location of GW170817, we measure an `imstat` peak flux density value of $\approx 2.8\,\mu$Jy at 2.8 GHz. With this procedure, several of the bright, extended sources present in the field left substantial deconvolution residuals. Thus, to mitigate the effects of deconvolution residuals, test the robustness of our measurement, and further improve our sensitivity, we imaged all 3 GHz data (both A and B configurations of the VLA) listed in Table 2.1 non-interactively with two Taylor terms (`nterms=2`), robust weighting (`robust=0.5`), single phase-only selfcal (solution interval of 4 minutes), and a cleaning threshold of 4 μJy. This yielded an image rms noise of 0.99 μJy (in a region of size equal to 20 synthesized beams around the position of GW170817; theoretical thermal noise $\approx 0.85\,\mu$Jy) and a peak flux density value of 2.86 μJy (Table 2.2) within one synthesized beam centered on the location of GW170817.

A late-time VLA observation of the GW170817 field was also carried out in U band (nominal central frequency of 15 GHz) on 10 February 2021 (Table 2.1). We calibrated this dataset and interactively imaged the field (with `nterms=1` and `robust=0.5`). No significant emission is found at the location of GW170817 (Table 2.2). The rms measured in a region of size equal to 20 synthesized beams centered around the position of GW170817 is of $\approx 1.9\,\mu$Jy at 15 GHz.

Table 2.1. VLA late-time observations of the GW170817 field at 3.5 years since merger. See text for details on rms measurements.

Date (UT)	ν (GHz)	VLA config.	Time on-source (hr)	rms (μJy)	VLA program	PI	Nominal synth. beam($''$)
2020 Sep 19	3.0	B	2 h43 m24 s	4.6	20A-185	Balasubramanian	2.1
2019 Sep 20	3.0	B	2 h43 m27 s	5.8	20A-185	Balasubramanian	2.1
2020 Dec 15	3.0	A	3 h24 m14 s	3.5	SL0449	Margutti	0.65
2020 Dec 27	3.0	A	3 h24 m14 s	3.3	SL0449	Margutti	0.65
2021 Jan 10	3.0	A	2 h41 m34 s	3.7	20B-208	Balasubramanian	0.65
2021 Jan 16	3.0	A	2 h38 m34 s	3.6	20B-208	Balasubramanian	0.65
2021 Feb 02	3.0	A	3 h24 m16 s	3.3	SM0329	Margutti	0.65
2021 Feb 04	3.0	A	2 h38 m38 s	4.1	20B-472	Corsi	0.65
2021 Feb 05	3.0	A	2 h41 m41 s	4.0	20B-472	Corsi	0.65
2021 Feb 06	3.0	A	2 h41 m34 s	3.8	20B-472	Corsi	0.65
2021 Feb 08	3.0	A	2 h41 m36 s	4.0	20B-472	Corsi	0.65
2021 Feb 10	15.0	A	2 h40 m52 s	1.9	SM0329	Margutti	0.13

Table 2.2. Results for the co-added late-time radio observations of GW170817 at the epoch of 3.5 years. See text for discussion.

Date (UT)	Epoch (days)	ν (Hz)	F_ν (μJy)	σ_ν (μJy)	Instrument	Reference
2020 Dec 15 - 2021 Feb 08	1243	2.8×10^9	2.8	1.1-1.3	VLA A	This work
2020 Sep 19 - 2021 Feb 08	1199	3.0×10^9	2.86	0.99	VLA A&B	This work
2020 Dec 10 - 2021 Jan 27	1234	2.41×10^{17}	1.70×10^{-4}	0.45×10^{-4}	Chandra	This work

2.2.2 Results and Conclusions

As is evident from Figure 2.4, our late-time radio observations (orange data point in gray shaded region) of GW170817 do not provide evidence for radio emission in excess to what is expected from the very late time tail of a structured jet afterglow model (black solid line). The X-ray observations (purple data point in gray shaded region), on the other hand, suggest a more pronounced statistical fluctuation or the possible emergence of a new component at higher frequencies (bottom panel in Figure 2.4).

The radio-to-X-ray spectral index as derived from the measured ratio of the late-time radio-to-X-ray flux densities (see Table 2.2) is $\Gamma_{\rm radio-X} + 1 = -0.535 \pm 0.024$, within $\approx 2.1\sigma$ of the value adopted in Figure 2.4 (-0.584 ± 0.002) derived by Makhathini et al. (2021). The current measurements still carry too large uncertainties for claiming any clear evidence for a change in spectral behavior at late times. It may be possible however that the non-detection of a radio re-brightening associated with a kilonova afterglow, together with the tentative X-ray excess, suggest a flattening (reduce is the negative spectral index value) of the radio-to-X-ray spectrum at late times.

In general terms, it is not difficult to envision a scenario in which the electron index ($p = -2\Gamma - 1$) for the ejecta responsible for the late-time X-ray excess differs from the one used to model the structured jet afterglow at earlier times ($p = 2.07 - 2.14$; Makhathini et al., 2021). The predictions of Fermi particle acceleration imply that the power-law index p expected at non-relativistic shock speeds is close to $p \approx 2$, while at ultra-relativistic velocities one can have $p \approx 2.2$ (e.g., Sironi et al., 2015, and references therein). Thus, a flattening of the radio-to-X-ray spectral index in GW170817, if confirmed by further follow-up, could support the idea that a non-relativistic ejecta component is starting to dominate the emission.

In addition to the the above results, theoretical predictions for particle acceleration, non-relativistic ejecta observed in radio-emitting core-collapse SNe typically have $p = 2.5 - 3.2$ (e.g., Chevalier, 1998), pointing to steeper radio-to-X-ray spectra than that suggested by the X-ray excess observed in GW170817. Cases where a

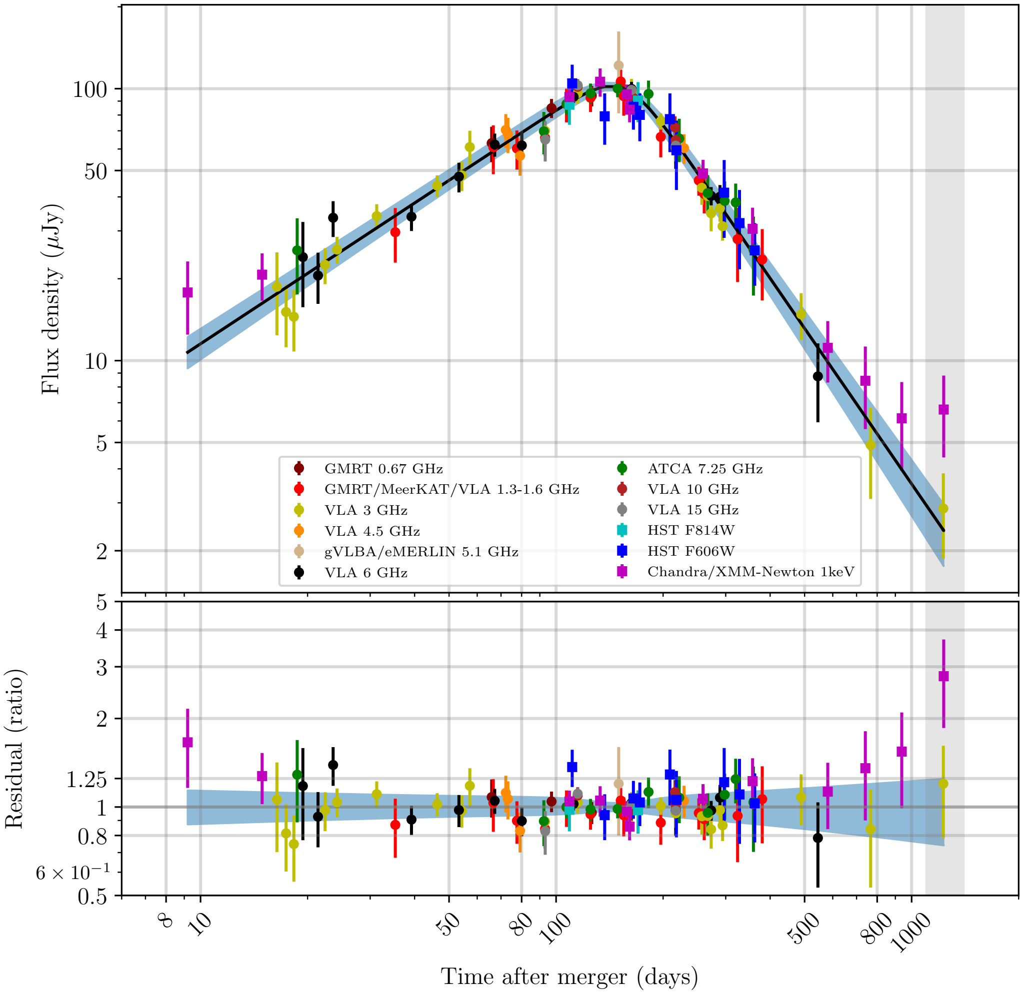

Figure 2.4. Comprehensive 3 GHz light curve of GW170817 as presented in our recent work Makhathini et al. (2021), which includes data from Fong et al. (2019); Ghirlanda et al. (2019); Nynka et al. (2018), together with our latest measurement in the radio (3 GHz, latest yellow data point in the grey, shaded region) and X-rays (latest purple data point in the grey, shaded region) extrapolated to 3 GHz using the spectral index derived in Makhathini et al. (2021). The best fit structured jet model for GW170817 is also plotted (top panel, black line) along with the associated 1σ error region (blue shaded region). As evident from the lower panel, our radio measurement is compatible with the tail of the GW170817 jet within the large errors. On the other hand, the X-rays show a $\sim 2\,\sigma$ excess and could indicate the onset of a new component (Hajela et al., 2020a, 2021b; Troja et al., 2020).

transition of the ejecta from the relativistic to the non-relativistic regime has been observed include GRB 030329 (e.g., Frail et al., 2005; van der Horst et al., 2008) and TDE Swift J1644+57 (Cendes et al., 2021). These two cases pointed to a slowly-increasing or constant value of p in the relativistic-to-non-relativistic transition, which again would correspond to a spectral steepening rather than a spectral flattening.

One key difference between GW170817 and previously observed non-relativistic flows is that we have seen a single power-law spectrum from radio, optical, and X-rays, i.e., synchrotron radiation from electrons with different Lorentz factors in many orders of magnitude. In this case, the spectral index should represent p. On the other hand, in other non-relativistic flows, we often determine p from the radio spectra closer to the minimum Lorentz factor γ_m of the electron energy distribution, where the synchrotron emission may be dominated by thermal electrons around the typical Lorentz factor rather than accelerated electrons (e.g., Park et al., 2015; Maeda, 2013). Thus, GW170817 offers an opportunity to test particle acceleration theory, and continued monitoring from radio-to-X-rays is key to this end. We also note that continued X-ray observations may offer an opportunity to probe the evolution of the cooling frequency in the Newtonian limit, when $\nu_\mathrm{c} \propto \beta^{-3}t^{-2}$ (Hotokezaka et al., 2018), and thus constrain β (velocity of the ejecta in units of $\boldsymbol{c}$) and the kinetic energy of the fast tail of the ejecta (see also Linial and Sari, 2019).

An alternative explanation for the excess in X-rays (as compared to the radio) observed in GW170817 might be the possibility of a Compton echo of the X-rays from the prompt emission of GRB 170817A, scattering off surrounding dust (Beniamini et al., 2018). Given currently large uncertainties in the X-ray result, hereafter we focus on the constraints that the lack of a radio excess set on kilonova ejecta models.

Following Kathirgamaraju et al. (2019), the kilonova blast wave drives a shock through the interstellar medium, resulting in synchrotron emission. Electrons are accelerated to a power-law distribution of Lorentz gamma factors $\gamma_e > \gamma_{e,m}$, with power-law index p. The energy in the kilonova blast wave is distributed as $E(>\beta\gamma) \propto (\beta\gamma)^{-\alpha}$ (with γ the Lorentz factor of the shocked fluid) and normalized to the total energy E at some minimum velocity β_0 such that $E(>\beta_0\gamma_0) = E$. It is reasonable to assume that radio (GHz) observations are in between the minimum frequency, ν_m (corresponding to γ_m, see Nakar and Piran, 2011), and the cooling frequency, ν_c. In this case, the kilonova peak flux density reads (Nakar and Piran, 2011):

$$F_{\nu,\mathrm{pk}} \approx (1522\,\mu\mathrm{Jy})\,\epsilon_{\mathrm{e},-1}^{p-1}\,\epsilon_{\mathrm{B},-3}^{\frac{p+1}{4}}\,n_{-2}^{\frac{p+1}{4}}\,\beta_0^{\frac{5p-7}{2}}\,E_{51}\,\nu_{9.5}^{\frac{1-p}{2}}\,d_{26}^{-2}, \tag{2.2}$$

where $Q_x = Q/10^x$ is followed for all quantities Q (all expressed in cgs units); ϵ_B and ϵ_e are the fractions of the total energy in the magnetic field and electrons respectively; n, the number density of the medium; d is the distance to the source; the normalization constant is calculated for $p = 2.1$. The time at which the kilonova afterglow emission peaks can be calculated as (Kathirgamaraju et al., 2019):

$$t_\mathrm{dec} = t_\mathrm{pk} \approx (3.3\mathrm{yr})\left(\frac{E_{\mathrm{iso},51}}{n_{-2}}\right)^{\frac{1}{3}}\beta_0^{-\frac{2}{3}}\left(\frac{2+\alpha}{\beta_0(5+\alpha)}-1\right). \tag{2.3}$$

where E_iso is the isotropic equivalent energy of the blast wave. The blast wave can be approximated to be mildly relativistic before this peak, and therefore the rising part of the kilonova ejecta light curve can be easily modeled as (see Kathirgamaraju et al., 2019, and references therein):

$$F_{\nu,\mathrm{KN}}\left(t\right) = F_{\nu,\mathrm{pk}}\left(\frac{t}{t_\mathrm{pk}}\right)^{s}, \tag{2.4}$$

where:

$$s = \frac{3\alpha - 6(p-1)}{8+\alpha}. \tag{2.5}$$

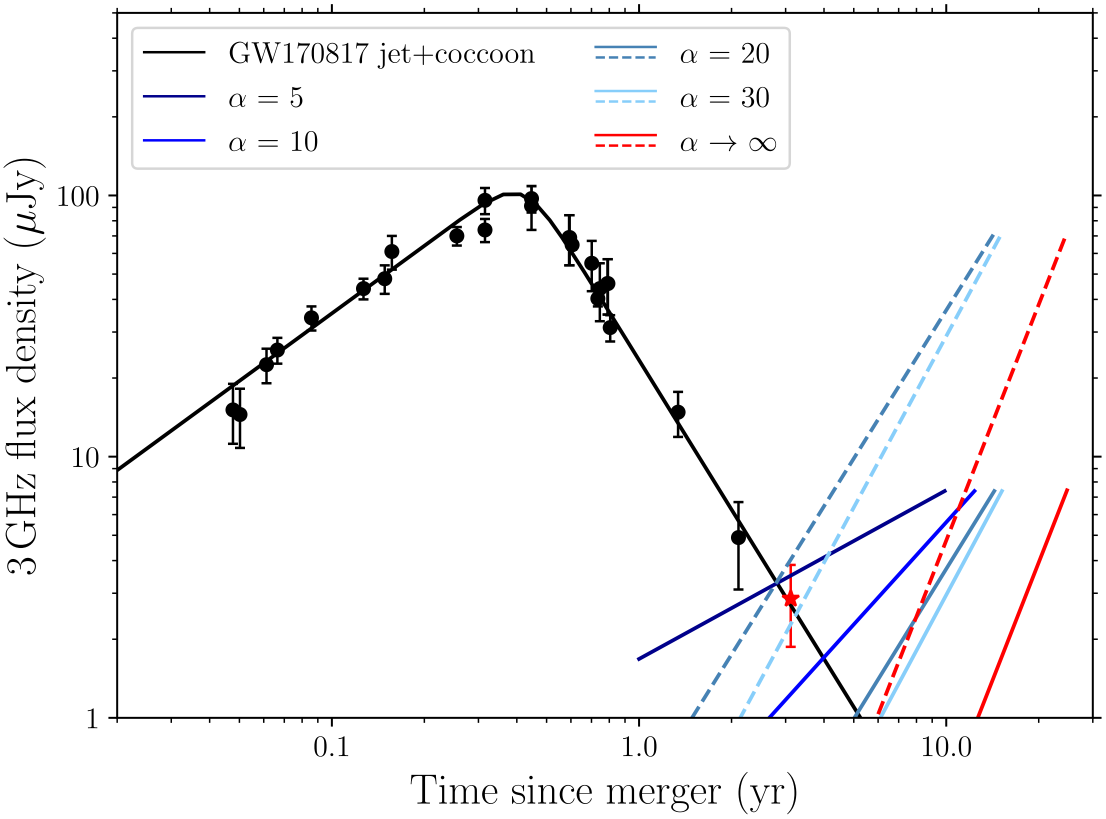

Figure 2.5. 3 GHz radio light curve of GW170817 with our recent radio measurement (red star) along with predictions for the rising part of the kilonova afterglow light curve as a function of α (see §2.4) with the assumption that the minimum speed of the ejecta is $\beta_0 = 0.3$. The solid lines assume $p = 2.1$, $\epsilon_e = 7.8 \times 10^{-3}$, $\epsilon_B = 9.9 \times 10^{-4}$, $n = 9.8 \times 10^{-3}\mathrm{cm}^{-3}$ (as in Makhathini et al., 2021) and $\alpha = 5, 10, 20, 30, \infty$. These values of α are all compatible with our latest radio measurement (red star), while smaller values of α would produce radio emission in excess to it. For comparison, the dashed lines show the case $\epsilon_e = 10^{-1}$, $\epsilon_B = 10^{-3}$, $n = 10^{-2}\mathrm{cm}^{-3}$, $p = 2.2$ (as in Kathirgamaraju et al., 2019), with $\alpha = 20, 30, \infty$ (see text for discussion.)

In Figure 2.5, we plot the rising portion (as discussed by the equations above) the 3 GHz kilonova light curves obtained following the above prescriptions, and setting $\beta_0 = 0.3$. This choice is motivated by the fact that observations in UV/optical/IR of the early kilonova, which only probe the slowest-moving material, point to speeds of $\sim 0.1c - 0.3c$. Since we expect the radio to probe the fastest tail of the kilonova ejecta, we consider $\beta_0 \sim 0.3$ a reasonable choice. We note however that smaller values of β_0, though unlikely, would shift the radio light curve peak to later times, thus allowing for less steep values of α. We set $E_{\rm iso} = 10^{51}$ erg, $d = 40\,$Mpc, while varying the power-law index α of the energy-speed distribution of the kilonova ejecta. The solid lines correspond to the choice $p = 2.1$, $\epsilon_e = 7.8 \times 10^{-3}$, $\epsilon_{\rm B} = 9.9 \times 10^{-4}$ $n = 9.8 \times 10^{-3} {\rm cm}^{-3}$ as derived from the modeling of the earlier-time panchromatic afterglow of the GW170817 structured jet (Makhathini et al., 2021). For comparison, the dashed lines show the case $\epsilon_e = 10^{-1}$, $\epsilon_{\rm B} = 10^{-3}$ $n = 10^{-2} {\rm cm}^{-3}$, $p = 2.2$, which corresponds to the generic case discussed in Kathirgamaraju et al. (2019). As evident from this Figure, to explain the absence of a kilonova detection in the radio one needs $\alpha \gtrsim 5$ for the case where the density and micro-physical parameters are set equal to the ones measured for the structured jet afterglow. This constraint on α agrees with the predictions from numerical simulations described in Hotokezaka et al. (2018) and X-ray observations discussed in Hajela et al. (2020b). For the more generic parameters as in Kathirgamaraju et al. (2019), $\alpha \gtrsim 20$.

For an equal mass ratio binary, a steeper energy-velocity distribution at a given $\beta\gamma$ correlates with a stiffer NS EoS for a given cold, non-rotating maximum mass (compare e.g., $SFHo$ and $LS220$ in Figures 1 and 9 of Radice et al., 2018). For EoS with the same stiffness (i.e., with the same radii at NS masses of $1.4\,{\rm M}_{\odot}$), larger values of the cold, non-rotating maximum NS mass also correlate to steeper energy-velocity ejecta distribution (as long as a NS is formed even if for a short timescale of order $\sim 1\,$ms; compare e.g., $BHB\Lambda\phi$ and $DD2$ in Fig. 9 of Radice et al., 2018). On the other hand, if a fast tail exists in the ejecta, one can robustly exclude stiff EoS and relatively high mass ratio scenarios due to the weak or absent core bounce in these scenarios (Nedora et al., 2021b). Taken together, if future radio observations reveal a kilonova afterglow, these trends would favor moderate stiffness and mass ratio models. Given these considerations, the constraints we are setting here on α shed some light on the possible EoS, but cannot uniquely pinpoint it. An independent measurement of β via direct size imaging (once the ejecta becomes bright enough in the radio) together with constraints on α derived from light curve modeling, may help to reduce degeneracies.

2.3 Constraining energy-speed distribution of ejecta and EoS of neutron stars using radio observations of GW170817 4.5 years after merger

We conducted follow-up observations similar to §2.2 at the epoch of 4.5 yr from merger and published our results in Balasubramanian et al. (2022) (in review for ApJL). The following is a summary of the observations and results obtained.

2.3.1 Observations

We carried out radio continuum observations of the GW170817 field with the VLA. Our observations were executed with the standard VLA S band setup, with a nominal central frequency of 3 GHz, and split in 12 observations (each providing approximately 2.5 hours on source) between December 2021 and March 2022. The first four epochs were observed with the VLA in its B configuration, while the subsequent eight epochs were carried out with the array in its most extended A configuration. These observations are listed in Table 2.3. After calibration was performed with the automated VLA calibration pipeline, we manually inspected the data and performed further flagging for radio frequency interference (RFI) as needed. We then imaged the data using the `CASA` (McMullin et al., 2007a) task `tclean` with one Taylor term (`nterms=1`) and robust weighting (`robust=0.5`; see also Balasubramanian et al., 2021b), and derived the sensitivity RMS measurements running `imstat` on the residual images within a circular region of radius equal to 10 nominal synthesized beams[1] around the position of GW170817 ($\alpha = 13\text{h}09\text{m}48.069\text{s}$, $\delta = -23\text{d}22\text{m}53.39\text{s}$, J2000; Mooley et al., 2018a). Because this region may include residuals associated with the host galaxy light (see Figure 2.6), we also list in parentheses in Table 2.3 the RMS values we obtain using a circular region of the same size in a source-free portion of the image. We find no significant ($> 3\times$RMS) excess in a region of one synthesized beam around the position of GW170817 in any of the individual epochs.

Next, we co-add the four B configuration observations, and the eight A configuration observations separately; finally, we co-add the full multiple configuration data set (all in the visibility domain) for a total of 12 observations. The imaging for these co-added datasets was performed similar to what is described above,

---

[1] As recommended by Hancock et al. (2012) and Mooley et al. (2013b).

with the `CASA` task `tclean` but using `nterms=2` to better clean the emission from bright radio sources in the field. To estimate the RMS sensitivity for the co-added observations in the A and B configurations, we conservatively use a circular region of radius 10 times the nominal synthesized beam width of the B configuration, centered on the location of GW170817 in the residual images. We list our findings in Table 2.4. In our deepest co-added image, we reach an RMS sensitivity of $1.1\,\mu$Jy at 3.0 GHz. No emission in excess to 3 times the co-added image RMS is found in a circular region of radius 2.1 arcsec (FWHM of the nominal VLA synthesized beam in B configuration at 3 GHz) around the location of GW170817. Specifically, at the location of GW170817 we measure a 3 GHz flux of $2.1 \pm 1.1\,\mu$Jy. Therefore, we constrain the radio emission from GW170817 to $< 3.3\,\mu$Jy at 4.5 years since merger (see Figure 2.7).

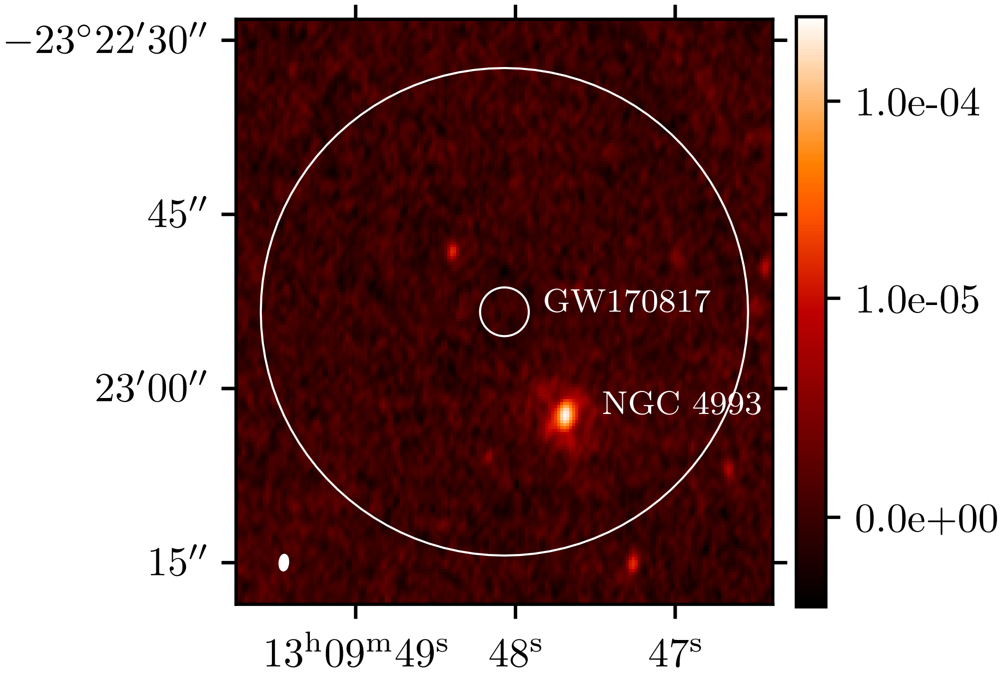

Figure 2.6. Image of the GW170817 field at ≈ 4.5 yrs since merger, as derived from our deepest co-added dataset (see Table 2.4). The small circle has a radius of $2.1''$ and is centered on the position of GW170817. The larger circle has a radius of $21''$, equal to the radius of the circular region used to calculate our RMS sensitivity in the residual image of the field. The host galaxy of GW170817 is enclosed in this larger circular region. Several sources unrelated to GW170817 are also visible. The synthesized beam ellipse is shown in the bottom left. The color bar gives the flux density in Jy.

Table 2.3. VLA late-time observations of the GW170817 field. See text for details on RMS measurements.

Date (UT)	ν (GHz)	VLA config.	Time on-source (hr)	RMS (μJy)	VLA program	PI	Nominal synth. beam ($''$)
2021 Dec 06	3.0	B	2 h24 m54 s	4.9 (3.6)	21B-057	Balasubramanian	2.1
2021 Dec 20	3.0	B	2 h25 m57 s	4.4 (3.9)	21B-057	Balasubramanian	2.1
2021 Dec 28	3.0	B	2 h25 m57 s	4.7 (3.9)	21B-057	Balasubramanian	2.1
2022 Jan 05	3.0	B	2 h25 m57 s	4.9 (4.3)	21B-057	Balasubramanian	2.1
2022 Mar 05	2.9	A	2 h28 m00 s	4.4 (3.9)	22A-168	Balasubramanian	0.65
2022 Mar 10	3.0	A	2 h28 m08 s	4.4 (3.9)	22A-168	Balasubramanian	0.65
2022 Mar 14	3.0	A	2 h28 m02 s	4.0 (3.9)	22A-168	Balasubramanian	0.65
2022 Mar 17	3.0	A	2 h28 m08 s	4.0 (3.9)	22A-168	Balasubramanian	0.65
2022 Mar 22	3.0	A	2 h28 m10 s	4.1 (4.0)	22A-168	Balasubramanian	0.65
2022 Mar 23	3.0	A	2 h17 m34 s	4.4 (4.1)	22A-168	Balasubramanian	0.65
2022 Mar 28	3.0	A	2 h38 m42 s	3.7 (3.4)	22A-168	Balasubramanian	0.65
2022 Mar 29	3.0	A	2 h28 m00 s	3.9 (3.7)	22A-168	Balasubramanian	0.65

Table 2.4. Results for the co-added late-time radio observations of GW170817. See text for discussion.

Date (UT)	Epoch (yr)	ν (Hz)	F_ν (μJy)	σ_ν (μJy)	Instrument	Reference
2021 Dec 06 - 2022 Jan 05	4.3	2.8×10^9	< 6.6	2.2	VLA B	This work
2022 Mar 05 - 2022 Mar 29	4.6	3.0×10^9	< 4.5	1.5	VLA A	This work
2021 Dec 06 - 2022 Mar 29	4.5	3.0×10^9	< 3.3	1.1	VLA A&B	This work
2021 Dec 07 - 2022 May 18	4.5	2.41×10^{17}	5.18×10^{-5}	3.44×10^{-5}	Chandra	GCN[†]

[†] O’Connor and Troja (2022)

2.3.2 Results and Conclusions

In Figure 2.7, we show the 3 GHz light curve of GW170817 (see the panchromatic afterglow data webpage[2] for a compilation of the full dataset). The black data points are the previous radio observations (Hallinan et al., 2017; Mooley et al., 2018d,b; Makhathini et al., 2021) that follow the jet+cocoon afterglow model (black line with gray 1σ error region). The red star shows our previous radio detection at 3.5 years since merger (Balasubramanian et al., 2021b). The radio upper limit from this work is shown with a downward pointing red triangle. As evident from this figure, we do not find any significant evidence for emission in excess to the expectations from a decaying jet+cocoon afterglow model, confirming our previous results (Balasubramanian et al., 2021b).

For comparison, in Figure 2.7 we also show the X-ray flux measurements derived from *Chandra* observations of the GW170817 field are shown as purple squares (see e.g., Haggard et al., 2017; Margutti et al., 2017a; Troja et al., 2017; Hajela et al., 2022; Troja et al., 2022, and references therein) extrapolated to the radio band using a radio-to-X-ray spectral index of $\beta = -0.584$ (see Makhathini et al., 2021). Recently, O'Connor and Troja (2022) also reported a measurement of $\sim 0.6 \times 10^{15}\,\mathrm{erg\,cm^{-2}s^{-1}}$ for the $0.3-10\,$keV flux of GW170817 at $\approx 4.8\,$years after the merger, using observations carried out with the *Chandra* observatory (O'Connor and Troja, 2022; Hajela et al., 2021a). We convert this flux into a flux density at 1 keV (see Table 2.4) and, by combining it with the radio upper-limit presented here, we de-

---

[2] http://www.tauceti.caltech.edu/kunal/gw170817/gw170817_afterglow_data_full.txt and https://github.com/kmooley/GW170817/

rive a radio-to-X-ray spectral index of $\beta \gtrsim -0.608$. This is compatible with the best fit value obtained via previous observations of the structured jet afterglow ($\beta = -0.584 \pm 0.002$; Makhathini et al., 2021), and with the results of our analysis at 3.5 years after merger ($\beta = -0.535 \pm 0.024$; Balasubramanian et al., 2021b).

Hereafter, we discuss the implications of our latest radio observations in the context of the kilonova ejecta model, following the formulation of Kathirgamaraju et al. (2019) as described in Section 2.2.2.

For $\alpha = \infty$, Equations 2.2-2.4 reduce to the case of a spherical outflow of total energy E with uniform velocity β_0 (Nakar and Piran, 2011). In this case, our flux upper-limit at 4.5 yr constrains the energy E and speed β_0 for a given choice of the density and micro-physical parameters. Indeed, setting these parameters as in Makhathini et al. (2021), an energy of $E \approx 10^{50}$ erg and speed of $\beta_0 \approx 0.5$ would produce a radio peak flux comparable to our 3σ upper-limit at 4.5 yrs since merger. Hence, single-speed ejecta more energetic than $E \approx 10^{50}$ erg must be slower than $\beta_0 \approx 0.5$. Else, radio emission from such ejecta would have peaked before 4.5 yrs in the radio, at a flux level above $3.3\,\mu$Jy.

Next, in Figure 2.8 we consider the case of a stratified ejecta with an energy-speed distribution described by the parameter α. In this case, we can use our observations to constrain α under specific assumptions on the energy and minimum speed of the ejecta, and of the density and micro-physical parameters. The blue and green curves in the left panel of Figure 2.8 show the rising portion of the predicted kilonova afterglow. Specifically, the shades of solid blue curves assume the parameters $E = 10^{51}$ erg, $\beta_0 = 0.3$, $p = 2.1$, $\epsilon_e = 7.8 \times 10^{-3}$, $\epsilon_{\rm B} = 9.9 \times 10^{-4}$, $n = 9.8 \times 10^{-3}{\rm cm}^{-3}$, $d = 40\,$Mpc (as in Makhathini et al., 2021); the dotted green and red curves assume the parameters $E = 10^{51}$ erg, $\beta_0 = 0.3$, $p = 2.2$, $\epsilon_e = 10^{-1}$, $\epsilon_{\rm B} = 10^{-3}$, $n = 10^{-2}{\rm cm}^{-3}$, $d = 40\,$Mpc (as in Kathirgamaraju et al., 2019). The radio observations presented here (red downward pointing triangle for our 3σ upper-limit, and grey cross and dashed error bars for the flux measurement at the location of GW170817) constrain α to $\alpha \gtrsim 6$ if we assume the parameters as in Makhathini et al. (2021). For the more general choice of micro-physical parameters (Kathirgamaraju et al., 2019), our latest upper-limit is compatible only with the more extreme cases of very steep values of α or with a kilonova blast wave comprised of a single velocity component ($\alpha = \infty$).

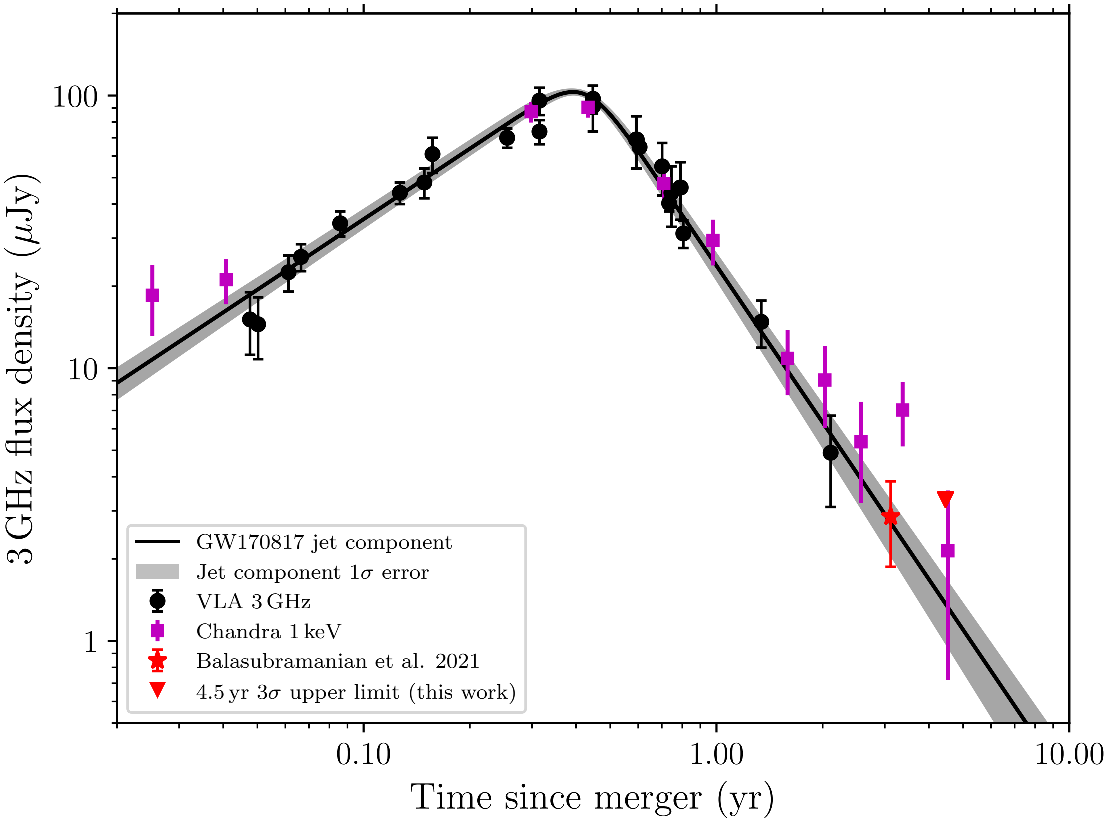

Figure 2.7. 3 GHz radio light curve of GW170817 with the best fit structured jet model from Makhathini et al. (2021). Radio data are shown as black data points. The *Chandra* 1 keV data scaled to 3 GHz with a power-law index of $\beta = -0.584$ (including the latest measurement by O'Connor and Troja, 2022) are shown as purple squares (see e.g., Haggard et al., 2017; Margutti et al., 2017a; Troja et al., 2017; Hajela et al., 2022; Troja et al., 2022, and references therein). Our previous observation 3.5 years since merger is marked with a red star (Balasubramanian et al., 2021b). The 3 σ upper limit from this work is shown as red downward pointing triangle.

The results presented here can also improve on the constraints discussed in Nedora et al. (2021c) regarding the NS EoS. In the right panel of Figure 2.8 we show a plot of the EoS-dependent model radio light curves from Nedora et al. (2021c), compared with the radio upper-limit derived in this analysis. As evident from this figure, our radio observations at 4.5 yrs since merger add new constraints on the possible EoSs, disfavoring the softer EoS SFHo (with $p = 2.05$, $\epsilon_e = 0.1$, $\epsilon_B = 0.01 - 0.001$ and $n = (4 - 5) \times 10^{-3}\,\mathrm{cm}^{-3}$), as well as the stiffer LS220 (with $p = 2.05$, $\epsilon_e = 0.1$, $\epsilon_B = 0.01 - 0.001$ and $n = 5 \times 10^{-3}\,\mathrm{cm}^{-3}$) in moderate mass ratio scenarios ($q \lesssim 1.43$). The SFHo and LS220 EoSs predict the same maximum mass of the cold non-rotating NS, but LS220 correlates with a steeper ejecta energy-speed distribution for $q = 1$ (Radice et al., 2018). On the other hand, scenarios like a DD2 EoS with $q = 1$, that predict a larger value of the cold, non-rotating maximum NS mass, are still possible.

We finally note that all the models used to generate the numerically simulated light curves (from Nedora et al., 2021a) and shown in the right panel of Figure 2.8 are derived from EoS that predict the stellar parameters (NS mass and radius) and tidal deformability parameter within the constraints obtained from GW and other astrophysical observations (Abbott et al., 2017b, 2018, 2019; De et al., 2018).

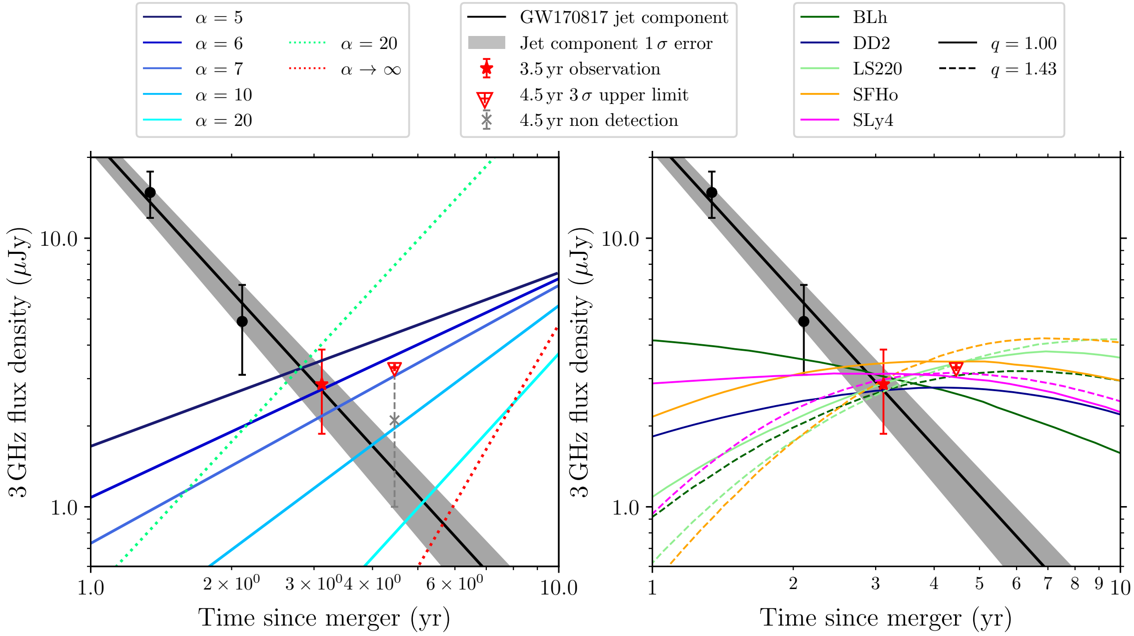

Figure 2.8. Late-time observations of the GW170817 field at 3 GHz from Makhathini et al. (2021) (black dots), Balasubramanian et al. (2021b) (red star), and from this work (red downward pointing triangle for our 3σ upper-limit; and grey cross for the maximum flux measured around the GW170817 position). We compare these observations with predicted kilonova afterglow light curves. *Left:* The solid lines in various shades of blue are the predicted kilonova afterglow light curves as a function of α (see §2.4) with the assumption that the minimum speed of the ejecta is $\beta_0 = 0.3$, for the parameters $E = 10^{51}$ erg, $p = 2.1$, $\epsilon_e = 7.8 \times 10^{-3}$, $\epsilon_\mathrm{B} = 9.9 \times 10^{-4}$, $n = 9.8 \times 10^{-3}\mathrm{cm}^{-3}$, $d = 40\,\mathrm{Mpc}$ (as in Makhathini et al., 2021) and $\alpha = 5, 6, 7, 10, 20$. For comparison, the green and red dashed line show the case $E = 10^{51}$ erg, $\epsilon_e = 10^{-1}$, $\epsilon_\mathrm{B} = 10^{-3}$, $n = 10^{-2}\mathrm{cm}^{-3}$, $p = 2.2$, $d = 40\,\mathrm{Mpc}$ (as in Kathirgamaraju et al., 2019), with $\alpha = 20, \infty$; *Right:* Predicted radio light curves of BNS ejecta for different EoS and mass ratios reproduced from Nedora et al. (2021c) (see their Figure 4 and Table 2). See text for discussion.

CHAPTER 3
FOLLOWUP OBSERVATIONS OF GRAVITATIONAL WAVE EVENTS AS A PART OF JAGWAR

3.1 JAGWAR - Jansky VLA mapping of Gravitational Wave bursts as Afterglows in Radio

With the discovery of GWs from merging compact objects (BHs and NSs), a new chapter has begun in the field of time domain astronomy. The LIGO (LIGO Scientific Collaboration et al., 2015) and Virgo (Acernese et al., 2015) (with KAGRA (Akutsu et al., 2021) joining them for the upcoming observation cycle) detectors generally have large localization areas in the sky. This has prompted multi-wavelength follow-up observations of the GW localization region to identify the source of the GW emission and study the physics of the remnant through the afterglow emission. As seen in the previous chapter of this thesis, observation in the radio wavelengths can be used to find afterglows resulting from ultra-relativistic and sub-relativistic ejecta. The Jansky VLA mapping of Gravitational Wave bursts as Afterglows in Radio (JAGWAR[1]) is a collaboration focused on devising strategies to improve chances of discovering radio counterparts of GW events using observations from the sensitive Janksy VLA instrument. The two alternative basic strategies adopted for the identification of a radio counterpart with maximum sensitivity are :

- Targeted search - search for already discovered afterglow (other wavelengths) - single deep pointing in C ($4-8\,$GHz) or S ($2-4\,$GHz) bands.
- Blind search - radio only search - multiple pointings in S band with maximum survey speed.

The program also partners with other leading radio telescopes around the globe like ASKAP (Johnston et al., 2008), ATCA (Middelberg et al., 2006), GMRT (Swarup, 1990), MeerKAT (Jonas, 2009) and AMI-LA (Zwart et al., 2008).

---

[1] http://www.tauceti.caltech.edu/jagwar/

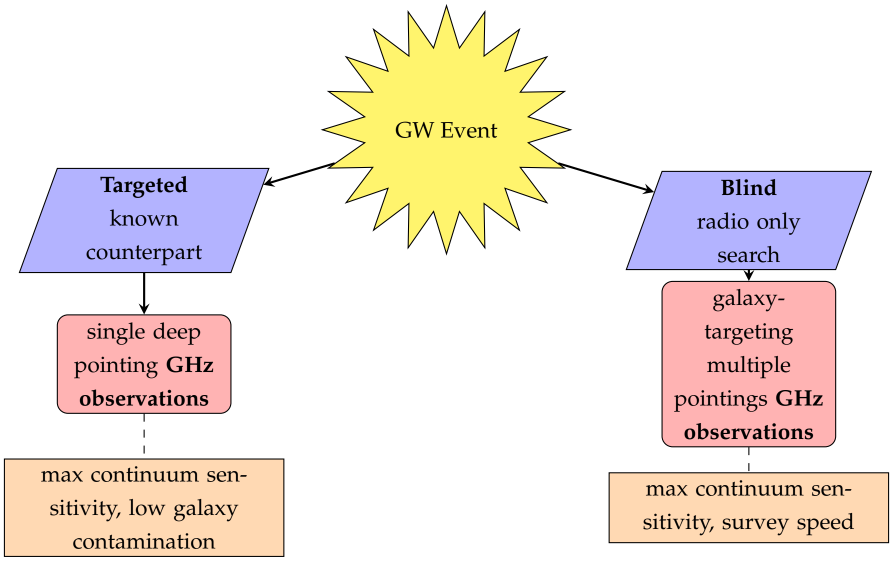

Figure 3.1. Observation strategies adapted by JAGWAR

The LIGO and Virgo collaborations have successfully completed three observation cycles and identified numerous GW candidates (The LIGO Scientific Collaboration et al., 2021). In the following sections, I discuss a selection of some of the candidates from the third observing run (O3), for which follow-up observations were made by the JAGWAR team.

3.2 GW191216 : Search for an EM counterpart of a BH-BH merger

GW191216 was observed on 16 December 2019 by the LIGO and Virgo collaborations. It was first classified as a mass-gap event (one of the constituent objects in the binary has a mass in between that of the heaviest NS and the lightest BH), but later on (about a week after the GW event) was re-classified as a binary BH merger (LIGO Scientific Collaboration and Virgo Collaboration, 2019c,d). Although EM emission from a binary BH merger is unlikely due to the absence of tidally disrupted material that can power EM emission, a possible detection of a gamma-ray counterpart to GW150914 (Connaughton et al., 2016) inspired several theoretical scenarios for EM emission. Those typically invoke the existence of some material (e.g., from the progenitor stars, AGN disks) in the merger environment whose accretion can power jets (Perna et al., 2019). The GW localization region of GW191216 was also rather large, as seen in many such observations. The High-Altitude Water Cherenkov Observatory (HAWC) reported a possible TeV counterpart detected 80 s after the GW191216 GW trigger (HAWC Collaboration, 2019). There were no other EM counterparts detected. The region of the sky from where the HAWC neutrino was detected was about 0.28 deg^2, a region feasible for a blind, radio only search (as described above).

Our team carried out deep C-band VLA observations of the field over 3 epochs each of 37 pointings to create a 0.38 deg^2 mosaic (3.2; see Bhakta et al., 2021, for details).

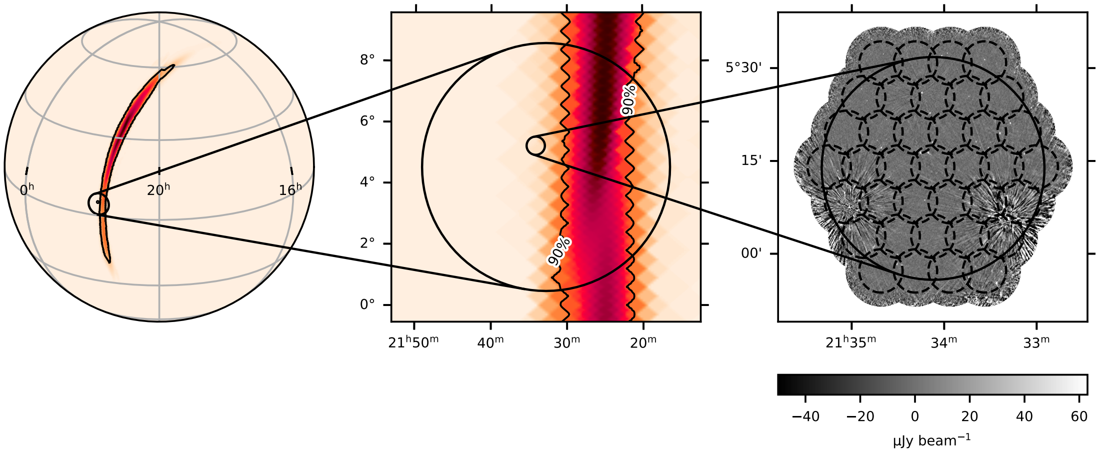

Figure 3.2. The LIGO/Virgo sky localization of GW191216 (left) localization region for the HAWC event (smaller circle of 0.28 deg^2 in middle panel). The right panel shows the sky coverage of our VLA follow up observations of the HAWC 68% containment region. The 0.38 deg^2 image mosaic is from our third epoch. The larger black circle corresponds to the 0.28 deg^2 HAWC region, while the smaller circles correspond to the primary beams (half-power beam width of about 7 arcminutes) of the 37 pointings at C band (central frequency of 6 GHz). Figure from Bhakta et al. (2021).

A sudden release of energy in the form of EM radiation is often thought to be due to the formation of a relativistic shock wave that interacts with the surrounding medium to produce multi-wavelength radiation. This outflow is mostly associated with jets, as confirmed by simulations and observations (an example of jet+cocoon emission seen from GW170817 was discussed in the previous chapter).

In the case of a binary BH merger, given the absence of tidally disrupted material during the merger, alternative ideas for EM emission were inspired by the aforementioned possible gamma-ray counterpart detection to binary BH (BBH) merger, GW150914. They all require some source of pre-existing material related to a progenitor star, an accretion disk or many other such examples (see Perna et al., 2019, and references therein for details). Mergers with one component being a NS can have tidally disrupted material that interacts with the jet (the "cocoon" seen in GW170817), while this is not likely for a binary BH merger, making it improbable to observe from larger angles. So, we may be able to observe a possible jet from a binary BH of the right energy, Lorentz factor and opening angle. Perna et al. (2019) have performed simulations of a population of BBH mergers assuming a range of energies and Lorentz factors for the possible jets emanating from the binary BH site at the time of merger.

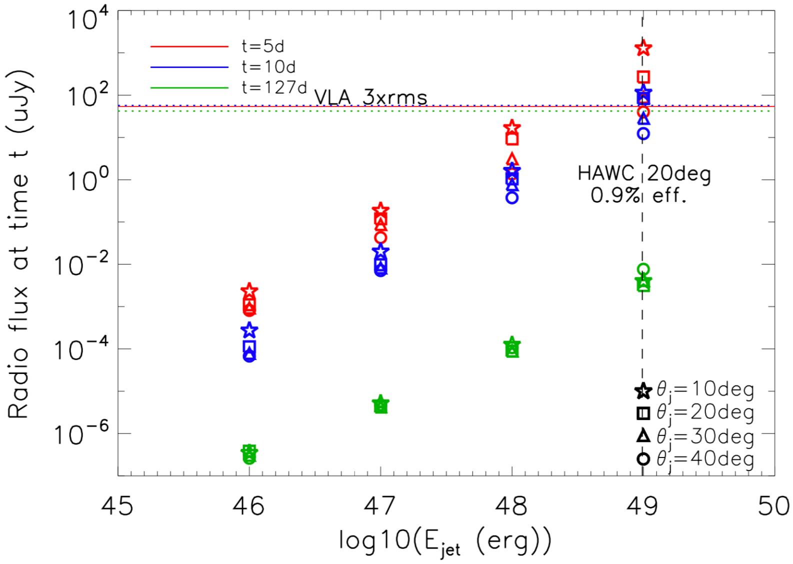

Figure 3.3. Constraints on the parameters of possible jets from binary BH mergers from our S191612ap upper limits (horizontal lines). These model predictions also assume a Lorentz factor of $\Gamma = 100$, and density of medium of $n_{\rm ISM} = 0.01\,{\rm cm}^{-3}$ and that the jet is pointed directly at the observer. Colors represent different epochs (in days from GW event) of observation (see legend). Figure from Bhakta et al. (2021).

Our observations did not yield any transients associated with GW191216 (Bhakta et al., 2021), the flux density upper limits derived are a significant improvement (a factor of two lower) over previous limits for radio counterparts from binary BHs (e.g., Mooley et al., 2018c; Artkop et al., 2019). Figure 3.3 shows the constraints that our upper limits (horizontal lines) place on a jet that is pointed directly at the observer, with a Lorentz factor of $\Gamma = 100$ and density of medium of $n_{\rm ISM} = 0.01\,{\rm cm}^{-3}$. Therefore, for observations as deep as ours, jets as energetic as 10^{49} erg cannot be detected if the jet opening angles are $\lesssim 20\,$deg.

3.3 Radio follow-up of AT2019wxt

The LIGO and Virgo collaborations reported S191213g, a GW compact binary merger candidate on 12 December 2019 at 04:34:08.1 UTC (LIGO Scientific Collaboration and Virgo Collaboration, 2019a). Initial classification of the GW event was that it was either a binary NS merger (77% probability) or a terrestrial event (23% probability, not astronomical but instrumental or environmental noise), with a false alarm rate of one in 10 months. Using all three detectors, the event was localized to a 50% localization region of area 259 deg^2 and a 90% localization region of area 1393 deg^2, while a posterior luminosity distance estimate from the GW amplitude was estimated to be 195±59 Mpc. A revised skymap and distance was posted by the LIGO and Virgo collaborations with a huge 90% localization region of area 4480 deg^2 and luminosity distance estimate of 201±81 Mpc (LIGO Scientific Collaboration and Virgo Collaboration, 2019b). No counterpart candidates were found in searches of this area at X-ray or gamma-ray wavelengths (Diego et al., 2019; Sugita et al., 2019; Verrecchia et al., 2019; Wilson-Hodge et al., 2019; Barthelmy et al., 2019; Cutini et al., 2019; Shenoy et al., 2019), nor were any found in neutrino searches (IceCube Collaboration, 2019; Ageron et al., 2019; Alvarez-Muniz et al., 2019). The Zwicky Transient Facility (ZTF) partially imaged the revised localization area (29%), and identified a number of initial candidates (Andreoni et al., 2019; Stein et al., 2019). After extensive follow-up spectroscopy and photometry (e.g., Perley et al., 2019; Fremling et al., 2019; Elias-Rosa et al., 2019; Smith et al., 2019; Brennan et al., 2019; Castro-Tirado et al., 2019), it was concluded that none of the optical transients were likely related to the S191213g GW event.

The Pan-STARRS collaboration reported a potential transient (PS19hgw) within the GW localization area as part of a larger search for kilonova candidates (McBrien et al., 2019). The object was at a right ascension (J2000)=01 h 55 m 41.94 s and Declination=+31 d 25 m 04.4 s, and was detected with an i-band (central wavelength 806 nm with bandwidth 149 nm) magnitude of 19.4±0.1 mag on 16 December 2019, PS19hgw or AT2019wxt was noted to lie close to the galaxy KUG 0152+311 at a redshift z = 0.036 (144 Mpc, NED). AT2019wxt showed narrow lines consistent with the host galaxy redshift of z=0.037, and a blue, relatively featureless continuum with a broad feature at 5400 - 6200 Angstroms. Vogl et al. (2019) identified the broad feature as being due to HeI lines, and suggested that AT2019wxt was either a young type Ib or perhaps type IIb SN (refer to Chapter 1 for classification of SNe). The similarities of the spectra to SN 2011fu (Kumar et al., 2013) prompted Vallely (2019) to classify AT2019wxt as a type IIb. This SN classification was subsequently supported by Valeev et al. (2019) and Becerra-Gonzalez and a larger Collaboration (2019).

Photometric measurements around this same time showed that AT2019wxt remained constant for several days after discovery (Fremling, 2019; Oates and Swift Team, 2019; Kong, 2019), before declining approximately two weeks after the S191213g GW event (Huber et al., 2019; Hopp et al., 2020). The consensus view at that time was that AT2019wxt was a type IIb SN and was unlikely to be related to the GW event S191213g (Becerra-Gonzalez and a larger Collaboration, 2019).

The latest catalog (released after $\sim$2 years from the GW event) of candidate sources of GWs (The LIGO Scientific Collaboration et al., 2021) from the LIGO VIRGO third observation run (O3) has declared that this GW event is no longer a candidate. However, the SN type IIb classification and the peculiar optical emission (see our paper Hinna et al. in prep) was still a source of interest. The optical i-band light curve shows a double peak structure that is characteristic of stripped envelope core-collapse SNe (SESN). No variable source has been detected in the X-ray observations of the field. We observed the source in the X (10 GHz), Ku (15 GHz) and K (22 GHz) bands of the VLA from ~ 4 days to ~ 263 days since the first optical detection (reference epoch: MJD 58833.335) in the D, C and B configuration of the VLA array (see Table 3.1).

Table 3.1. VLA observations of AT2019wxt along with the integrated flux measurements of the host galaxy KUG 0152+311. All epochs refer to the first optical detection (MJD 58833.335).

Obs. Time (MJD)	Time Elapsed (days)	VLA config.	VLA band	Obs. Freq. (GHz)	Source Flux (μJy) $F_\nu \pm \sigma_\nu$	Galaxy Flux (μJy) integrated $F_\nu \pm \sigma_\nu$
58837.0	3.7	D	K	22.0	< 25.1	452.5 ± 90.8
58914.8	84.6	C	X	10.0	19.9 ± 4.5	283.1 ± 28.6
58919.1	88.9	C	Ku	15.4	15.5 ± 3.2	335.0 ± 33.6
58921.7	91.5	C	X	9.3	27.4 ± 5.1	306.5 ± 30.9
58933.0	102.8	C	Ku	15.4	10.0 ± 3.0	240.5 ± 24.2
58933.7	103.5	C	X	9.8	16.0 ± 3.5	261.6 ± 26.3
58939.0	108.8	C	X	10.0	14.2 ± 3.2	291.6 ± 29.3
58940.0	109.8	C	Ku	15.4	12.6 ± 3.3	241.3 ± 24.3
58943.7	113.5	C	K	22.0	< 21.6	155.4 ± 31.6
58949.7	119.5	C	Ku	15.4	< 9.6	242.4 ± 24.4
58950.0	119.8	C	X	9.7	27.2 ± 4.1	292.8 ± 29.4
58956.7	126.5	C	K	22.0	< 11.7	233.5 ± 46.8
58957.6	127.5	C	Ku	15.3	< 10.8	207.9 ± 21.1

58958.6	128.4	C	X	10.0	24.7 ± 3.4	310.6 ± 31.1
58969.9	139.7	C	X	10.0	9.6 ± 3.0	203.0 ± 20.5
58970.6	140.4	C	Ku	14.8	11.0 ± 2.9	203.1 ± 20.5
58971.6	141.4	C	X	9.3	17.9 ± 3.7	273.2 ± 27.5
58974.9	144.7	C	Ku	15.7	9.7 ± 3.2	178.1 ± 18.1
59002.5	172.3	C	X	9.4	21.7 ± 3.9	310.1 ± 31.2
59087.3	257.1	B	Ku	15.0	< 10.2	125.4 ± 12.9
59089.3	259.1	B	X	10.0	< 9.6	150.8 ± 15.4
59092.6	262.4	B	Ku	15.0	< 10.8	125.2 ± 12.9

All K band (22 GHz) observations of the source were upper limits and so, only the X (10 GHz) and Ku (15 GHZ) band data were used for further analysis. Figure 3.4 shows the radio light curves of AT2019wxt (top panel) and the host galaxy KUG 0152+311 (bottom panel). Observations with significance $< 3\,\sigma$ are shown as downward pointing triangles to indicate upper-limits.

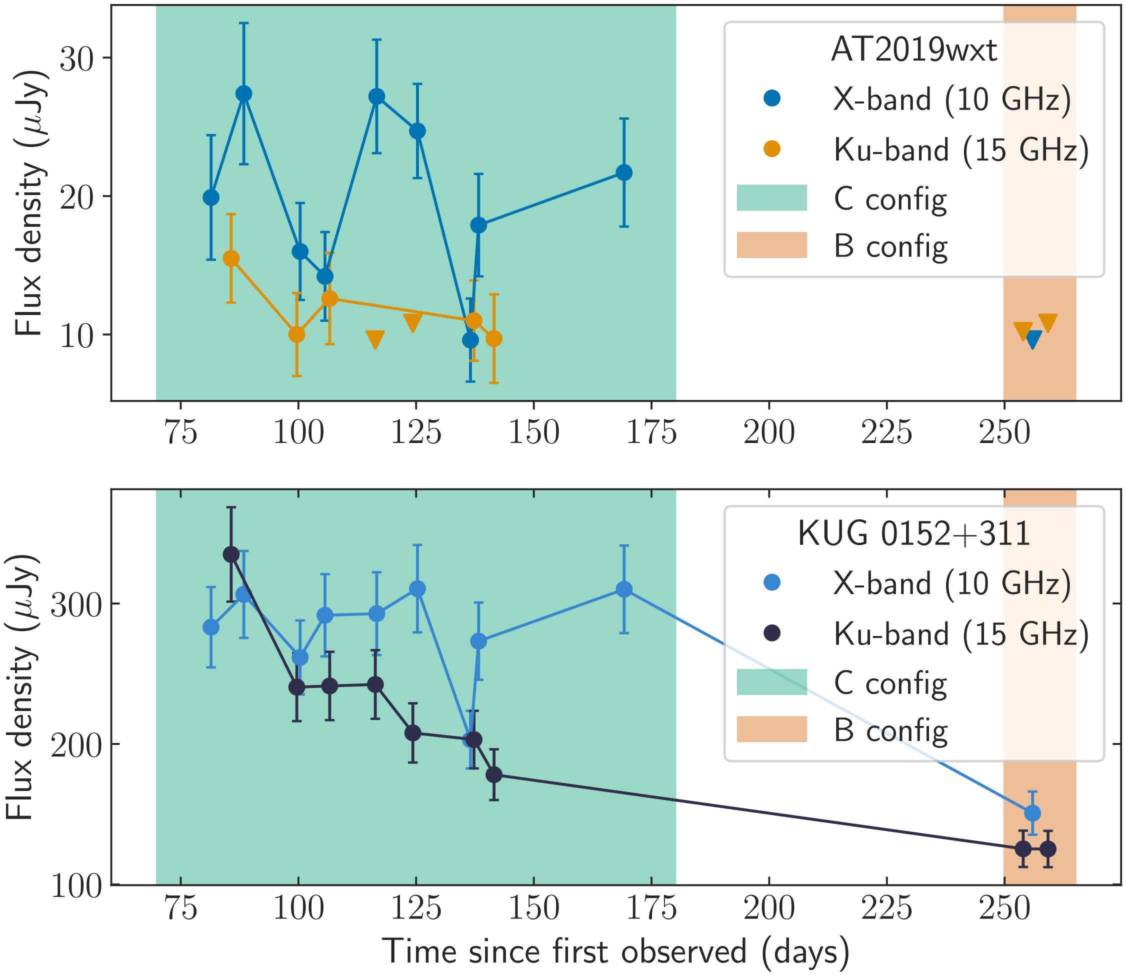

Figure 3.4. Radio light curve of AT2019wxt compared to the light curve of the host galaxy, KUG 0152+311.

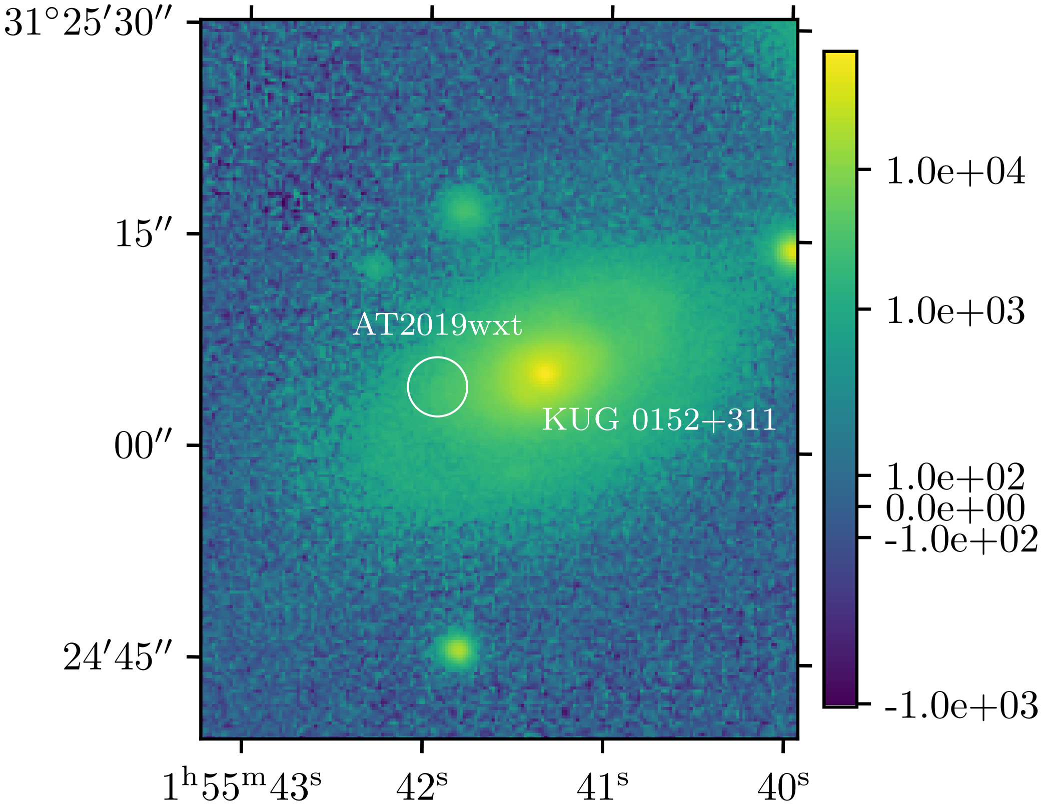

Figure 3.5. Location of AT2019wxt with respect to its host galaxy. The image is a Pan-STARRS i-band optical archival image of the field, with the circle (radius=2.1 arcsec) centred at the optical position of AT2019wxt.

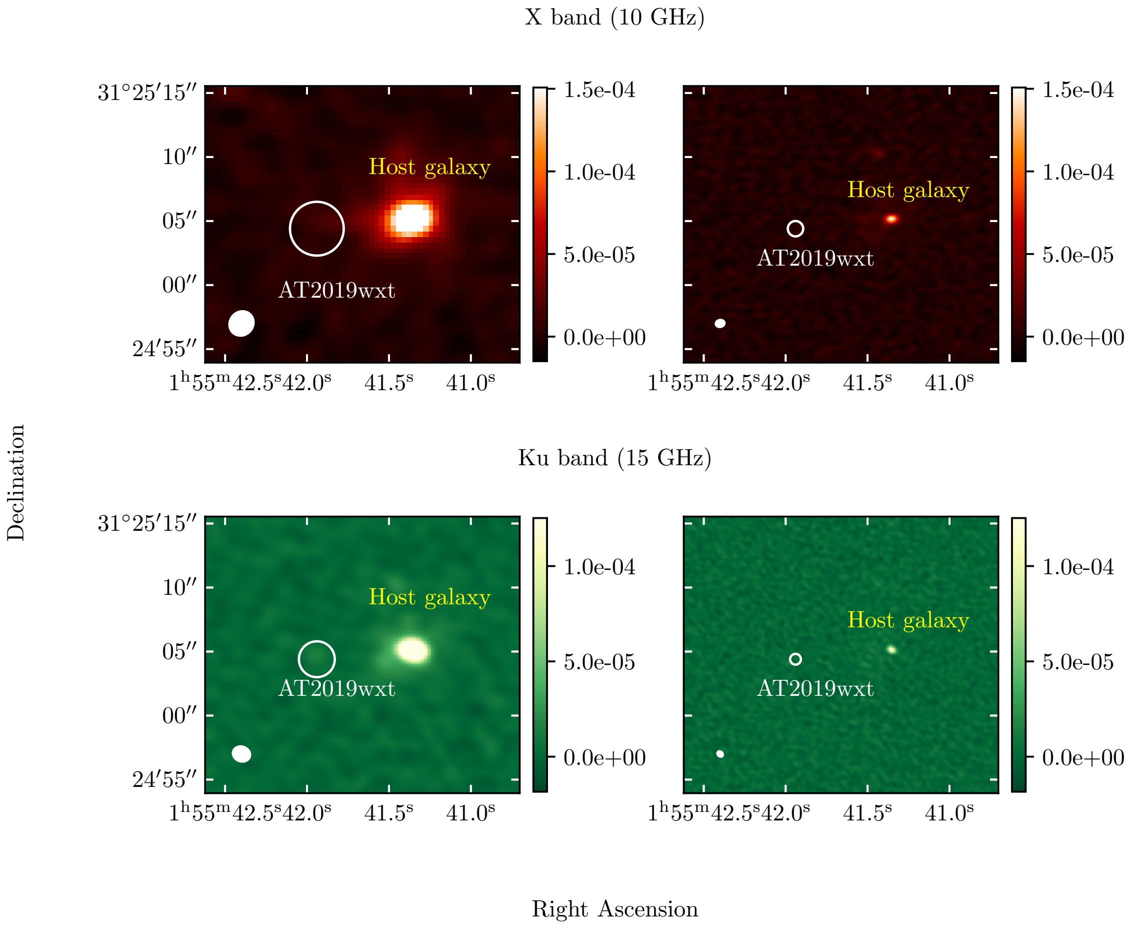

Figure 3.6. Comparison of images in C configuration (left panels) and B configuration (right panels). The top panels are the X (10 GHz) band observations and the bottom panels are the Ku (15 GHz) observations. White circles are the region in which the flux density for AT2019wxt are calculated.

The host galaxy appears resolved in all images. Figure 3.6 shows the images from the two different configurations (left panels: C configuration and right panels: B configuration) and two observation bands (top panels: X band and bottom panels: Ku band). This figure indicates that there is the possibility of host galaxy flux leaking into the source region (white circles) in the C configuration measurements (left panels). This is clearly noticed as there are only non-detections of the source in the B config observations that do not capture the large scale emission from the host galaxy. So, it is highly probable that all "detections" (significance

$> 3\,\sigma$) of the source may be excess flux density from the host galaxy. To test whether the flux measured at the location of AT2019wxt is dominated by the host, we compute the Pearson correlation coefficient and obtain the result that the host and AT2019wxt flux densities are 99.32% correlated in the X band and 98.71% correlated in Ku band. To visually reiterate the correlation between AT2019wxt and host galaxy flux densities, we plot them against each other in Figure 3.7.

To further quantify the variability of AT2019wxt, we compute some variability statistics as described in Swinbank et al. (2015). We use N, F$_\nu$ and σ_ν to represent the number of observations, flux density measurements and the corresponding errors at frequency ν (see Table 3.1) respectively. The flux density coefficient of variation can be calculated as:

$$V_\nu = \frac{1}{\overline{F_\nu}} \sqrt{\frac{N}{N-1}\left(\overline{F_\nu{}^2} - \overline{F_\nu}^2\right)}. \tag{3.1}$$

Assuming weights of $w_\nu = 1/\sigma_\nu^2$, the weighted average flux density is calculated as:

$$\xi_{F_\nu} = \frac{\sum_{i=1}^{N} w_{\nu,i} F_{\nu,i}}{\sum_{i=1}^{N} w_{\nu,i}}. \tag{3.2}$$

Further, we calculate the reduced-χ^2 using the above defined weighted mean flux density

$$\eta_\nu = \frac{1}{N-1} \sum_{i=1}^{N} \frac{\left(F_{\nu,i} - \xi_{F_\nu}\right)^2}{\sigma_{\nu,i}^2}. \tag{3.3}$$

Using this metric we can calculate the probability for the source to be a variable as:

$$P_{\mathrm{var}} = 1 - \int_{\eta_\nu{}'=\eta_\nu}^{\infty} p\left(\eta_\nu{}', N-1\right) \mathrm{d}\eta_\nu{}'. \tag{3.4}$$

where $p(x, n)$ is the χ^2 probability density function for x over n degrees of freedom.

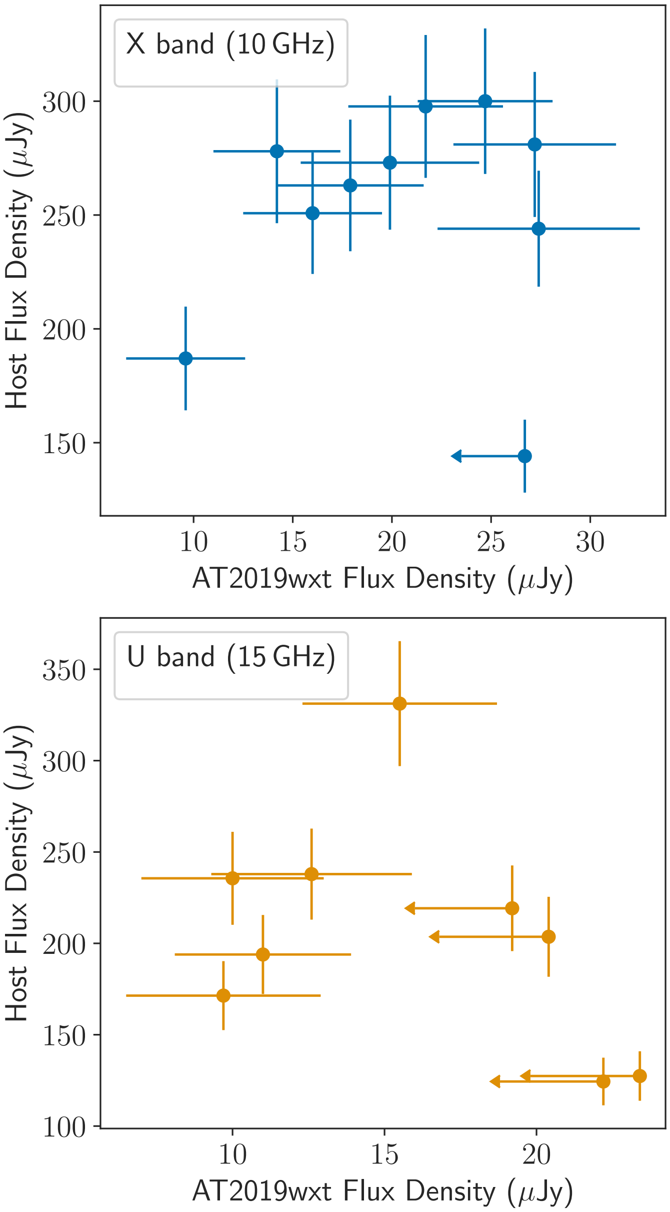

Figure 3.7. This figure visually illustrates the correlation between AT2019wxt and host galaxy flux densities at 10 GHz (top panel) and 15 GHz (bottom panel).

Table 3.2. Radio variability metrics for AT2019wxt compared with the host galaxy and type IIb SN, SN 1993J in X (10 GHz) and Ku (15 GHz) bands excluding upper limits.

Freq. band	AT2019wxt		Host		SN 1993J	
	V_ν	$P_{\rm var}$ (%)	V_ν	$P_{\rm var}$ (%)	V_ν	$P_{\rm var}$ (%)
X (10 GHz)	0.3	5.6	0.1	2.2	0.2	48.4
Ku (15 GHz)	0.2	3.3	0.2	32.6	0.2	4.2×10^{-3}

Table 3.2 lists the variability statistics of AT2019wxt excluding upper limits along with those for the host galaxy KUG 0152+311 and a well sampled type IIb SN, SN 1993J (this comparison is motivated by the fact that AT2019wxt was initially classified as a type IIb SN). In the X band, we see that the statistics indicate that AT2019wxt and the host galaxy show similar variability that is much less compared to the variability of SN 1993J. This result taken with the fact that the host and AT2019wxt fluxes are strongly correlated points to the conclusion that the AT2019wxt flux measurements may be contaminated from excess emission from the host galaxy in X band. The U band variability is much more complicated. SN 1993J does not vary much in the time scales of interest. However, we see that the host galaxy variability far exceeds the variability of AT2019wxt. The variability of the host galaxy itslef needs to be explored further in the future as there are no previous observations/studies of this galaxy and its properties. Therefore, we conclude that there is no evidence of a significant variable radio source in the region of AT2019wxt.

3.4 Preliminary results on GW190814

The first half of the third observing run (O3a) of Advanced LIGO - Advanced Virgo collaboration reported 39 candidate compact merger events (Abbott et al., 2021). One of these candidates, GW190814, is the most asymmetric system observed to date with the component objects weighing $\sim 26\, M_\odot$ and $\sim 2.6\, M_\odot$. This source was discovered on on 2019 August 14, 21:11:00 UTC (Abbott et al., 2020b) and was finally localized to an incredible 19 deg^2 with 90% confidence (50% confidence area $= 4\,$deg^2 Abbott et al., 2021). Although this event has been classified as a neutron star-black hole (NSBH) merger (The LIGO Scientific Collaboration et al., 2021), the nature of the second mass remains elusive - is it the heaviest NS or lightest BH to ever be observed? While EM emission is expected when one component is a NS (e.g., Hotokezaka et al., 2016; Rosswog et al., 2017), the detection of gamma-rays from a source possibly related to another BBH event GW150914 (Connaughton et al., 2016) has excited the community. This justifies the need to make follow-up observations of GW190814 even if the nature of the second mass is unknown (see also Section 3.2).

Numerous searches for an EM counterpart for GW190814 have not been successful (e.g., Page et al., 2020; Gompertz et al., 2020; Watson et al., 2020; Antier et al., 2019; Gomez et al., 2019; Andreoni et al., 2020; Morgan et al., 2020; Vieira et al., 2020; Thakur et al., 2020; Ackley et al., 2020; Dobie et al., 2019). A shallow, galaxy targeted search in the radio frequencies at 4 GHz was made with the help of the VLA, not yielding a detection of any potential radio counterpart (Alexander et al., 2021). In addition, a deep 944 MHz search using the Australian Square Kilometre Array Pathfinder (ASKAP) also did not reveal potential counterparts (Dobie et al., 2022).

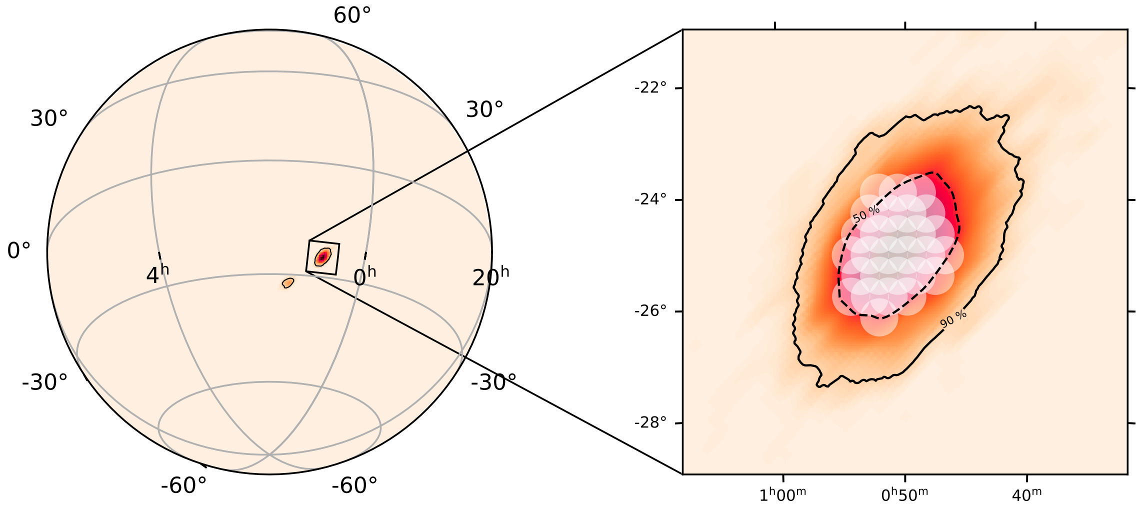

Figure 3.8. *Left :* The LIGO Virgo localization of the source with black solid outlines representing the 90% confidence region. *Inset :* Zoomed in portion of the localization region showing the mosaic of observations from this work (white translucent region) covering the 50% confidence area of 4 deg^2. The mosaic is composed of 28 individual pointings (circles making up the white translucent region).

We conducted a deeper, blind survey of the 50% confidence region at 1.5 GHz using VLA with observations spanning over 3 epochs, with the image in each epoch made by mosaicking 28 pointings (observations of a field). Figure 3.8 shows the coverage of the 50% localization we achieve by our observations. We are in the process of imaging these observations. The imaging for such large mosaics is a challenge and new methods are being developed to quickly generate such mosaicked radio images (for e.g., in the case of the congoing VLA Sky Survey. See Lacy et al., 2020) Once imaged, we will create point source catalogs from each epoch and cross-match these catalogs to obtain a master catalog. For each source on this master catalog, we will examine its flux variability and select the sources that show significant variability. Next, these selected sources are queried on databases of variable sources to determine if they are already known sources and remove them from the selected list. If any source remains in this list after the comparison with databases, we will test that the source satisfies expected models for light curves from merging compact objects, thereby constraining the physical parameters of the models.

CHAPTER 4

LATE TIME RE-BRIGHTENING OF RADIO-BRIGHT SN 2004DK

Having discussed the radio emission from merging compact objects in Chapter 2 and Chapter 3, here I turn my attention to stripped-envelope (Type Ib/c) core-collapse SNe, another class of transients that have been linked to long GRBs and the formation of compact objects in single star explosions (see Figure 1.2).

Type Ibc SNe, which constitute $\approx 16.3\%$ of the local core collapse SNe (Perley et al., 2020), are the class of core-collapse SNe which lack Hydrogen (H) lines in their spectra (Ib = He-rich; Ic = He-poor; see Figure 1.3). Many aspects of the mass loss and progenitor physics of such explosions are still unanswered (e.g., Wellons et al., 2012; Soderberg et al., 2006). The study of the structure of the medium (CSM) in the vicinity of the explosion provides insights into the last stages of evolution of the pre-SN progenitor. After the core collapses, shock waves produced due to the collapse travel outward and eventually interact with material ejected by the star before its explosion (layers are shed at many stages during the different burning cycles). Radio (and X-ray) observations can help study such interactions, mapping out the mass loss history of the progenitor (e.g., Soderberg et al., 2005, 2006; Corsi et al., 2014; Margutti et al., 2017b; Rivera Sandoval et al., 2018; Palliyaguru et al., 2019). In addition, because non-thermal radio emission probes the fastest moving ejecta, we can discover the most relativistic type Ibc explosions associated with long GRBs (i.e., relativistic jets) via their bright radio emission. Basically, for a similar CSM density, how radio bright a SN is and how early its emission peaks in the radio constrain the speed of the fastest components of its ejecta (Berger et al., 2003). However, what exact mechanisms make some (a small fraction of the total) Ibc SNe power relativistic ejecta (GRBs) is still a mystery. Thus, studying and characterizing the entire zoo of possible radio transients associated with Ibc events may help us shed light on such unknown explosion physics (Berger et al., 2003; Corsi et al., 2016).

4.1 Observations of SN 2004dk

As part of our investigation of stripped-envelope core-collapse SNe we have carried out late-time (~ 14 years since explosion) observations of radio-bright SN 2004dk with the VLA and VLA Low Band Ionosphere and Transient Experiment (VLITE [1]; Clarke et al. 2016) in order to investigate the presence/absence of signatures of jet emission. SN 2004dk is a type Ibc event with a peculiar radio light curve characterized by a late-time re-brightening (Balasubramanian et al., 2021a). Low frequency radio observations help in probing absorption mechanisms and CSM structure. SN 2004dk was discovered by the Katzman Automatic Imaging Telescope (KAIT) on 2004 August 1.19 UT (Graham and Li, 2004) at RA = 16 h 21 m 48.87 s, Dec = -02 d 16 m 17.6 s in the galaxy NGC 6118, at a distance of $\approx$ 23 Mpc (average distance for Nasa Extragalactic Database distances calculated using Hubble constant $H_0 = 72 - 75$ km s^{-1} Mpc^{-1}).

A brief description of the observations of the SN, discussed in Balasubramanian et al. (2021a), follows.

4.1.1 VLA observations

SN 2004dk was first observed at GHz radio frequencies at about 8 days after explosion, with the Karl G. Jansky Very Large Array (VLA). Follow-up observations with the VLA continued until 2009 ($\Delta t \sim 1912$ days since explosion; Stockdale et al., 2009; Wellons et al., 2012). A summary of the radio observations carried out with the VLA between 4.9 GHz and 22.5 GHz is reported in the first section of Table 4.1 (adapted from Wellons et al., 2012). The 8.5 GHz light curve of SN 2004dk peaks at $\sim$ 14 days from the SN explosion, with a flux density $F_\nu \approx$ 2.5 mJy. At an epoch of $\Delta t \sim 1700$ days since explosion, a re-brightening is observed at 4.9 GHz and 8.5 GHz.

A more recent GHz radio observation of the SN 2004dk field was carried out on 2018 April 7.4 UT ($\Delta t \sim 5000$ days since explosion) with the VLA in its A configuration (VLA/18A-119, PI: Margutti; see Table 4.1). 3C286 was used as flux calibrator and J1557-0001 was used as complex gain calibrator (to calibrate phase/position). We calibrated this data in `CASA` (McMullin et al., 2007b) using the standard VLA

---

[1] https://vlite.nrao.edu/

calibration pipeline, and then manually inspected and flagged the calibrated data for Radio Frequency Interference (RFI). After imaging the field with the `clean` task interactively, we used the `CASA` task `imfit` to obtain the integrated flux density of SN 2004dk (and the associated statistical error) within a circular region of radius 0.33″ (nominal VLA resolution at the observed frequency for A-array configuration) centered on the optical position of the SN. A 5% absolute flux calibration error was added in quadrature to the flux density error returned by `imfit` to account for error as the fluxes are dynamic range limited (e.g., Ofek et al., 2011).

4.1.2 VLITE observations

VLITE is a commensal, low-frequency system on the VLA that runs in parallel since 2014, with nearly all observations above 1 GHz. VLITE provides real-time correlation of the signal from a subset of VLA antennas using the low-band receiver system (Clarke et al., 2011) and a dedicated DiFX-based software correlator (Deller et al., 2007). The VLITE system processes 64 MHz of bandwidth centered on 352 MHz, but due to strong RFI in the upper portion of the band, the usable frequency range is limited to an RFI-free band of ∼40 MHz, centered on 338 MHz.

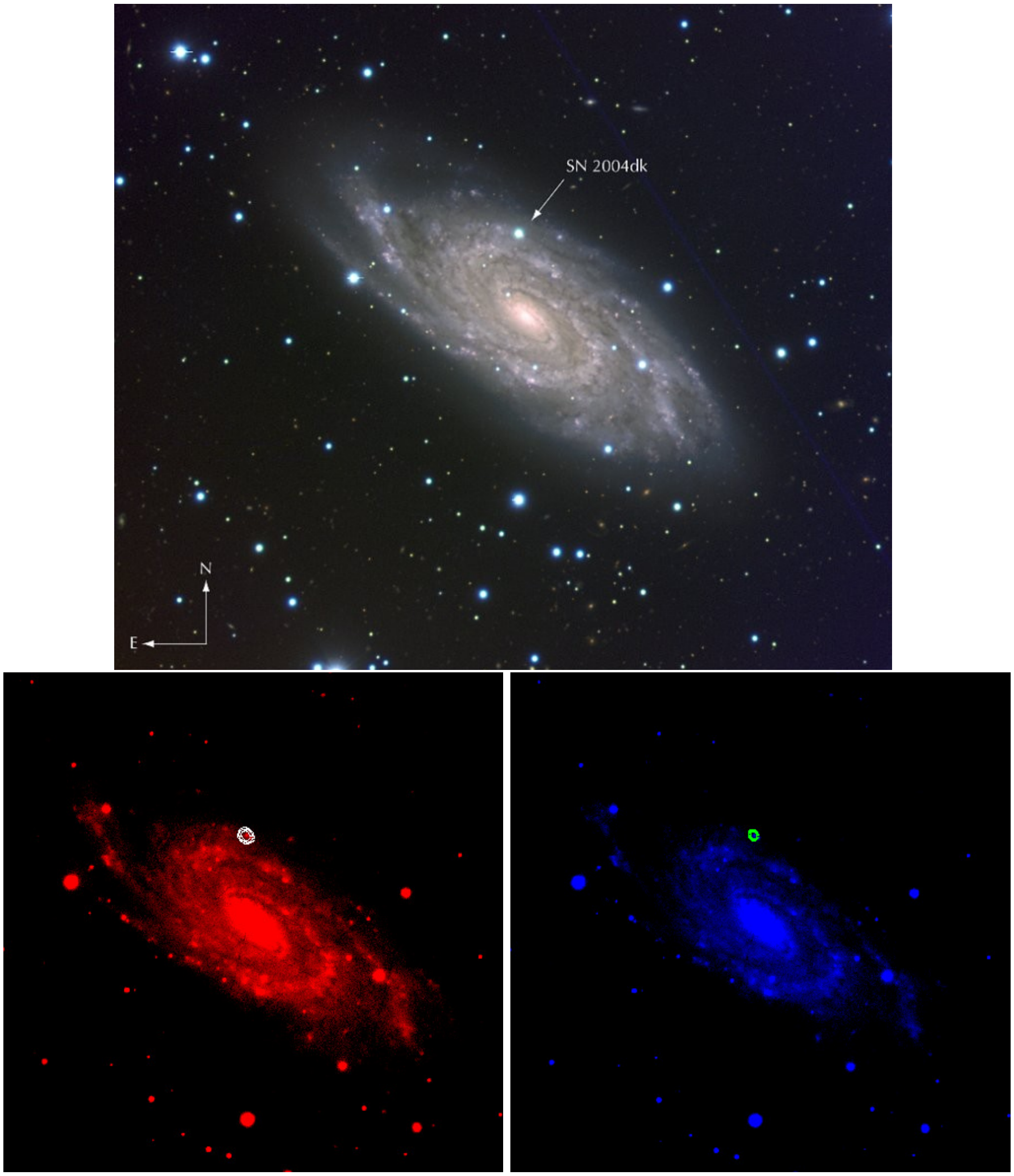

Figure 4.1. *Top*: VLT MELIPAL+VIMOS image (www.eso.org/public/images/eso0436b/) of the spiral galaxy NGC 6118 and SN 2004dk taken on 21 August 2004. *Bottom-left*: Radio contours observed using VLITE (white $-10\,\sigma$ outermost contour, see Table 4.1 for the data) on 01 Jan 2021 UT and *Bottom-right*: VLASS (green $-7\,\sigma$ outermost contour, see Table 4.1 for the data) on 21 May 2019, both overplotted on an r-band Pan-STARRS1 image of the field (Flewelling et al., 2020) with the help of SAOImageDS9 (Joye and Mandel, 2003).

SN 2004dk was observed by VLITE on 2018 April 8, 2019 August 30, 2020 December 28 and 2021 January 1 UT. The VLITE data are reported in the bottom section of Table 4.1. SN 2004dk is the first SN to be detected at sub-GHz frequencies by VLITE. VLITE data were processed using a dedicated calibration pipeline based on a combination of Obit (Cotton, 2008) and AIPS (van Moorsel et al., 1996) data reduction packages. The calibration pipeline uses standard automated tasks for the removal of RFI and follows common techniques of radio-interferometric data reduction, including delay, gain, and bandpass calibration (for details on the pipeline data reduction see Polisensky et al. (2016)). The flux density scale is set using Perley and Butler (2017). The final VLITE images have restoring beams (resolution) of approximately $6'' \times 4''$ and rms noise $0.5-1$ mJy beam^{-1} (1σ). Flux densities were measured with PyBDSF (Mohan and Rafferty, 2015) via the VLITE Database Pipeline (Polisensky et al., 2019). We conservatively adopt 20% flux density errors that include local image noise as well as fitting and flux-scale uncertainties.

4.1.3 VLASS archival observation

The VLA Sky Survey (VLASS) is an ongoing $2-4$ GHz survey of the entire sky visible to the VLA i.e., $\delta > -40$ deg for a total of about 33,885 deg^2 of the sky (Lacy et al., 2020).

We queried the VLASS quick look image archive for fields centered at < 1 deg from the optical position of SN 2004dk. We manually inspected the retrieved VLASS images and identified a source coincident with the optical position of SN 2004dk. The VLASS field containing the SN (observed in VLASS epoch 1.2[4]) was then analyzed using the `CASA` task `imfit` to obtain the integrated source flux density (and corresponding statistical error), using a circular region of radius $2.5''$ (nominal VLASS resolution) centered at the optical SN position. In order to account for absolute flux calibration errors, we added in quadrature to the integrated flux error returned by `imfit` a fractional 10% error (as VLASS Epoch 1 total flux densities are estimated to have systematic errors of order 10%[4]). Our results are reported in the bottom section of Table 4.1, and Figure 4.1 (right panel) shows the VLASS radio contours of SN 2004dk.

---

[4] https://science.nrao.edu/science/surveys/vlass/vlass-epoch-1-quick-look-users-guide

Table 4.1. Measured radio flux densities of SN 2004dk until Jan 2021. Data until Oct 2009 UT are from Wellons et al. (2012).The last four rows contain the more recent VLITE and VLA observations presented in this paper.

Date (UT)	Epoch (days)	340 MHz (mJy)	3.0 GHz (mJy)	4.9 GHz (mJy)	6.0 GHz (mJy)	8.5 GHz (mJy)	15.0 GHz (mJy)	22.5 GHz (mJy)	Inst.
2004 Aug 7.1	7.9	...	...	...	...	1.30±0.05	...	...	VLA-D
2004 Aug 11.0	11.8	...	...	0.87±0.06	...	2.11±0.06	...	2.78±0.33	VLA-D
2004 Aug 13.0	13.8	...	...	1.09±0.06	...	2.42±0.06	3.57±0.26	2.72±0.37	VLA-D
2004 Sep 2.0	33.8	...	...	1.80±0.09	...	1.56±0.13	0.79±0.21	0.69±0.18	VLA-D
2004 Sep 10.0	41.8	...	...	1.06±0.07	...	0.81±0.15	...	≤0.43	VLA-A
2004 Sep 18.0	49.8	...	...	0.86±0.10	...	1.19±0.11	...	≤0.47	VLA-A
2004 Oct 4.1	65.9	...	...	0.46±0.15	...	0.41±0.09	≤0.34	≤1.41	VLA-A
2004 Oct 17.8	79.6	...	...	0.56±0.10	...	0.47±0.12	≤0.92	...	VLA-A
2005 Feb 12.4	197.2	...	...	<0.26	...	<0.17	...	...	VLA-BnA
2009 Feb 12.6	1658.4	...	...	0.22±0.06	...	...	...	...	VLA-B
2009 Feb 24.5	1670.3	...	...	0.21±0.03	...	0.19±0.03	...	...	VLA-B
2009 Apr 2.6	1707.4	...	...	0.34±0.07	...	≤0.08	...	...	VLA-B
2009 Apr 19.0	1723.8	...	...	0.21±0.02	...	0.15±0.02	...	...	VLA-C
2009 Sep 19.8	1877.6	...	...	0.28±0.05	...	0.17±0.02	...	≤0.57	VLA-B

2009 Oct 26.8	1914.6	...	...	...	...	...	...	<0.27	VLA-D
2018 Apr 8.4	5000.2	17.10±3.42	...	...	...	...	...	...	VLITE
2018 Apr 8.4	5000.2	...	...	...	4.06±0.24 [a]	...	...	...	VLA-A
2019 May 21.4	5408.2	...	6.46±0.65 [b]	...	...	...	...	...	VLASS
2019 Aug 31.0	5509.8	11.20±2.24	...	...	...	...	...	...	VLITE
2020 Dec 28.7	5995.5	21.53±4.31	...	...	...	...	...	...	VLITE
2021 Jan 1.8	5999.6	21.52±4.30	...	...	...	...	...	...	VLITE

[a] Includes additional 5% flux error as the observation was dynamic range limited.

[b] Includes additional 10% flux error as this is a quick-look observation from VLASS.

4.2 Synchrotron Self Absorption model

The Synchrotron Self Absorption (SSA) model (Chevalier, 1998; Chevalier and Fransson, 2006) has been used successfully to describe late-time radio emission powered by SN ejecta-CSM interaction (e.g., Soderberg et al., 2005; Wellons et al., 2012; Palliyaguru et al., 2019). Within the SSA model, for a smooth CSM profile such as the one predicted to arise from a constant mass-loss rate, constant velocity pre-SN wind, the observed radio emission is characterized by a smooth turn-on first at higher frequencies, and later at lower frequencies. This evolution can be explained as a consequence of a self-absorption frequency which decreases with time as the SN shock propagates toward lower density regions. Modifications to this scenario include an initial exponential rise of the low-frequency radio flux due to free–free absorption (electrons gain energy by absorbing photons after colliding with ions) in the ionized CSM (an effect usually relevant at early times; see e.g., Weiler et al., 1990; Chevalier, 1998), as well as flux variations associated with a non-smooth CSM profile, perhaps associated with eruptive mass-loss from the SN progenitor (Wellons et al., 2012; Corsi et al., 2014; Palliyaguru et al., 2019). A detailed description of the SSA model focused on its application to radio SNe can be found in Soderberg et al. (2005). In what follows, we summarize briefly the model so as to introduce notation relevant for our analysis of the SN 2004dk data. Here, I describe the SSA model in brief, as discussed in Balasubramanian et al. (2021b).

Within the SSA model, we consider emission produced at a certain epoch t since explosion (i.e., $t = 0$ at the time of the explosion of the SN, t_e) from a thin shell of radiating electrons of radius r, and thickness r/η. The electrons are accelerated to a power-law distribution of Lorentz factors $N(\gamma) \propto \gamma^{-p}$, above a minimum Lorentz factor γ_m. The temporal evolution of the radius of the shell, of the magnetic field strength, and of the minimum Lorentz factor are assumed to follow the relations:

$$r(t) = r_0\left(\frac{t}{t_0}\right)^{\alpha_r}, \tag{4.1}$$

$$B(t) = B_0\left(\frac{t}{t_0}\right)^{\alpha_B}, \tag{4.2}$$

$$\gamma_m(t) = \gamma_{m,0}\left(\frac{t}{t_0}\right)^{\alpha_\gamma}, \tag{4.3}$$

where t_0 is an arbitrary reference epoch, t is the epoch since explosion t_e, and r_0, B_0, $\gamma_{m,0}$ are the values of the shell radius, magnetic field, and electron minimum Lorentz factor at this reference epoch, respectively. Also, the density profile of the radiating electrons within the shocked CSM is assumed to be $n_e \propto r^{-s}$. Assuming also equipartition, i.e., $\epsilon_e = \epsilon_B$ for the fraction of energy going into relativistic electrons and magnetic field respectively (see e.g., Wellons et al., 2012), one has:

$$\alpha_B = \frac{(2-s)}{2}\alpha_r - 1 \quad \text{and} \quad \alpha_\gamma = 2(\alpha_r - 1). \tag{4.4}$$

The flux density at a certain epoch t and frequency ν is given by:

$$f_\nu = C_f\left(\frac{t}{t_0}\right)^{(4\alpha_r-\alpha_B)/2}\left[1 - e^{-\tau_\nu^\xi(t)}\right]^{1/\xi}\nu^{5/2}F_3(x)F_2^{-1}(x), \tag{4.5}$$

where the optical depth $\tau_\nu(t)$ reads:

$$\tau_\nu = C_\tau\left(\frac{t}{t_0}\right)^{(p-2)\alpha_\gamma+(3+p/2)\alpha_B+\alpha_r}\nu^{-(p+4)/2}F_2(x), \tag{4.6}$$

and where $\xi \in [0,1]$ controls the sharpness of the spectral break between optically thin and thick regimes. In the above equations, F_2 and F_3 are Bessel functions of $x = 2/3(\nu/\nu_m)$ with ν_m the critical synchrotron frequency of electrons with Lorentz factor equal to γ_m. This frequency, ν_m, evolves with time as:

$$\nu_m = \nu_{m,0}\left(\frac{t}{t_0}\right)^{(10\alpha_r-s\alpha_r-10)/2}, \tag{4.7}$$

where

$$\nu_{m,0} = \gamma_{m,0}^2\frac{eB_0}{2\pi m_e c}. \tag{4.8}$$

The normalization constants for the flux density and optical depth, C_f and C_τ, are themselves functions of B_0, $\nu_{m,0}$, r_0 (see Equations (A13)-(A14) in Soderberg et al., 2005):

$$C_f = \frac{2\pi m_e}{2+p}\left(\frac{r_0}{d}\right)^2\left(\frac{2\pi m_e c}{eB_0}\right)^{1/2}, \tag{4.9}$$

$$C_\tau = \frac{(p+2)(p-2)\gamma_{m,0}^{(p-1)}}{4\pi\eta}\frac{B_0^2}{8\pi}\frac{e^3 B_0 r_0}{m_e^3 c^4 \gamma_{m,0}}\left(\frac{eB_0}{2\pi m_e c}\right)^{p/2}, \tag{4.10}$$

where d is the distance to the source.

At high frequencies, the observed spectral flux density needs to be corrected for the effects of synchrotron cooling, which occurs at frequencies above the cooling frequency (ν_c), defined as:

$$\nu_c = \frac{18\pi m_e c e}{t^2\sigma_T^2 B^3}. \tag{4.11}$$

Overall, the resulting spectral shape and temporal evolution of the flux density from Equation (4.5), corrected for the effects of synchrotron cooling, can be approximated as:

$$f_\nu \propto \begin{cases} \nu^2 t^{2\alpha_r+\alpha_\gamma} & \nu < \nu_m, \\ \nu^{1/3} t^{(4\alpha_r-\alpha_B)/2} & \nu_m < \nu < \nu_a, \\ \nu^{-(p-1)/2} t^{[4\alpha_r-\alpha_B+(4+p)\alpha_{\nu_a}]/2} & \nu_a < \nu < \nu_c, \\ \nu^{-p/2} t^{[2\alpha_r+(1-3p)\alpha_B+(2+p/2)\alpha_{\nu_a}-2p+1]} & \nu > \nu_c \end{cases} \tag{4.12}$$

where $\nu_m << \nu_a$ (self-absorption frequency), typically a good assumption at late times, and:

$$\begin{aligned} \nu_a &= \nu_{a,0}\left(\frac{t}{t_0}\right)^{[2(p-2)\alpha_\gamma+2(3+p/2)\alpha_B+2\alpha_r]/(p+4)} \\ &= \nu_{a,0}\left(\frac{t}{t_0}\right)^{\alpha_{\nu_a}}. \end{aligned} \tag{4.13}$$

Note that in the above Equation, $\nu_{a,0}$ can be calculated using the condition $\tau_{\nu_{a,0}}(t_0) = 1$.

Based on the above considerations, for a given t_e, via comparison with flux density observations at different times and frequencies, one can determine the set of parameters (B_0, α_r, p, $\nu_{m,0}$, r_0, s, ξ). These, in turn, constrain the physics of the emitting shell and the properties of the CSM. Specifically, one can derive constraints (see e.g., Soderberg et al., 2006) on the ejecta energy,

$$E = \frac{4\pi}{\eta} r_0^3 \frac{B_0^2}{8\pi\epsilon_e} \left(\frac{t}{t_0}\right)^{(5\alpha_r - s\alpha_r - 2)} \tag{4.14}$$

electron density,

$$n_e = \frac{(p-2)}{(p-1)} \frac{B_0^2}{8\pi m_e c^2 \gamma_{m,0}} \left(\frac{r}{r_0}\right)^{-s}, \tag{4.15}$$

and the mass loss rate,

$$\dot{M} = \frac{8\pi n_{e,0} m_p r_0^2 v_w}{\eta} \frac{(p-2)}{(p-1)} \frac{B_0^2}{8\pi m_e c^2 \gamma_{m,0}} \left(\frac{r}{r_0}\right)^{(2-s)}. \tag{4.16}$$

In the above Equation, v_w is the wind (stellar material expelled my massive stars) velocity and $n_{e,0}$ is the value of n_e at $t = t_0$. Hereafter, we take $v_w = 1000\,\mathrm{km\,s^{-1}}$, the typical value for Galactic Wolf-Rayet stars (see Wellons et al., 2012).

4.3 Results and Conclusion

Using all detections reported in Table 4.1, we perform a χ^2 fit of the SN 2004dk radio observations within the SSA model described in the previous Section. For all fits, we set $t_0 = 10$ days from the explosion time t_e and, following Wellons et al. (2012), $\eta = 4$. Table 4.2 shows the best fit results obtained for various scenarios. The orange fit (and corresponding orange lines in Figures 4.2 and 4.3) considers only data obtained within the first ~ 100 days from the SN 2004dk explosion, so as to exclude the radio re-brightening phase. For this fit, following the "standard" fit by Wellons et al. (2012), we fix $\alpha_r = 0.9$, $p = 3.0$, $s = 2.0$, and $\xi = 1.0$. We further set $\nu_{m,0} = 0.02\,\mathrm{GHz}$ (Soderberg et al., 2006) and allow B_0 and r_0 to vary. The obtained best fit values for B_0 and r_0 agree with those by Wellons et al. (2012). This fit yields a $\chi^2/\mathrm{dof} \approx 174/18$.

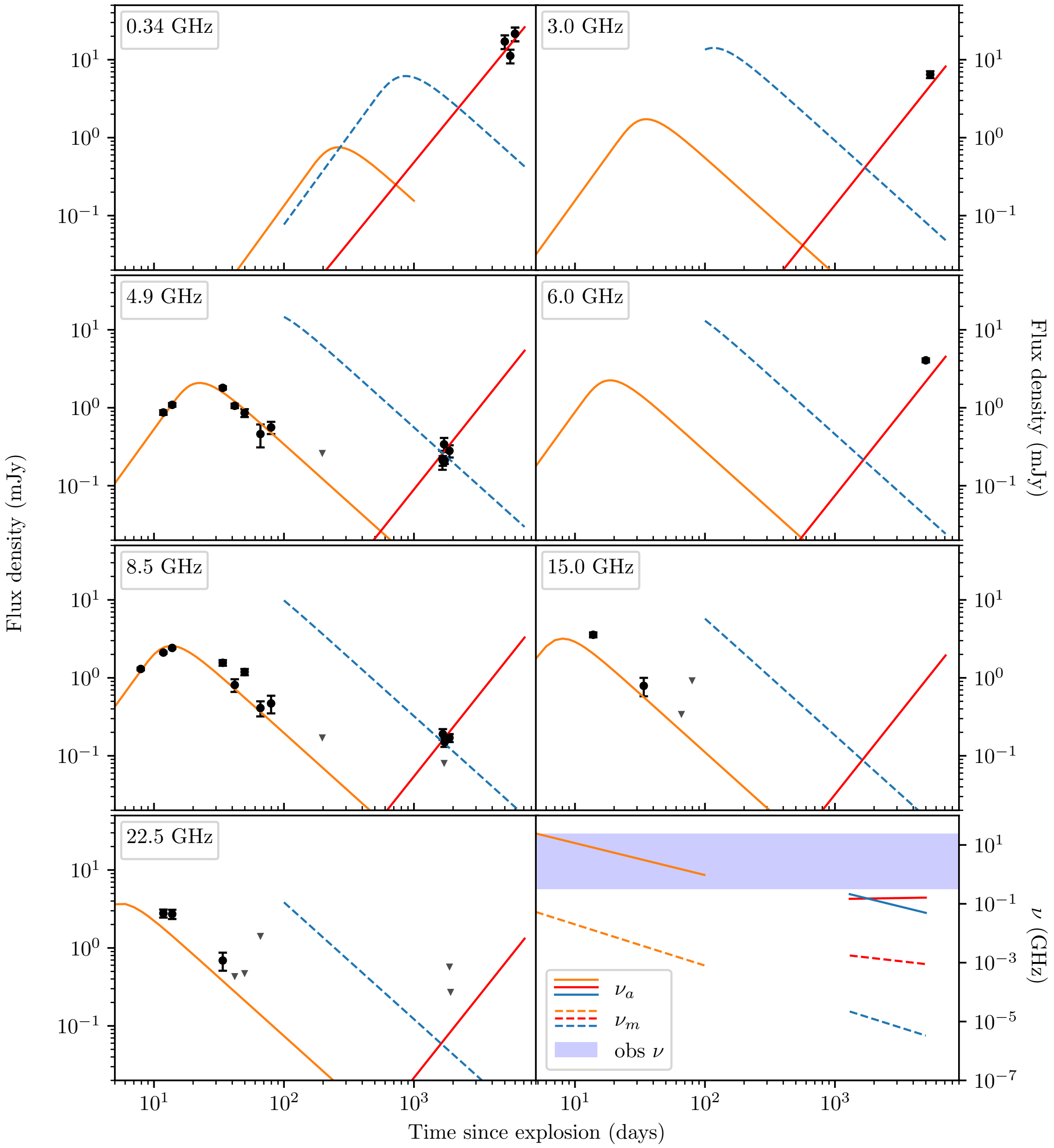

Figure 4.2. The radio light curves of SN 2004dk (data points) with the best fit SSA models (see Balasubramanian et al., 2021a). Upper limits are shown as downward pointing triangles and are not included in the fits. The orange curve is the best fit SSA model for early times ($<$ 100 days), which agrees with the fit obtained by Wellons et al. (2012). Curves at later times (red and blue) are independent SSA fits derived assuming a smooth radial evolution of the SN ejecta. The last panel of the plot shows the temporal evolution of ν_a (solid lines) and ν_m (dashed lines) and the color code is the same as that of the light curves. The extent of the light blue patch covers the observation frequencies from the lowest 340 MHz to the highest 22.5 GHz.

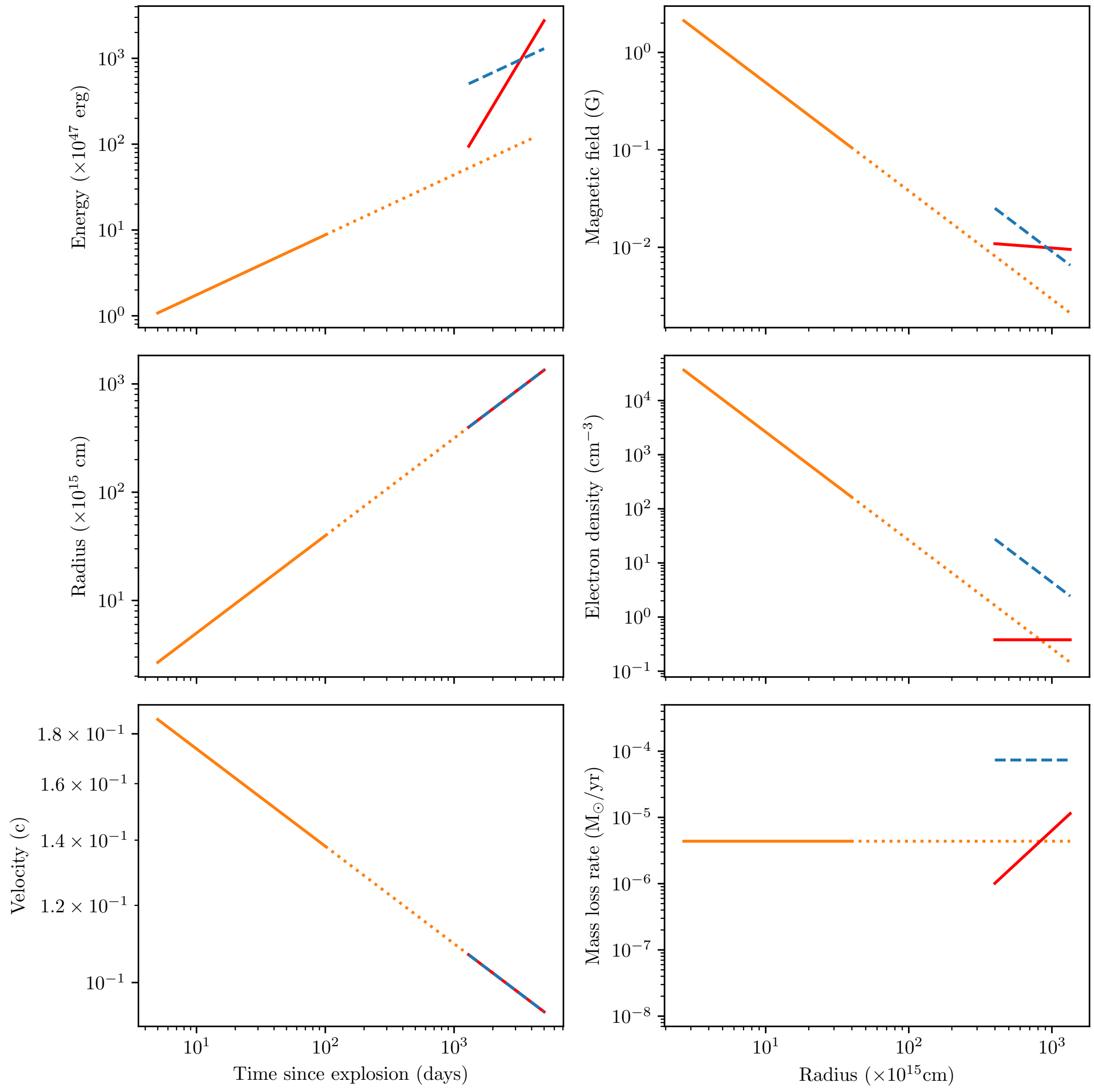

Figure 4.3. Plot of physical parameters for various fits using the same colors as the light curve plot (Figure 4.2). The panels on the left show the temporal evolution of the shocked shell properties, while the panels on the right show the radial evolution of the ambient medium and magnetic field (see Balasubramanian et al., 2021a, for detailed discussion).

Next, we perform an independent analysis of the late-time ($t \gtrsim 1000$ d since explosion) radio observations of SN 2004dk within the SSA model. All the fits assume a smooth radial evolution of the SN 2004dk ejecta with $\alpha_r = 0.9$ and $r_0 = 5.0 \times 10^{15}$ cm (as derived from the fit of the early-time data). For the red fit (and corresponding red lines in Figures 4.2 and 4.3) we fix $\nu_{m,0} = 0.02\,\mathrm{GHz}$, and $p = 3.0$, and vary B_0 and s and ξ. The best fit result yields $s \approx 0$ and a $\chi^2/\mathrm{dof} \approx 101/11$. For comparison, we also report a blue fit (and corresponding blue lines in Figures 4.2 and 4.3) where we set $s = 2$ (standard case of a smooth CSM shaped by a constant mass-loss rate from the progenitor). We see in Figure 4.2 that the blue curve does not fit the data well ($\chi^2/\mathrm{dof} \approx 495/12$).

Table 4.2. The best fit results for SN 2004dk within the SSA model. See text for discussion.

Parameters	Orange fit	Red fit	Blue fit
B_0 (G)	1.06	0.02	3.27
α_r	0.9 ^{f}	0.9 ^{f}	0.9 ^{f}
p	3.0 ^{f}	3.0 ^{f}	3.0 ^{f}
$\nu_{m,0}$ (GHz)	0.02 ^{f}	0.02 ^{f}	0.02 ^{f}
r_0 ($\times 10^{15}$ cm)	5.0	5.0 ^{f}	5.0 ^{f}
s	2.0 ^{f}	0.0	2.0 ^{f}
t_e (JD)	2453216.7 ^{f}	2453216.7 ^{f}	2453216.7 ^{f}
ξ	1.0 ^{f}	0.2	0.9
χ^2/dof	173.80/18	100.98/11	495.45/12
$\gamma_{m,0}$	2.6	20.1	1.5
E_0 (erg)	1.8 $\times 10^{47}$	4.9 $\times 10^{43}$	1.7 $\times 10^{48}$
v_0 (c)	0.17	0.17	0.17
$n_{e,0}$ (cm^{-3})	1.0 $\times 10^{4}$	3.8 $\times 10^{-1}$	1.8 $\times 10^{5}$
$\dot{M}_0$ (M$_\odot$/yr)	4.4 $\times 10^{-6}$	1.6 $\times 10^{-10}$	7.4 $\times 10^{-5}$

^{f} fixed parameter

We finally note that the results reported in Table 4.2 are somewhat dependent on the assumed value of η, given the scalings $B_0 \propto \eta^{4/17}$, $r_0 \propto \eta^{1/17}$, and $\gamma_{m,0} \propto \eta^{-2/17}$ (see Equations (5)-(7) in Soderberg et al., 2006).

From the outcome of the fits reported in the previous Section, it is evident that the standard $s = 2$ (constant mass-loss rate) and $p = 3$ scenario of the SSA model for radio SNe fits the SN 2004dk radio data well at early times ($t \lesssim 100$ days since explosion, orange fit in Figure. 4.2) and agrees with the fit obtained by Wellons et al. (2012). However, interpreting the SN 2004dk late-time radio re-brightening within the SSA scenario requires a modified CSM profile which approaches the $s = 0$ case of a constant density CSM (compare the blue fit with the red one).

Changes in the mass-loss rate profile at late times have been observed in other SNe with peculiar and variable radio light curves (e.g., Montes et al., 1998; Wellons et al., 2012; Corsi et al., 2014; Palliyaguru et al., 2019) and can be attributed to a significant evolution in the mass-loss history of the SN progenitor in the years before explosion, perhaps related to precursor eruptions to the main SN event. In Figure 4.3, we show the evolution of the mass-loss rate with radius (bottom right panel) for the late-time best fit models of SN 2004dk radio light curves, compared to that derived from the early-time data (orange).

It is particularly interesting that the fit providing the best χ^2/dof pushes the parameter s to $s = 0$, so that a constant ISM density profile seems to be favored over a stellar wind one (see Chevalier, 1982, for a discussion of the $s = 0$ case). To better understand the reasons behind this result, the following considerations are useful. As shown in the bottom-right panel in Figure 4.2, our observing radio frequencies ν (light blue patch) are such that, for all best fit models considered here, $\nu_m < \nu_a < \nu < \nu_c$. Thus, from Equation (4.12), we expect the flux to scale as:

$$f_\nu \propto t^{\frac{1}{4}(6\alpha_r - 5s\alpha_r + 10p\alpha_r - 10p - sp\alpha_r + 6)}. \tag{4.17}$$

As is evident from the above Equation, when $s = 0$ (and for $\alpha_r = 0.9$ and $p = 3$), f_ν increases with time in this frequency regime, while for $s = 2$ (blue fit in Figure 4.2) the flux decrease with time, thus making it hard to fit a re-brightening behavior such as the one observed in SN 2004dk (see Figure 4.2).

From Equations (4.16)-(4.17), when $s \neq 2$ we can further derive the following scaling of the observed flux with the mass-loss rate:

$$f_\nu \propto \left(\frac{\dot{M}}{v_w}\right)^{\frac{[\alpha_r(6-5s+10p-sp)-10p+6]}{(4\alpha_r(2-s))}}. \tag{4.18}$$

For $\alpha_r = 0.9$, $p = 3.$ and $s = 0$, one gets:

$$f_\nu \propto \left(\frac{\dot{M}}{v_w}\right)^{+1.2} \tag{4.19}$$

which shows how an increase in mass-loss rate corresponds to a re-brightening of the observed flux (see Figure. 4.3 for the radial evolution of the mass-loss rate, and Figure 4.2 for the temporal evolution of the flux density).

Now, we can compare our results with those reported in Mauerhan et al. (2018), where the velocity measurements from late-time observations of the Hα profiles yielded $v_w \approx 400\,\text{km s}^{-1}$. Assuming this to be the speed of an H-rich CSM outflow from the progenitor system, we find that the H-rich material was ejected ≈ 400 years before explosion (since the SN shock meets this CSM outflow at a radius of $r \sim 5 \times 10^{17}$ cm. The last is derived using the radius of the shell as predicted by the best fit models shown in red and blue in Figure 4.3, at the time of the earliest radio data used in those fits). This is an approximate estimate of the boundary of the H-rich CSM medium. This estimate closely agrees with the ≈ 320 years found by Mauerhan et al. (2018), which suggests a "superwind" related to pulsations of the partially ionised H envelope during the red supergiant phase (Heger et al., 1997). Computational studies of such a mechanism show that winds can cause episodic mass loss from the star, all in a timescale of $\lesssim 10^3$ years before the explosion (Yoon and Cantiello, 2010).

Pooley et al. (2019) interpret the late-time X-ray and optical behavior of SN 2004dk in the "wind bubble model", where the emission is a result of interaction with a CSM prepared by inner fast winds interacting with a previous slow wind. In this framework, the inner CSM density follows the usual radial dependence, $\rho \propto r^{-2}$, agreeing with the SSA fit obtained at early times in this work and in Wellons et al. (2012). However, the shock will then interact with a nearly constant density region before reaching the cold, dense shell (CDS), which is formed due to radiative cooling of matter in the region where the fast and slow winds collide. While a detailed comparison with the model by Pooley et al. (2019) is beyond the scope of our analysis, we note that our best fit SSA model at late-times (red curves in Figure 4.3) also hints at a constant density medium.

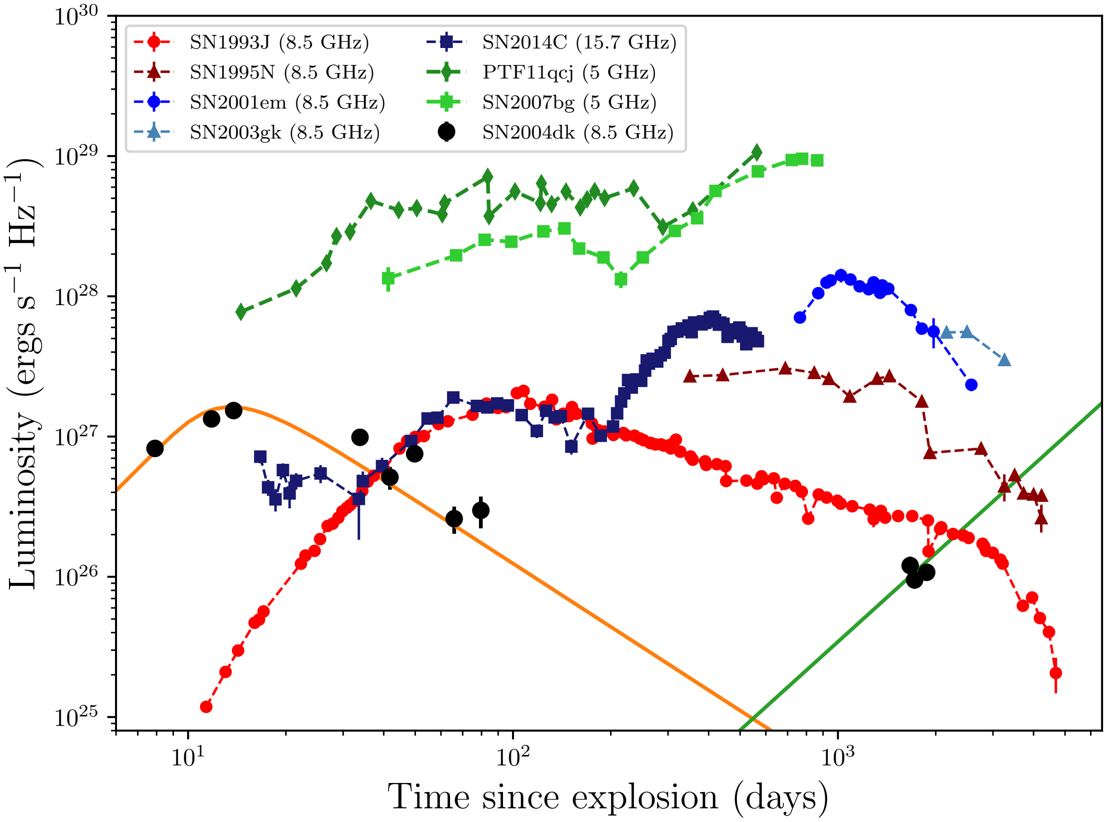

Figure 4.4. 8.5 GHz light curve of SN 2004dk (data points in black with the best fit light curves for both early and late times as plotted in 4.2) compared with late-time light curves of other SNe (type II in shades of red, type Ib in shades of blue and type Ic BL in shades of green). Data for SN 1993J from Weiler et al. (2007); SN 1995N from Chandra et al. (2009); SN 2001em from Chandra et al. (2020); SN 2003gk from Bietenholz et al. (2014); and SN 2014C from Anderson et al. (2017):SN 2007bg from Salas et al. (2013); and PTF11qcj from Corsi et al. (2014) and Palliyaguru et al. (2019).

In Figure 4.4 we compare the radio light curve of SN 2004dk with other radio SNe whose light curves have been monitored on long timescales. The radio light curve of the Type IIb SN 1993J has been modelled via a combination of free-free absorption and synchrotron self-absorption (see Section 4.2 and Weiler et al., 2007). The bumpy radio light curve of the Type IIn SN 1995N has been explained by invoking density enhancements in the CSM (Chandra et al., 2009). SN 2001em, initially classified as a Type Ib explosion, has shown evidence for late-time interaction with an H-rich CSM (ejected by the progenitor a few thousand years before explosion). It has thus been re-classified as a Type IIn SN and also as the second brightest explosion of this type in the radio (Chandra et al., 2020). In the case of the Type Ib SN 2003gk, a decaying late-time radio emission has been observed several years after explosion (Bietenholz et al., 2014). SN 2014C represents another case of a Type IIn explosion with two distinct phases of mass loss invoked for its progenitor, on timescales similar to that of SN 2004dk (Anderson et al., 2017). PTF11qcj and SN 2007bg are the most radio-loud Type Ic with broad lines, showing evidence for interaction with a CSM of varying density (Corsi et al., 2014; Palliyaguru et al., 2019; Salas et al., 2013), again qualitatively similar to the case of SN 2004dk. We note that the 8.5 GHz radio peak luminosity of SN 2004dk during its first peak of emission is comparable to the peak luminosities of the first peak of SN 2014C and SN 1993J (Figure 4.4).

In conclusion, the VLITE observations reported in this paper, combined with previously collected VLA data, favor an interpretation of SN 2004dk as a strongly CSM-interacting radio SN going through an environment shaped by the progenitor wind at first, and then followed by an ISM-like profile. The re-brightening associated with this change in density profile was first probed in 2009 (see Stockdale et al., 2009; Wellons et al., 2012; Pooley et al., 2019). Our VLITE observations confirm such re-brightening episode and suggest that the radio emission of SN 2004dk will likely continue to brighten at GHz frequencies until a second peak in the light curve is reached. However, our conclusions are also limited by the simplifications inherent in the spherically symmetric SSA model we adopted. Continued VLA/VLITE observations will be able to further test this hypothesis (or else spur a more complex theoretical modeling of this peculiar radio SN light curve).

CHAPTER 5

SUMMARY AND FUTURE PROSPECTS

In this Thesis I have discussed observations and analyses of a variety of radio transients from merger of compact objects like NSs and BHs to deaths of massive stars also known as SNe. In Chapter 1, I have introduced the concept of transients as fast changing events. The importance of studying transients in radio wavelengths lies in the unique perspective it gives on the study of fast explosions, helping to probe relativistic particles in often strong magnetic environments. Such studies can help unveil properties of the ejecta from explosive transients, physical parameters of the medium surrounding the transients, etc. In this chapter, I have also emphasized GRBs as some of the most energetic explosions in the cosmos. While many aspects of the physics of GRBs are well known, there still remains many questions about them, from their energetics to the properties of the central engines that drive the jets that make the GRBs, and subsequently emit the afterglows. We also saw the possible links of these energetic emissions to two cataclysmic events: mergers of compact objects and core collapse SNe. Continued study of these related groups of transients at various wavelengths is likely to help us solve some of the open problems.

In Chapter 2, I presented my work on the radio follow-up studies of GW170817, the first binary NS merger to be observed both in GWs and across all bands of the EM spectrum. I summarized the detection of both GWs and the two types of EM emission, the non-thermal jet+cocoon emission and the quasi-thermal kilonova emission. The importance of radio observations in understanding the morphology of GW170817 cannot be understated. The radio non-thermal emission seen from the jet+cocoon had faded below detection limits at the epoch of about 3 years since merger. Models predicted a re-brightening to be visible at X-ray and radio wavelengths due to the interaction of the isotropic kilonova ejecta with the interstellar medium after a few years from merger. I have worked on observational campaigns with the Jansky VLA to look for this proposed re-brightening (Balasubramanian et al., 2021b, 2022). While no re-brightening has been detected as of 4.5 years after merger, my work has placed strong constraints on particle acceleration mechanisms, the energy-speed distribution of kilonova ejecta and on the equation of state of NSs. I also made predictions on what to expect from observations of similar sensitivity at 7.5 years from merger.

In Chapter 3 I have summarized my contributions to radio follow-up observations of GW events from the third observing run (O3) of LIGO and Virgo. The first event we studied was S191216ap (Bhakta et al., 2021), a binary BH merger. Although it is not very likely for binary BH mergers to emit EM waves, the discovery of a possible EM counterpart to GW150914 has excited the community to come up with plausible models. No counterpart for S191216ap was found in our observations, but we placed deeper constraints on the physical parameters of a possible jet from binary BHs. The next transient I studied was AT2019wxt (Hinna et al. 2022 in prep) which was discovered in followup campaigns for the GW event S191213bg. S191213bg was later dropped as a possible high-confidence GW event after off-line analysis of the GW data. However, the peculiar AT2019wxt was still an interesting source. The optical light curve shows a double peak structure characteristic of stripped envelope core collapse SNe. The radio and X-ray observations do not show evidence of a variable source in the location of the transient. Lastly, I have carried out radio observations of the 50% confidence region of the GW event GW190814, a probable NSBH merger with the most extreme difference in the masses of the constituent objects observed to date. At the time of writing, I am finalizing this work (paper in prep). These follow-up campaigns have helped inform future GW observations and prepare the community for follow-up observations in the upcoming runs of the LIGO and Virgo detectors.

My work with the observations of the late-time re-brightening of the radio loud SN 2004dk (Balasubramanian et al., 2021a) was described in Chapter 4. The study of radio bright core-collapse SNe is motivated by the fact that a small fraction of these emit jets, and we don't know what separates normal core collapse SNe from these special ones. SN2004dk shows a peculiar light curve with a re-brightening in radio still observed $\sim$15 years after the SN. Combined with late-time optical spectra, we have shown the evidence of the SN shock wave interacting with envelopes of the massive star ejected before the star collapsed in a SN. This study also helped us map the mass loss of the progenitor up to $\approx$400 years before the SN explosion.

With the updates to existing GW detectors, and upcoming third generation GW detectors like the Einstein Telescope (ET) and Cosmic Explorer (CE; see e.g., Abbott et al., 2017a; Mills et al., 2018; Singh et al., 2021), the number of candidate merger events which may be accompanied with EM counterparts will grow by orders of magnitude. To keep up with the rising number of sources, new radio facilities like the next generation VLA (ngVLA) will play a vital role in helping with follow-up observations like the ones described in Chapters 2 and 3. A population of multi-messenger sources will help us paint a better picture about the physics of mergers and short GRBs. Finally, with more sensitive GW detectors such as CE, extreme stripped-envelope core-collapse SNe may become sources of interest also for multi-messenger studies across the GW spectrum (see e.g., Michaely and Perets, 2018; Nakamura et al., 2016).

BIBLIOGRAPHY

B. P. Abbott, R. Abbott, T. D. Abbott, M. R. Abernathy, K. Ackley, et al. Exploring the sensitivity of next generation gravitational wave detectors. *Classical and Quantum Gravity*, 34(4):044001, February 2017a.

B. P. Abbott, R. Abbott, T. D. Abbott, F. Acernese, K. Ackley, et al. GW170817: Observation of Gravitational Waves from a Binary Neutron Star Inspiral. Phys. Rev. Lett., 119(16):161101, October 2017b.

B. P. Abbott, R. Abbott, T. D. Abbott, F. Acernese, K. Ackley, et al. Multi-messenger Observations of a Binary Neutron Star Merger. ApJ, 848(2):L12, October 2017c.

B. P. Abbott, R. Abbott, T. D. Abbott, F. Acernese, K. Ackley, et al. GW170817: Measurements of Neutron Star Radii and Equation of State. Phys. Rev. Lett., 121 (16):161101, October 2018.

B. P. Abbott, R. Abbott, T. D. Abbott, F. Acernese, K. Ackley, et al. Properties of the Binary Neutron Star Merger GW170817. *Physical Review X*, 9(1):011001, January 2019.

R. Abbott, T. D. Abbott, S. Abraham, F. Acernese, K. Ackley, et al. GWTC-2: Compact Binary Coalescences Observed by LIGO and Virgo During the First Half of the Third Observing Run. *arXiv e-prints*, art. arXiv:2010.14527, October 2020a.

R. Abbott, T. D. Abbott, S. Abraham, F. Acernese, K. Ackley, et al. GW190814: Gravitational Waves from the Coalescence of a 23 Solar Mass Black Hole with a 2.6 Solar Mass Compact Object. ApJ, 896(2):L44, June 2020b.

R. Abbott, T. D. Abbott, S. Abraham, F. Acernese, K. Ackley, et al. GWTC-2: Compact Binary Coalescences Observed by LIGO and Virgo during the First Half of the Third Observing Run. *Physical Review X*, 11(2):021053, April 2021.

F. Acernese, M. Agathos, K. Agatsuma, D. Aisa, N. Allemandou, et al. Advanced Virgo: a second-generation interferometric gravitational wave detector. *Classical and Quantum Gravity*, 32(2):024001, January 2015.

K. Ackley, L. Amati, C. Barbieri, F. E. Bauer, S. Benetti, et al. Observational constraints on the optical and near-infrared emission from the neutron star-black hole binary merger candidate S190814bv. A&A, 643:A113, November 2020.

M. Ageron, B. Baret, A. Coleiro, M. Colomer, D. Dornic, et al. LIGO/Virgo S191213g : no neutrino counterpart candidate in ANTARES search. *GRB Coordinates Network*, 26404:1, December 2019.

T. Akutsu, M. Ando, K. Arai, Y. Arai, S. Araki, et al. Overview of KAGRA: Calibration, detector characterization, physical environmental monitors, and the geophysics interferometer. *Progress of Theoretical and Experimental Physics*, 2021(5): 05A102, May 2021.

K. D. Alexander, E. Berger, W. Fong, P. K. G. Williams, C. Guidorzi, et al. The Electromagnetic Counterpart of the Binary Neutron Star Merger LIGO/Virgo GW170817. VI. Radio Constraints on a Relativistic Jet and Predictions for Late-time Emission from the Kilonova Ejecta. ApJ, 848(2):L21, October 2017.

K. D. Alexander, G. Schroeder, K. Paterson, W. Fong, P. Cowperthwaite, et al. A Late-time Galaxy-targeted Search for the Radio Counterpart of GW190814. ApJ, 923(1):66, December 2021.

J. Alvarez-Muniz, F. Pedreira, E. Zas, K. H. Kampert, M. Schimp, and Pierre Auger Collaboration. LIGO/Virgo S191213g: No neutrino candidates at Pierre Auger Observatory. *GRB Coordinates Network*, 26423:1, December 2019.

G. E. Anderson, A. Horesh, K. P. Mooley, A. P. Rushton, R. P. Fender, et al. The peculiar mass-loss history of SN 2014C as revealed through AMI radio observations. MNRAS, 466(3):3648–3662, April 2017.

Igor Andreoni, Shreya Anand, Eric Bellm, Erik Kool, Dan Perley, et al. LIGO/Virgo S191213g: Candidates from the Zwicky Transient Facility. *GRB Coordinates Network*, 26424:1, December 2019.

Igor Andreoni, Daniel A. Goldstein, Mansi M. Kasliwal, Peter E. Nugent, Rongpu Zhou, et al. GROWTH on S190814bv: Deep Synoptic Limits on the

Optical/Near-infrared Counterpart to a Neutron Star-Black Hole Merger. ApJ, 890(2):131, February 2020.

S Antier, S Agayeva, V Aivazyan, S Alishov, E Arbouch, et al. The first six months of the Advanced LIGO's and Advanced Virgo's third observing run with GRANDMA. *Monthly Notices of the Royal Astronomical Society*, 492(3):3904–3927, 11 2019. ISSN 0035-8711.

Kyle Artkop, Rachel Smith, Alessandra Corsi, Simona Giacintucci, Wendy M. Peters, et al. Radio Follow-up of a Candidate γ-Ray Transient in the Sky Localization Area of GW170608. ApJ, 884(1):16, October 2019.

A. Balasubramanian, A. Corsi, E. Polisensky, T. E. Clarke, and N. E. Kassim. Radio Observations of SN2004dk with VLITE Confirm Late-time Rebrightening. ApJ, 923(1):32, December 2021a.

Arvind Balasubramanian, Alessandra Corsi, Kunal P. Mooley, Murray Brightman, Gregg Hallinan, et al. Continued Radio Observations of GW170817 3.5 yr Post-merger. ApJ, 914(1):L20, June 2021b.

Arvind Balasubramanian, Alessandra Corsi, Kunal P. Mooley, Kenta Hotokezaka, David L. Kaplan, et al. GW170817 4.5 years after merger: Dynamical ejecta afterglow constraints. *arXiv e-prints*, art. arXiv:2205.14788, May 2022.

S. D. Barthelmy, A. Y. Lien, D. M. Palmer, T. Sakamoto, A. P. Beardmore, et al. LIGO/Virgo S191213g: no counterpart candidates in the Swift/BAT observations. *GRB Coordinates Network*, 26410:1, December 2019.

J. Becerra-Gonzalez and a larger Collaboration. LIGO/Virgo S191213g: AT2019wxt 10.4m GTC spectroscopy. *GRB Coordinates Network*, 26521:1, December 2019.

Paz Beniamini, Dimitrios Giannios, George Younes, Alexander J. van der Horst, and Chryssa Kouveliotou. Compton echoes from nearby gamma-ray bursts. MNRAS, 476(4):5621–5628, June 2018.

E. Berger, S. R. Kulkarni, D. A. Frail, and A. M. Soderberg. A Radio Survey of Type Ib and Ic Supernovae: Searching for Engine-driven Supernovae. ApJ, 599 (1):408–418, December 2003.

D. Bhakta, K. P. Mooley, A. Corsi, A. Balasubramanian, D. Dobie, et al. The JAGWAR Prowls LIGO/Virgo O3 Paper I: Radio Search of a Possible Multimessenger Counterpart of the Binary Black Hole Merger Candidate S191216ap. ApJ, 911(2):77, April 2021.

M. F. Bietenholz, F. De Colle, J. Granot, N. Bartel, and A. M. Soderberg. Radio limits on off-axis GRB afterglows and VLBI observations of SN 2003gk. MNRAS, 440 (1):821–832, May 2014.

R. D. Blandford and C. F. McKee. Fluid dynamics of relativistic blast waves. *Physics of Fluids*, 19:1130–1138, Aug 1976.

Geoffrey C. Bower, Destry Saul, Joshua S. Bloom, Alberto Bolatto, Alexei V. Filippenko, et al. Submillijansky Transients in Archival Radio Observations. ApJ, 666 (1):346–360, September 2007.

S. Brennan, T. Killestein, M. Fraser, P. Jonker, K. Maguire, et al. LIGO/Virgo S191213g: WHT spectroscopy of candidate counterparts. *GRB Coordinates Network*, 26429:1, December 2019.

A. J. Castro-Tirado, Y. D. Hu, A. F. Valeev, V. V. Sokolov, E. Fernandez-Garcia, et al. LIGO/Virgo S191213g: AT2019wnh, AT2019wnk and AT2019wrt 10.4m GTC spectroscopy. *GRB Coordinates Network*, 26492:1, December 2019.

Y. Cendes, T. Eftekhari, E. Berger, and E. Polisensky. Radio Monitoring of the Tidal Disruption Event Swift J164449.3+573451. IV. Continued Fading and Nonrelativistic Expansion. ApJ, 908(2):125, February 2021.

Poonam Chandra and Dale A. Frail. A Radio-selected Sample of Gamma-Ray Burst Afterglows. ApJ, 746(2):156, February 2012.

Poonam Chandra, Vikram V. Dwarkadas, Alak Ray, Stefan Immler, and David Pooley. X-rays from the Explosion Site: 15 Years of Light Curves of SN 1993J. ApJ, 699(1):388–399, July 2009.

Poonam Chandra, Roger A. Chevalier, Nikolai Chugai, Dan Milisavljevic, and Claes Fransson. Supernova Interaction with a Dense Detached Shell in SN 2001em. ApJ, 902(1):55, October 2020.

Phil Charles and Aarran Shaw. The transient universe. *Astronomy and Geophysics*, 54(6):6.15–6.16, December 2013.

R. A. Chevalier. Self-similar solutions for the interaction of stellar ejecta with an external medium. ApJ, 258:790–797, July 1982.

Roger A. Chevalier. Synchrotron Self-Absorption in Radio Supernovae. ApJ, 499 (2):810–819, May 1998.

Roger A. Chevalier and Claes Fransson. Circumstellar Emission from Type Ib and Ic Supernovae. ApJ, 651(1):381–391, November 2006.

Tracy E. Clarke, Rick A. Perley, Namir E. Kassim, Brian C. Hicks, Frazer N. Owen, et al. The expanded very large array low band upgrade. In *General Assembly and Scientific Symposium*, page E5, August 2011.

Tracy E. Clarke, Namir E. Kassim, Walter Brisken, Joseph Helmboldt, Wendy Peters, et al. Commensal low frequency observing on the NRAO VLA: VLITE status and future plans. In *Ground-based and Airborne Telescopes VI*, volume 9906 of *Society of Photo-Optical Instrumentation Engineers (SPIE) Conference Series*, page 99065B, August 2016.

V. Connaughton, E. Burns, A. Goldstein, L. Blackburn, M. S. Briggs, et al. Fermi GBM Observations of LIGO Gravitational-wave Event GW150914. ApJ, 826(1): L6, July 2016.

A. Corsi, E. O. Ofek, A. Gal-Yam, D. A. Frail, S. R. Kulkarni, et al. A Multiwavelength Investigation of the Radio-loud Supernova PTF11qcj and its Circumstellar Environment. ApJ, 782(1):42, February 2014.

A. Corsi, A. Gal-Yam, S. R. Kulkarni, D. A. Frail, P. A. Mazzali, et al. Radio Observations of a Sample of Broad-line Type IC Supernovae Discovered by PTF/IPTF: A Search for Relativistic Explosions. ApJ, 830(1):42, October 2016.

Alessandra Corsi, Gregg W. Hallinan, Davide Lazzati, Kunal P. Mooley, Eric J. Murphy, et al. An Upper Limit on the Linear Polarization Fraction of the GW170817 Radio Continuum. ApJ, 861(1):L10, July 2018.

W. D. Cotton. Obit: A Development Environment for Astronomical Algorithms. PASP, 120(866):439, April 2008.

D. A. Coulter, R. J. Foley, C. D. Kilpatrick, M. R. Drout, A. L. Piro, et al. Swope Supernova Survey 2017a (SSS17a), the optical counterpart to a gravitational wave source. *Science*, 358(6370):1556–1558, December 2017.

S. Cutini, N. Omodei, M. Axelsson, E. Bissaldi, D. Kocevski, et al. LIGO/Virgo S191213g: No counterpart candidates in Fermi-LAT observations. *GRB Coordinates Network*, 26412:1, December 2019.

Soumi De, Daniel Finstad, James M. Lattimer, Duncan A. Brown, Edo Berger, and Christopher M. Biwer. Tidal Deformabilities and Radii of Neutron Stars from the Observation of GW170817. Phys. Rev. Lett., 121(9):091102, August 2018.

M. de Pasquale, L. Piro, B. Gendre, L. Amati, L. A. Antonelli, et al. The BeppoSAX catalog of GRB X-ray afterglow observations. A&A, 455(3):813–824, September 2006.

A. T. Deller, S. J. Tingay, M. Bailes, and C. West. DiFX: A Software Correlator for Very Long Baseline Interferometry Using Multiprocessor Computing Environments. PASP, 119(853):318–336, March 2007.

Gotz Diego, Alexander Lutovinov, V. Savchenko, C. Ferrigno, J. Rodi, et al. LIGO/Virgo S191213g: No counterpart candidates in INTEGRAL SPI-ACS prompt observation. *GRB Coordinates Network*, 26401:1, December 2019.

D. Dobie, A. Stewart, K. Hotokezaka, Tara Murphy, D. L. Kaplan, et al. A comprehensive search for the radio counterpart of GW190814 with the Australian Square Kilometre Array Pathfinder. MNRAS, 510(3):3794–3805, March 2022.

Dougal Dobie, David L. Kaplan, Tara Murphy, Emil Lenc, Kunal P. Mooley, et al. A Turnover in the Radio Light Curve of GW170817. ApJ, 858(2):L15, May 2018.

Dougal Dobie, Adam Stewart, Tara Murphy, Emil Lenc, Ziteng Wang, et al. An ASKAP Search for a Radio Counterpart to the First High-significance Neutron Star-Black Hole Merger LIGO/Virgo S190814bv. ApJ, 887(1):L13, December 2019.

N. Elias-Rosa, S. Benetti, S. Piranomonte, A. Melandri, L. di Fabrizio, and Grawita Collabration. LIGO/Virgo S191213g: GRAWITA TNG classification of ZTF19acykzsk. *GRB Coordinates Network*, 26428:1, December 2019.

Gerald J. Fishman, Charles A. Meegan, Robert B. Wilson, Martin N. Brock, John M. Horack, et al. The First BATSE Gamma-Ray Burst Catalog. ApJS, 92:229, May 1994.

H. A. Flewelling, E. A. Magnier, K. C. Chambers, J. N. Heasley, C. Holmberg, et al. The Pan-STARRS1 Database and Data Products. ApJS, 251(1):7, November 2020.

W. Fong, P. K. Blanchard, K. D. Alexander, J. Strader, R. Margutti, et al. The Optical Afterglow of GW170817: An Off-axis Structured Jet and Deep Constraints on a Globular Cluster Origin. ApJ, 883(1):L1, September 2019.

D. A. Frail, A. M. Soderberg, S. R. Kulkarni, E. Berger, S. Yost, et al. Accurate Calorimetry of GRB 030329. ApJ, 619(2):994–998, February 2005.

C. Fremling. LIGO/Virgo S191213g: Palomar 60-inch imaging of AT2019wxt. *GRB Coordinates Network*, 26500:1, December 2019.

C. Fremling, T. Ahumada, L. P. Singer, K. de, M. M. Kasliwal, et al. LIGO/Virgo S191213g: GMOS-N spectroscopy shows ZTF19acykzsk/AT2019wqj is a SN II. *GRB Coordinates Network*, 26427:1, December 2019.

G. Ghirlanda, O. S. Salafia, Z. Paragi, M. Giroletti, J. Yang, et al. Compact radio emission indicates a structured jet was produced by a binary neutron star merger. *Science*, 363(6430):968–971, March 2019.

Andreja Gomboc. Unveiling the secrets of gamma ray bursts. *Contemporary Physics*, 53(4):339–355, July 2012.

S. Gomez, G. Hosseinzadeh, P. S. Cowperthwaite, V. A. Villar, E. Berger, et al. A Galaxy-targeted Search for the Optical Counterpart of the Candidate NS-BH Merger S190814bv with Magellan. ApJ, 884(2):L55, October 2019.

B. P. Gompertz, A. J. Levan, and N. R. Tanvir. A Search for Neutron Star-Black Hole Binary Mergers in the Short Gamma-Ray Burst Population. ApJ, 895(1):58, May 2020.

J. Graham and W. Li. Supernova 2004dk in NGC 6118. *Central Bureau Electronic Telegrams*, 75:1, August 2004.

Daryl Haggard, Melania Nynka, John J. Ruan, Vicky Kalogera, S. Bradley Cenko, et al. A Deep Chandra X-Ray Study of Neutron Star Coalescence GW170817. ApJ, 848(2):L25, October 2017.

A. Hajela, R. Margutti, K. D. Alexander, A. Kathirgamaraju, A. Baldeschi, et al. Two Years of Nonthermal Emission from the Binary Neutron Star Merger GW170817: Rapid Fading of the Jet Afterglow and First Constraints on the Kilonova Fastest Ejecta. ApJ, 886(1):L17, November 2019.

A. Hajela, R. Margutti, K. D. Alexander, W. Fong, E. Berger, et al. Chandra observations of GW170817 at 3.3 years since merger (Full report). *GRB Coordinates Network*, 29055:1, December 2020a.

A. Hajela, R. Margutti, A. Kathirgamaraju, D. Giannios, T. Laskar, et al. X-Ray Emission from GW170817 ˜2.5 years After the Merger. *Research Notes of the American Astronomical Society*, 4(5):68, May 2020b.

A. Hajela, R. Margutti, K. D. Alexander, J. S. Bright, T. Laskar, and E. Berger. Chandra observation of GW170817 at 1575 days since merger (all epochs). *GRB Coordinates Network*, 31231:1, December 2021a.

A. Hajela, R. Margutti, J. Bright, K. D. Alexander, W. Fong, et al. Continued Chandra observations of GW170817 at 3.3 years since merger. *GRB Coordinates Network*, 29375:1, January 2021b.

A. Hajela, R. Margutti, J. S. Bright, K. D. Alexander, B. D. Metzger, et al. Evidence for X-Ray Emission in Excess to the Jet-afterglow Decay 3.5 yr after the Binary Neutron Star Merger GW 170817: A New Emission Component. ApJ, 927(1): L17, March 2022.

G. Hallinan, A. Corsi, K. P. Mooley, K. Hotokezaka, E. Nakar, et al. A radio counterpart to a neutron star merger. *Science*, 358(6370):1579–1583, December 2017.

P. J. Hancock, T. Murphy, B. M. Gaensler, A. Hopkins, and J. R. Curran. Compact continuum source finding for next generation radio surveys. MNRAS, 422(2): 1812–1824, May 2012.

HAWC Collaboration. LIGO/Virgo S191216ap: HAWC gamma-ray sub-threshold event coincident with LIGO/Virgo and IceCube localizations. *GRB Coordinates Network*, 26472:1, December 2019.

A. Heger, L. Jeannin, N. Langer, and I. Baraffe. Pulsations in red supergiants with high L/M ratio. Implications for the stellar and circumstellar structure of supernova progenitors. A&A, 327:224–230, November 1997.

J. A. Högbom. Aperture Synthesis with a Non-Regular Distribution of Interferometer Baselines. A&AS, 15:417, June 1974.

Ulrich Hopp, Matthias Kluge, Claus Goessl, Christoph Ries, and Michael Schmidt. LIGO/Virgo S191213g: AT2019wxt Wendelstein optical observations. *GRB Coordinates Network*, 27057:1, February 2020.

K. Hotokezaka, S. Nissanke, G. Hallinan, T. J. W. Lazio, E. Nakar, and T. Piran. Radio Counterparts of Compact Binary Mergers Detectable in Gravitational Waves: A Simulation for an Optimized Survey. ApJ, 831(2):190, November 2016.

Kenta Hotokezaka and Tsvi Piran. Mass ejection from neutron star mergers: different components and expected radio signals. MNRAS, 450(2):1430–1440, June 2015.

Kenta Hotokezaka, Kenta Kiuchi, Masaru Shibata, Ehud Nakar, and Tsvi Piran. Synchrotron Radiation from the Fast Tail of Dynamical Ejecta of Neutron Star Mergers. ApJ, 867(2):95, November 2018.

M. E. Huber, S. J. Smartt, O. McBrien, and K. C. Chambers A. S. B. Schultz. LIGO/Virgo S191213g: Pan-STARRS monitoring shows PS19hgw (AT2019wxt) to be fading quickly. *GRB Coordinates Network*, 26577:1, December 2019.

IceCube Collaboration. LIGO/Virgo S191213g: Upper limits from IceCube neutrino searches. *GRB Coordinates Network*, 26399:1, December 2019.

John David Jackson. *Classical Electrodynamics, 3rd Edition*. 1998.

S. Johnston, R. Taylor, M. Bailes, N. Bartel, C. Baugh, et al. Science with ASKAP. The Australian square-kilometre-array pathfinder. *Experimental Astronomy*, 22 (3):151–273, December 2008.

J. L. Jonas. MeerKAT - The South African Array With Composite Dishes and Wide-Band Single Pixel Feeds. *IEEE Proceedings*, 97(8):1522–1530, August 2009.

W. A. Joye and E. Mandel. New Features of SAOImage DS9. In H. E. Payne, R. I. Jedrzejewski, and R. N. Hook, editors, *Astronomical Data Analysis Software and Systems XII*, volume 295 of *Astronomical Society of the Pacific Conference Series*, page 489, January 2003.

Daniel Kasen, Brian Metzger, Jennifer Barnes, Eliot Quataert, and Enrico Ramirez-Ruiz. Origin of the heavy elements in binary neutron-star mergers from a gravitational-wave event. Nature, 551(7678):80–84, November 2017.

M. M. Kasliwal, E. Nakar, L. P. Singer, D. L. Kaplan, D. O. Cook, et al. Illuminating gravitational waves: A concordant picture of photons from a neutron star merger. *Science*, 358(6370):1559–1565, December 2017.

Adithan Kathirgamaraju, Dimitrios Giannios, and Paz Beniamini. Observable features of GW170817 kilonova afterglow. MNRAS, 487(3):3914–3921, August 2019.

Albert Kong. LIGO/Virgo S191213g: Lulin Follow-up Observations of AT2019wxt. *GRB Coordinates Network*, 26503:1, December 2019.

H. A. Krimm, S. T. Holland, R. H. D. Corbet, A. B. Pearlman, P. Romano, et al. VizieR Online Data Catalog: The Swift/BAT hard X-ray transient monitor (Krimm+, 2013). *VizieR Online Data Catalog*, art. J/ApJS/209/14, November 2013.

Brajesh Kumar, S. B. Pandey, D. K. Sahu, J. Vinko, A. S. Moskvitin, et al. Light curve and spectral evolution of the Type IIb supernova 2011fu. MNRAS, 431(1): 308–321, May 2013.

M. Lacy, S. A. Baum, C. J. Chandler, S. Chatterjee, T. E. Clarke, et al. The Karl G. Jansky Very Large Array Sky Survey (VLASS). Science Case and Survey Design. PASP, 132(1009):035001, March 2020.

Davide Lazzati, Rosalba Perna, Brian J. Morsony, Diego Lopez-Camara, Matteo Cantiello, et al. Late Time Afterglow Observations Reveal a Collimated Relativistic Jet in the Ejecta of the Binary Neutron Star Merger GW170817. Phys. Rev. Lett., 120(24):241103, June 2018.

LIGO Scientific Collaboration and Virgo Collaboration. LIGO/Virgo S191213g: Identification of a GW compact binary merger candidate. *GRB Coordinates Network*, 26402:1, December 2019a.

LIGO Scientific Collaboration and Virgo Collaboration. LIGO/Virgo S191213g: Updated Sky Localization. *GRB Coordinates Network*, 26417:1, December 2019b.

LIGO Scientific Collaboration and Virgo Collaboration. LIGO/Virgo S191216ap: Identification of a GW compact binary merger candidate. *GRB Coordinates Network*, 26454:1, December 2019c.

LIGO Scientific Collaboration and Virgo Collaboration. LIGO/Virgo S191216ap: Updated Source Classification. *GRB Coordinates Network*, 26570:1, December 2019d.

LIGO Scientific Collaboration, J. Aasi, B. P. Abbott, R. Abbott, T. Abbott, et al. Advanced LIGO. *Classical and Quantum Gravity*, 32(7):074001, April 2015.

Itai Linial and Re'em Sari. Cooling off with a kilonova - lower limit on the expansion velocity of GW170817. MNRAS, 483(1):624–627, February 2019.

Keiichi Maeda. Young Supernovae as Experimental Sites for Studying the Electron Acceleration Mechanism. ApJ, 762(2):L24, January 2013.

S. Makhathini, K. P. Mooley, M. Brightman, K. Hotokezaka, A. J. Nayana, et al. The Panchromatic Afterglow of GW170817: The Full Uniform Data Set, Modeling, Comparison with Previous Results, and Implications. ApJ, 922(2):154, December 2021.

Ben Margalit and Tsvi Piran. Shock within a shock: revisiting the radio flares of NS merger ejecta and gamma-ray burst-supernovae. MNRAS, 495(4):4981–4993, July 2020.

R. Margutti, E. Berger, W. Fong, C. Guidorzi, K. D. Alexander, et al. The Electromagnetic Counterpart of the Binary Neutron Star Merger LIGO/Virgo GW170817. V. Rising X-Ray Emission from an Off-axis Jet. ApJ, 848(2):L20, October 2017a.

R. Margutti, K. D. Alexander, X. Xie, L. Sironi, B. D. Metzger, et al. The Binary Neutron Star Event LIGO/Virgo GW170817 160 Days after Merger: Synchrotron Emission across the Electromagnetic Spectrum. ApJ, 856(1):L18, March 2018.

Raffaella Margutti, A. Kamble, D. Milisavljevic, E. Zapartas, S. E. de Mink, et al. Ejection of the Massive Hydrogen-rich Envelope Timed with the Collapse of the Stripped SN 2014C. ApJ, 835(2):140, February 2017b.

J.M. Marr, R.L. Snell, and S.E. Kurtz. *Fundamentals of Radio Astronomy: Observational Methods*. Series in Astronomy and Astrophysics. Taylor & Francis, 2015. ISBN 9781420076769.

Jon C. Mauerhan, Alexei V. Filippenko, WeiKang Zheng, Thomas G. Brink, Melissa L. Graham, et al. Stripped-envelope supernova SN 2004dk is now interacting with hydrogen-rich circumstellar material. MNRAS, 478(4):5050–5055, August 2018.

O. McBrien, S. J. Smartt, K. W. Smith, D. R. Young, J. Gillanders. S. Srivastav, et al. LIGO/Virgo S191213g: Pan-STARRS1 discovery of a potential optical counterpart. *GRB Coordinates Network*, 26485:1, December 2019.

J. P. McMullin, B. Waters, D. Schiebel, W. Young, and K. Golap. CASA Architecture and Applications. In R. A. Shaw, F. Hill, and D. J. Bell, editors, *Astronomical Data Analysis Software and Systems XVI*, volume 376 of *Astronomical Society of the Pacific Conference Series*, page 127, October 2007a.

J. P. McMullin, B. Waters, D. Schiebel, W. Young, and K. Golap. CASA Architecture and Applications. In R. A. Shaw, F. Hill, and D. J. Bell, editors, *Astronomical Data Analysis Software and Systems XVI*, volume 376 of *Astronomical Society of the Pacific Conference Series*, page 127, October 2007b.

P. Mészáros. Gamma-ray bursts. *Reports on Progress in Physics*, 69(8):2259–2321, August 2006.

Brian D. Metzger. Welcome to the Multi-Messenger Era! Lessons from a Neutron Star Merger and the Landscape Ahead. *arXiv e-prints*, art. arXiv:1710.05931, October 2017.

Erez Michaely and Hagai B. Perets. Supernova and Prompt Gravitational-wave Precursors to LIGO Gravitational-wave Sources and Short GRBs. ApJ, 855(1): L12, March 2018.

Enno Middelberg, Robert J. Sault, and Michael J. Kesteven. The ATCA Seeing Monitor. PASA, 23(4):147–153, February 2006.

Cameron Mills, Vaibhav Tiwari, and Stephen Fairhurst. Localization of binary neutron star mergers with second and third generation gravitational-wave detectors. *Phys. Rev. D*, 97:104064, May 2018.

Niruj Mohan and David Rafferty. PyBDSF: Python Blob Detection and Source Finder, February 2015.

Marcos J. Montes, Schuyler D. Van Dyk, Kurt W. Weiler, Richard A. Sramek, and Nino Panagia. Radio Observations of SN 1980K: Evidence for Rapid Presupernova Evolution. ApJ, 506(2):874–879, October 1998.

K. P. Mooley, D. A. Frail, E. O. Ofek, N. A. Miller, S. R. Kulkarni, and A. Horesh. Sensitive Search for Radio Variables and Transients in the Extended Chandra Deep Field South. ApJ, 768(2):165, May 2013a.

K. P. Mooley, D. A. Frail, E. O. Ofek, N. A. Miller, S. R. Kulkarni, and A. Horesh. Sensitive Search for Radio Variables and Transients in the Extended Chandra Deep Field South. ApJ, 768(2):165, May 2013b.

K. P. Mooley, G. Hallinan, S. Bourke, A. Horesh, S. T. Myers, et al. The Caltech-NRAO Stripe 82 Survey (CNSS). I. The Pilot Radio Transient Survey In 50 deg^2. ApJ, 818(2):105, February 2016.

K. P. Mooley, A. T. Deller, O. Gottlieb, E. Nakar, G. Hallinan, et al. Superluminal motion of a relativistic jet in the neutron-star merger GW170817. Nature, 561 (7723):355–359, September 2018a.

K. P. Mooley, D. A. Frail, D. Dobie, E. Lenc, A. Corsi, et al. A Strong Jet Signature in the Late-time Light Curve of GW170817. ApJ, 868(1):L11, November 2018b.

K. P. Mooley, D. A. Frail, S. T. Myers, S. R. Kulkarni, K. Hotokezaka, et al. A Case Study of On-the-fly Wide-field Radio Imaging Applied to the Gravitational Wave Event GW151226. ApJ, 857(2):143, April 2018c.

K. P. Mooley, E. Nakar, K. Hotokezaka, G. Hallinan, A. Corsi, et al. A mildly relativistic wide-angle outflow in the neutron-star merger event GW170817. Nature, 554(7691):207–210, February 2018d.

R. Morgan, M. Soares-Santos, J. Annis, K. Herner, A. Garcia, et al. Constraints on the Physical Properties of GW190814 through Simulations Based on DECam Follow-up Observations by the Dark Energy Survey. ApJ, 901(1):83, September 2020.

Ko Nakamura, Shunsaku Horiuchi, Masaomi Tanaka, Kazuhiro Hayama, Tomoya Takiwaki, and Kei Kotake. Multimessenger signals of long-term core-collapse supernova simulations: synergetic observation strategies. MNRAS, 461(3):3296–3313, September 2016.

Ehud Nakar and Tsvi Piran. Detectable radio flares following gravitational waves from mergers of binary neutron stars. Nature, 478(7367):82–84, October 2011.

Engineering National Academies of Sciences and Medicine. *Pathways to Discovery in Astronomy and Astrophysics for the 2020s*. 2021.

Vsevolod Nedora, Sebastiano Bernuzzi, David Radice, Boris Daszuta, Andrea Endrizzi, et al. Numerical Relativity Simulations of the Neutron Star Merger GW170817: Long-term Remnant Evolutions, Winds, Remnant Disks, and Nucleosynthesis. ApJ, 906(2):98, January 2021a.

Vsevolod Nedora, David Radice, Sebastiano Bernuzzi, Albino Perego, Boris Daszuta, et al. Dynamical ejecta synchrotron emission as possible contributor to the rebrightening of GRB170817A. *arXiv e-prints*, art. arXiv:2104.04537, April 2021b.

Vsevolod Nedora, David Radice, Sebastiano Bernuzzi, Albino Perego, Boris Daszuta, et al. Dynamical ejecta synchrotron emission as a possible contributor to the changing behaviour of GRB170817A afterglow. MNRAS, 506(4):5908–5915, October 2021c.

Melania Nynka, John J. Ruan, Daryl Haggard, and Phil A. Evans. Fading of the X-Ray Afterglow of Neutron Star Merger GW170817/GRB 170817A at 260 Days. ApJ, 862(2):L19, August 2018.

S. R. Oates and Swift Team. LIGO/Virgo S191213g: Swift UVOT/XRT observations of Pan-STARRS1 candidate: PS19hgw. *GRB Coordinates Network*, 26501:1, December 2019.

B. O'Connor and E. Troja. Continued Chandra monitoring of GW170817 at 4.8 yr post-merger. *GRB Coordinates Network*, 32065:1, May 2022.

E. O. Ofek, D. A. Frail, B. Breslauer, S. R. Kulkarni, P. Chandra, et al. A Very Large Array Search for 5 GHz Radio Transients and Variables at Low Galactic Latitudes. ApJ, 740(2):65, October 2011.

William S. Paciesas, Charles A. Meegan, Andreas von Kienlin, P. N. Bhat, Elisabetta Bissaldi, et al. The Fermi GBM Gamma-Ray Burst Catalog: The First Two Years. ApJS, 199(1):18, March 2012.

K. L. Page, P. A. Evans, A. Tohuvavohu, J. A. Kennea, N. J. Klingler, et al. Swift-XRT follow-up of gravitational wave triggers during the third aLIGO/Virgo observing run. MNRAS, 499(3):3459–3480, December 2020.

Nipuni Palliyaguru and Alessandra Corsi. The double-peaked radio light curve of supernova PTF11qcj- Evidence for an off-axis jet? In *American Astronomical Society Meeting Abstracts #233*, volume 233 of *American Astronomical Society Meeting Abstracts*, page 258.09, Jan 2019.

Nipuni T. Palliyaguru, Alessandra Corsi, Dale A. Frail, Jozsef Vinkó, J. Craig Wheeler, et al. The Double-peaked Radio Light Curve of Supernova PTF11qcj. ApJ, 872(2):201, February 2019.

Jaehong Park, Damiano Caprioli, and Anatoly Spitkovsky. Simultaneous Acceleration of Protons and Electrons at Nonrelativistic Quasiparallel Collisionless Shocks. Phys. Rev. Lett., 114(8):085003, February 2015.

D. A. Perley, C. M. Copperwheat, and Growth Collaboration. LIGO/Virgo S191213g: Liverpool Telescope spectroscopy of ZTF candidates. *GRB Coordinates Network*, 26426:1, December 2019.

Daniel A. Perley, Christoffer Fremling, Jesper Sollerman, Adam A. Miller, Aishwarya S. Dahiwale, et al. The Zwicky Transient Facility Bright Transient Survey. II. A Public Statistical Sample for Exploring Supernova Demographics. ApJ, 904 (1):35, November 2020.

R. A. Perley and B. J. Butler. An Accurate Flux Density Scale from 50 MHz to 50 GHz. ApJS, 230(1):7, May 2017.

Rosalba Perna, Davide Lazzati, and Will Farr. Limits on Electromagnetic Counterparts of Gravitational-wave-detected Binary Black Hole Mergers. ApJ, 875(1):49, April 2019.

E. Pian, P. D'Avanzo, S. Benetti, M. Branchesi, E. Brocato, et al. Spectroscopic identification of r-process nucleosynthesis in a double neutron-star merger. Nature, 551(7678):67–70, November 2017.

Tsvi Piran. The physics of gamma-ray bursts. *Reviews of Modern Physics*, 76(4): 1143–1210, October 2004.

Tsvi Piran, Ehud Nakar, and Stephan Rosswog. The electromagnetic signals of compact binary mergers. MNRAS, 430(3):2121–2136, April 2013.

E. Polisensky, W. M. Lane, S. D. Hyman, N. E. Kassim, S. Giacintucci, et al. Exploring the Transient Radio Sky with VLITE: Early Results. ApJ, 832(1):60, November 2016.

Emil Polisensky, Emily Richards, Tracy Clarke, Wendy Peters, and Namir Kassim. The VLITE Database Pipeline. In Peter J. Teuben, Marc W. Pound, Brian A. Thomas, and Elizabeth M. Warner, editors, *Astronomical Data Analysis Software and Systems XXVII*, volume 523 of *Astronomical Society of the Pacific Conference Series*, page 4, October 2019.

David Pooley, J. Craig Wheeler, Jozsef Vinkó, Vikram V. Dwarkadas, Tamas Szalai, et al. Interaction of SN Ib 2004dk with a Previously Expelled Envelope. ApJ, 883 (2):120, October 2019.

David Radice, Albino Perego, Kenta Hotokezaka, Steven A. Fromm, Sebastiano Bernuzzi, and Luke F. Roberts. Binary Neutron Star Mergers: Mass Ejection, Electromagnetic Counterparts, and Nucleosynthesis. ApJ, 869(2):130, December 2018.

David Reitze, Rana X. Adhikari, Stefan Ballmer, Barry Barish, Lisa Barsotti, et al. Cosmic Explorer: The U.S. Contribution to Gravitational-Wave Astronomy beyond LIGO. In *Bulletin of the American Astronomical Society*, volume 51, page 35, September 2019a.

David Reitze, LIGO Laboratory: California Institute of Technology, LIGO Laboratory: Massachusetts Institute of Technology, LIGO Hanford Observatory, and LIGO Livingston Observatory. The US Program in Ground-Based Gravitational Wave Science: Contribution from the LIGO Laboratory. BAAS, 51(3):141, May 2019b.

Jia Ren, Da-Bin Lin, Lu-Lu Zhang, Kai Wang, Xiao-Yan Li, et al. Constraining the Jet Launching Time of GRB 170817A by Utilizing the Baryon Loading. ApJ, 901 (2):L26, October 2020.

L. E. Rivera Sandoval, T. J. Maccarone, A. Corsi, P. J. Brown, D. Pooley, and J. C. Wheeler. X-ray Swift observations of SN 2018cow. MNRAS, 480(1):L146–L150, October 2018.

S. Rosswog, U. Feindt, O. Korobkin, M. R. Wu, J. Sollerman, et al. Detectability of compact binary merger macronovae. *Classical and Quantum Gravity*, 34(10): 104001, May 2017.

George B. Rybicki and Alan P. Lightman. *Radiative processes in astrophysics*. 1979.

P. Salas, F. E. Bauer, C. Stockdale, and J. L. Prieto. SN 2007bg: the complex circumstellar medium around one of the most radio-luminous broad-lined Type Ic supernovae. MNRAS, 428(2):1207–1217, January 2013.

Re'em Sari, Tsvi Piran, and Ramesh Narayan. Spectra and Light Curves of Gamma-Ray Burst Afterglows. ApJ, 497(1):L17–L20, Apr 1998.

V. Shenoy, E. Aarthy, V. Bhalerao, D. Bhattacharya, A. R. Rao, et al. LIGO/Virgo S191213g: AstroSat CZTI upper limits. *GRB Coordinates Network*, 26425:1, December 2019.

N. Singh, T. Bulik, K. Belczynski, and A. Askar. Exploring compact binary populations with the Einstein Telescope. *arXiv e-prints*, art. arXiv:2112.04058, December 2021.

L. Sironi, U. Keshet, and M. Lemoine. Relativistic Shocks: Particle Acceleration and Magnetization. Space Sci. Rev., 191(1-4):519–544, October 2015.

K. W. Smith, S. J. Smartt, D. R. Young, S. Srivastav, J. Gillanders, et al. LIGO/Virgo S191213g: Pan-STARRS1 previous detections of ZTF19acykzsk. *GRB Coordinates Network*, 26430:1, December 2019.

A. M. Soderberg, S. R. Kulkarni, E. Berger, R. A. Chevalier, D. A. Frail, et al. The Radio and X-Ray-Luminous Type Ibc Supernova 2003L. ApJ, 621(2):908–920, Mar 2005.

A. M. Soderberg, R. A. Chevalier, S. R. Kulkarni, and D. A. Frail. The Radio and X-Ray Luminous SN 2003bg and the Circumstellar Density Variations around Radio Supernovae. ApJ, 651(2):1005–1018, November 2006.

Robert Stein, Simeon Reusch, Dan Perley, Igor Andreoni, Michael Coughlin, et al. LIGO/Virgo S191213g: Additional candidates from the Zwicky Transient Facility. *GRB Coordinates Network*, 26437:1, December 2019.

C. J. Stockdale, M. S. Heim, C. M. Vandrevala, F. E. Bauer, S. D. van Dyk, et al. Supernovae 1996aq and 2004dk. *Central Bureau Electronic Telegrams*, 1714:1, March 2009.

Ian B. Strong, Ray W. Klebesadel, and Roy A. Olson. A Preliminary Catalog of Transient Cosmic Gamma-Ray Sources Observed by the VELA Satellites. ApJ, 188:L1, February 1974.

S. Sugita, M. Serino, N. Kawai, H. Negoro, M. Nakajima, et al. LIGO/Virgo S191213g: Coverage and upper limits from MAXI/GSC observations. *GRB Coordinates Network*, 26403:1, December 2019.

G. Swarup. Giant metrewave radio telescope (GMRT) - Scientific objectives and design aspects. *Indian Journal of Radio and Space Physics*, 19:493–505, December 1990.

John D. Swinbank, Tim D. Staley, Gijs J. Molenaar, Evert Rol, Antonia Rowlinson, et al. The LOFAR Transients Pipeline. *Astronomy and Computing*, 11:25–48, June 2015.

A. L. Thakur, S. Dichiara, E. Troja, E. A. Chase, R. Sánchez-Ramírez, et al. A search for optical and near-infrared counterparts of the compact binary merger GW190814. MNRAS, 499(3):3868–3883, December 2020.

The LIGO Scientific Collaboration, the Virgo Collaboration, the KAGRA Collaboration, R. Abbott, T. D. Abbott, et al. GWTC-3: Compact Binary Coalescences Observed by LIGO and Virgo During the Second Part of the Third Observing Run. *arXiv e-prints*, art. arXiv:2111.03606, November 2021.

E. Troja, L. Piro, H. van Eerten, R. T. Wollaeger, M. Im, et al. The X-ray counterpart to the gravitational-wave event GW170817. Nature, 551(7678):71–74, November 2017.

E. Troja, L. Piro, G. Ryan, B. O'Connor, H. van Eerten, and T. Sakamoto. Long-lasting X-ray emission from GW170817 detected by Chandra. *GRB Coordinates Network*, 29038:1, December 2020.

E. Troja, B. O'Connor, G. Ryan, L. Piro, R. Ricci, et al. Accurate flux calibration of GW170817: is the X-ray counterpart on the rise? MNRAS, 510(2):1902–1909, February 2022.

A. F. Valeev, N. Castro-Rodriguez, and a larger Collaboration. LIGO/Virgo S191213g: AT2019wxt 10.4m GTC further spectroscopy. *GRB Coordinates Network*, 26591:1, December 2019.

P. Vallely. LIGO/Virgo S191213g: LBT spectrum of AT2019wxt (PS19hgw) reveals a type IIb supernova. *GRB Coordinates Network*, 26508:1, December 2019.

A. J. van der Horst, A. Kamble, L. Resmi, R. A. M. J. Wijers, D. Bhattacharya, et al. Detailed study of the GRB 030329 radio afterglow deep into the non-relativistic phase. A&A, 480(1):35–43, March 2008.

Gustaaf van Moorsel, Athol Kemball, and Eric Greisen. AIPS Developments in the Nineties. In George H. Jacoby and Jeannette Barnes, editors, *Astronomical Data Analysis Software and Systems V*, volume 101 of *Astronomical Society of the Pacific Conference Series*, page 37, January 1996.

F. Verrecchia, C. Casentini, M. Tavani, M. Cardillo, G. Piano, et al. LIGO/Virgo S191213g: upper limits from AGILE-MCAL observations. *GRB Coordinates Network*, 26407:1, December 2019.

Nicholas Vieira, John J. Ruan, Daryl Haggard, Maria R. Drout, Melania C. Nynka, et al. A Deep CFHT Optical Search for a Counterpart to the Possible Neutron Star-Black Hole Merger GW190814. ApJ, 895(2):96, June 2020.

C. Vogl, A. Floers, S. Taubenberger, W. Hillebrandt, and S. Suyu. LIGO/Virgo S191213g: VLT spectrum of AT2019wxt (PS19hgw) - a probable Ib supernova. *GRB Coordinates Network*, 26504:1, December 2019.

A. M. Watson, N. R. Butler, W. H. Lee, R. L. Becerra, M. Pereyra, et al. Limits on the electromagnetic counterpart to S190814bv. MNRAS, 492(4):5916–5921, March 2020.

Kurt W. Weiler, Nino Panagia, and Richard A. Sramek. Radio Emission from Supernovae. II. SN 1986J: A Different Kind of Type II. ApJ, 364:611, December 1990.

Kurt W. Weiler, Christopher L. Williams, Nino Panagia, Christopher J. Stockdale, Matthew T. Kelley, et al. Long-Term Radio Monitoring of SN 1993J. ApJ, 671(2): 1959–1980, December 2007.

Sarah Wellons, Alicia M. Soderberg, and Roger A. Chevalier. Radio Observations Reveal Unusual Circumstellar Environments for Some Type Ibc Supernova Progenitors. ApJ, 752(1):17, Jun 2012.

C. A. Wilson-Hodge, Fermi-GBM Team, and GBM-LIGO/Virgo Group. LIGO/Virgo S191213g: Upper limits from Fermi-GBM Observations. *GRB Coordinates Network*, 26409:1, December 2019.

Sung-Chul Yoon and Matteo Cantiello. Evolution of Massive Stars with Pulsation-driven Superwinds During the Red Supergiant Phase. ApJ, 717(1):L62–L65, July 2010.

Z. B. Zhang and C. S. Choi. An analysis of the durations of Swift gamma-ray bursts. A&A, 484(2):293–297, June 2008.

J. T. L. Zwart, R. W. Barker, P. Biddulph, D. Bly, R. C. Boysen, et al. The Arcminute Microkelvin Imager. MNRAS, 391(4):1545–1558, December 2008.

Appendices

APPENDIX A
SYNCHROTRON AFTERGLOW RADIATION

A.1 Synchrotron emission from accelerated charges

Consider a charge q of mass m moving with a velocity $\vec{v}$ in a magnetic field. The relativistic equations describing the motion of such a charge (in Gaussian units) are (See Lorentz four force (Rybicki and Lightman, 1979)):

$$\frac{d(\gamma m\vec{v})}{dt} = \frac{q}{c}(\vec{v} \times \vec{B})$$

$$\frac{d(\gamma mc^2)}{dt} = q\vec{v} \cdot \vec{E} = 0$$

The second equation is zero as there is no $\vec{E}$ in our problem. This implies that γ = constant or that $|\vec{v}|^2$ = constant. Now, $\vec{v}$ can be broken up into two components, $\vec{v}_\parallel$ parallel to $\vec{B}$ and $\vec{v}_\perp$ perpendicular to $\vec{B}$. This in turn implies :

$$\frac{d\vec{v}_\parallel}{dt} = 0 \qquad , \qquad m\gamma\frac{d\vec{v}_\perp}{dt} = \frac{q}{c}(\vec{v}_\perp \times \vec{B})$$

We have already seen that $|\vec{v}|$ is constant and from the first equation above, $\vec{v}_\parallel$ is a constant. Therefore, we have $|\vec{v}_\perp|$ is a constant, i.e., the charge moves in a helix of constant radius. The frequency of gyration is given by :

$$\omega_B = \frac{qB}{\gamma mc} \tag{A.1}$$

and the acceleration is perpendicular to velocity with a magnitude of $a_\perp = \omega_B v_\perp$.

We have seen in class, that we can obtain the following radiated fields from the Liénard–Wiechert potentials (see Jackson (1998), Chapter 14):

$$\vec{E}(\vec{r},t) = \frac{q}{c}\left[\frac{\vec{n}}{(1-\vec{\beta}\cdot\vec{n})^3 R} \times \left((\vec{n}-\vec{\beta}) \times \dot{\vec{\beta}}\right)\right] + \mathscr{O}\left(\frac{1}{R^2}\right) \tag{A.2}$$

$$\vec{B}(\vec{r},t) = \left[\vec{n} \times \vec{E}(\vec{r},t)\right] \tag{A.3}$$

where $\vec{R}(t') = \vec{r} - \vec{r}_0(t')$, $\vec{n} = \vec{R}/R$ and $\vec{\beta} = \vec{v}/c$.

A.1.1 Classical cyclotron

For non-relativistic particles, $|\vec{\beta}| << 1$ and therefore the magnitude of the fields from A.2 above become (Rybicki and Lightman, 1979)

$$|\vec{E}_{rad}| = |\vec{B}_{rad}| = \frac{q|\dot{\vec{v}}|}{Rc^2} sin\Psi \tag{A.4}$$

where Ψ is the angle between $\dot{\vec{v}}(= \vec{a})$ and $\vec{n}$. This in turn gives us the radiation pattern and hence the power radiated

$$\frac{dP}{d\Omega} = \frac{q^2a^2}{4\pi c^3} sin^2\Psi \implies P = \frac{2q^2a^2}{3c^3} \tag{A.5}$$

From the above discussion on the motion of the charge, we already have $a_\perp$ in terms of $\omega_B \approx qB/mc$ (as for the non-relativistic case $\gamma \to 1$) which we can plug in to obtain the total power radiated by a non-relativistic particle moving in a constant B field (Larmor Power) :

$$\boxed{P = \frac{2q^4c}{3mc^4}\Big(\frac{v_\perp}{c}\Big)^2 B^2} \tag{A.6}$$

and is **emitted solely at the frequency $\boldsymbol{\omega_B}$** (Rybicki and Lightman, 1979).

A.1.2 Relativistic generalization

Let us now see how to generalize what we saw above to a relativistic case. We defined the following four vectors in class already : four-velocity - $\eta^\mu = (\gamma c, \gamma\vec{v})$; four-momentum - $P^\mu = m_0\eta^\mu$; and four-acceleration $a^\mu = d\eta^\mu/d\tau$. It can be shown that this four-acceleration and four-velocity are orthogonal (Rybicki and Lightman, 1979):

$$a^\mu\eta_\mu = \frac{d\eta^\mu}{d\tau}\eta_\mu = \frac{1}{2}\frac{d}{d\tau}\Big(\eta^\mu\eta_\mu\Big) = \frac{1}{2}\frac{d}{d\tau}(-c^2) = 0$$

So, in the rest from of the particle ($\eta^\mu = (c, \vec{0})$), we have $a'_0 = 0$ and $|\vec{a'}|^2 = \vec{a'}\cdot\vec{a'}$ (only the spatial components). So, the Larmor Power (See A.5) modifies to (See Jackson

(1998) Section 14.2. It can be proven that P is a Lorentz invariant, and hence has the form):

$$P' = \frac{2q^2}{3m^2c^3}\left(\frac{dP_\mu}{d\tau}\frac{dP^\mu}{d\tau}\right) = \frac{2q^2}{3c^3}\vec{a'}\cdot\vec{a'} \tag{A.7}$$

Going to the inertial frame (primed coordinates are in particle frame):

$$a'_\perp = \gamma^2 a_\perp \implies P = \frac{2q^2}{3c^3}\gamma^4 a_\perp^2 \tag{A.8}$$

Substituting the value of $a_\perp$ from A.1, scattering cross-section $\sigma_T = 8\pi q^4/m^2c^4$ using an isotropic distribution of velocities $< \beta_\perp^2 >= 2\beta^2/3$ with the approximation $\beta \to 1$, the power emitted can be written as a function of γ (Sari et al., 1998):

$$\boxed{P(\gamma) = \frac{4}{3}\sigma_T c\gamma^2\frac{B^2}{8\pi}} \tag{A.9}$$

A.2 Application to GRB afterglows

Delayed electromagnetic emission seen from a merger remnant or other cataclysmic events like Supernovae is known as afterglow. It has been seen that emission of this type in radio wavelengths can be explained by synchrotron emission from a slowing down relativistic shell that collides with the external medium. Here, we will look at the broad band spectrum and light curve of synchrotron radiation from a power-law Lorentz factor distribution of electrons in the relativistic shock (Sari et al., 1998).

A.2.1 Assumptions and predictions

A relativistic shell propagates through a cold, uniform medium of particle density n. If the shock waves have a Lorentz factor of γ with respect to the observer frame, the number density of the particles behind the shock wave can be written as $4\gamma n$ (this can be shown using $p = 0$ for the cold fluid and the ultra-relativistic equation of state implies the pressure behind the shock is $p = u/3$, u is the energy density. See Blandford and McKee (1976); Rybicki and Lightman (1979) and hence the energy density behind the shock is $4\gamma^2 n m_p c^2$ (as there is possibility of particle creation, n must be the density of particles that are conserved like baryons, hence the use of m_p(Blandford and McKee, 1976). Assuming that electrons in the shock are distributed in a powerlaw distribution of their Lorentz factor γ_e with respect to the shocked fluid ie. $N(\gamma_e)d\gamma_e \propto \gamma_e^{-p}d\gamma_e$ for $\gamma_e \geq \gamma_m$ some minimum Lorentz factor given by :

$$\gamma_m = \epsilon_e\Big(\frac{p-2}{p-1}\Big)\frac{m_p}{m_e}\gamma$$

where ϵ_e is the fraction of the shock energy with the electrons and $p > 2$ to keep the energy of the electrons finite. Let ϵ_B be the fraction of the shock energy density in the magnetic field behind the shock. Therefore, this energy density and hence the magnetic field strength (*assumed to be perpendicular to the shock wave*) can be written as :

$$u_B = \frac{1}{8\pi}|\vec{B}|^2 = \epsilon_B 4\gamma^2 n m_p c^2 \implies B = (32\pi m_p \epsilon_B n)^{1/2}\gamma c$$

The Lorentz factor of the shock with respect to the observer is γ and we have seen in that class that the magnetic field transforms as $B'_\perp = \gamma B$. Now, we can go ahead and write down the radiation power (in the rest frame of the observer) as follows (see A.9):

$$P(\gamma_e) = \frac{4}{3}\sigma_T c\gamma^2\gamma_e^2\frac{B^2}{8\pi}$$

The observer will see a pulse for a duration much smaller than the gyration period (see A.1 and period= $2\pi/\omega_B$) and the **spectrum will be spread over a much broader region around the gyration frequency, unlike the monochromatic cyclotron emission**.

Power per frequency gives more information than the total power. The critical frequency ω_c beyond which there is negligible radiation at any angle is defined as (See Jackson (1998) section 14.6):

$$\omega_c = \frac{3}{2}\gamma_e^3\omega_B \implies \nu(\gamma_e) = \frac{\omega_c}{2\pi} = \gamma\gamma_e^2\frac{q_e B}{2\pi m_e c}$$

The spectral power, P_ν (Power per frequency), varies as $\nu^{1/3}$ for $\nu < \nu(\gamma_e)$ and cuts off exponentially for $\nu > \nu(\gamma_e)$ (Rybicki and Lightman, 1979). The maximum value of P_ν is

$$P_{\nu,max} \approx \frac{P(\gamma_e)}{\nu(\gamma_e)} = \frac{m_e c^2 \sigma_T}{3q_e}\gamma B.$$

P_ν describes the emitted spectrum when the electron does not lose a large fraction of its energy to radiation, which requires γ_e to be less than a critical value γ_c given by:

$$\gamma_c = \frac{6\pi m_e c}{\sigma_T \gamma B^2 t} = \frac{3m_e}{16\epsilon_B \sigma_T m_p c}\frac{1}{t\gamma^3 n}.$$

Therefore, the instantaneous flux density at the observer consists of three segments:

$$F_\nu = \begin{cases} (\nu/\nu_m)^{1/3} F_{\nu,max} & \nu < \nu_m \\ (\nu/\nu_m)^{-(p-1)/2} F_{\nu,max} & \nu_m < \nu < \nu_c, \\ (\nu_c/\nu_m)^{-(p-1)/2}\,(\nu/\nu_c)^{-p/2}\,F_{\nu,max} & \nu > \nu_c \end{cases}$$

where $\nu_m \equiv \nu(\gamma_m)$, $\nu_c \equiv \nu(\gamma_c)$, $F_{\nu,max} \equiv N_e P_{\nu,max}/4\pi D^2$ (N_e = total number of electrons and D = distance to the source).

At a given frequency, ν, many of the quantities discussed above, like ν_c, ν_m and $N_e P_{\nu,max}$, change with time. Let us assume a spherical shock of radius $R(t)$ propagating in a medium of density n. Then:

$$N_e = n\frac{4}{3}\pi R^3$$

Here, we will consider the case where $\epsilon_e << 1$ or $\gamma_c >> \gamma_m$, an adiabatic evolution. The constant energy of the spherical shock is (Blandford and McKee, 1976; Sari et al., 1998):

$$E = \frac{16}{17}\pi\gamma^2 R^3 n m_p c^2$$

Define $L = [17M/(16\pi m_p n)]^{1/3}$, is the radius at which the mass swept up from the external medium equals the initial mass M of the ejecta. $M = E/\gamma_0 c^2$, where γ_0 is the initial Lorentz factor of the ejecta. Therefore, we can calculate observed time t, $R(t)$ and $\gamma(t)$ as follows (Sari et al., 1998):

$$t \cong \frac{R}{4\gamma^2 c},$$

$$R(t) \cong \Big(\frac{17Et}{4\pi m_p nc}\Big)^{1/4},$$

$$\gamma(t) \cong \Big(\frac{17E}{1024\pi n m_p c^5 t^3}\Big)^{1/8}.$$

With these values, we can then calculate the following values that can be used to obtain the functional form of the light curve:

$$\begin{aligned} \nu_c &= 2.7 \times 10^{12} \epsilon_B^{-3/2} E_{52}^{-1/2} n_1^{-1} t_d^{-1/2} \text{ Hz}, \\ \nu_m &= 5.7 \times 10^{14} \epsilon_B^{1/2} \epsilon_e^2 E_{52}^{1/2} t_d^{-3/2} \text{ Hz}, \\ F_{\nu,max} &= 1.1 \times 10^5 \epsilon_B^{1/2} E_{52} n_1^{1/2} D_{28}^{-2}\ \mu\text{Jy}, \end{aligned}$$

where t_d is the time in days, $E_{52} = E/10^{52}$ ergs, n_1 is n in units of cm^{-3} and $D_{28} = D/10^{28}$ cm.

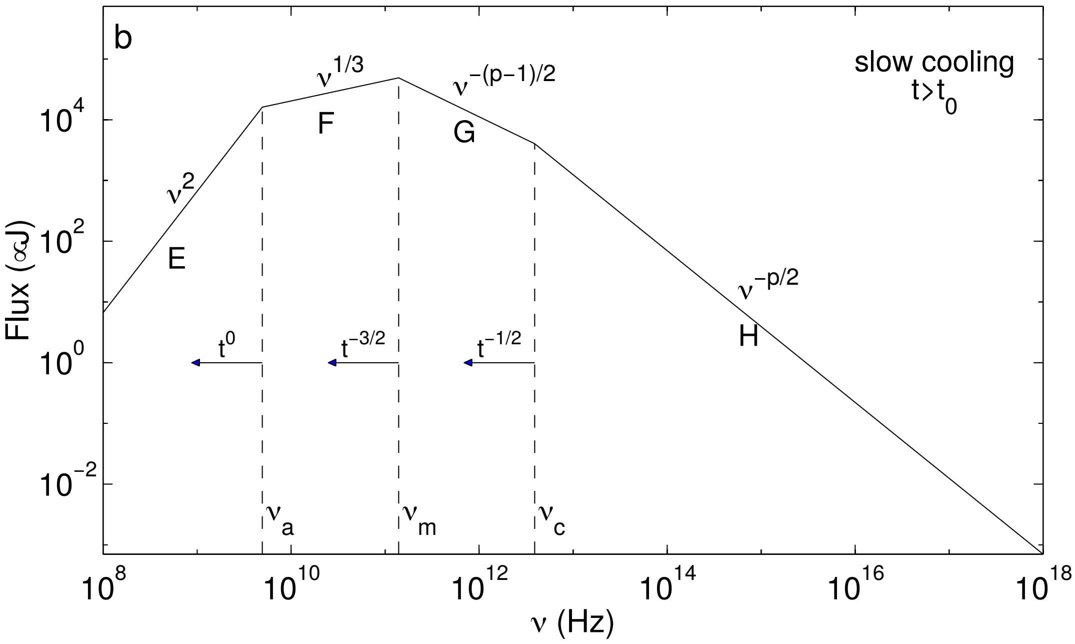

Figure A.1. Synchrotron emission spectrum assuming adiabatic expansion for later times $t > t_0$. Figure from Sari et al. (1998).

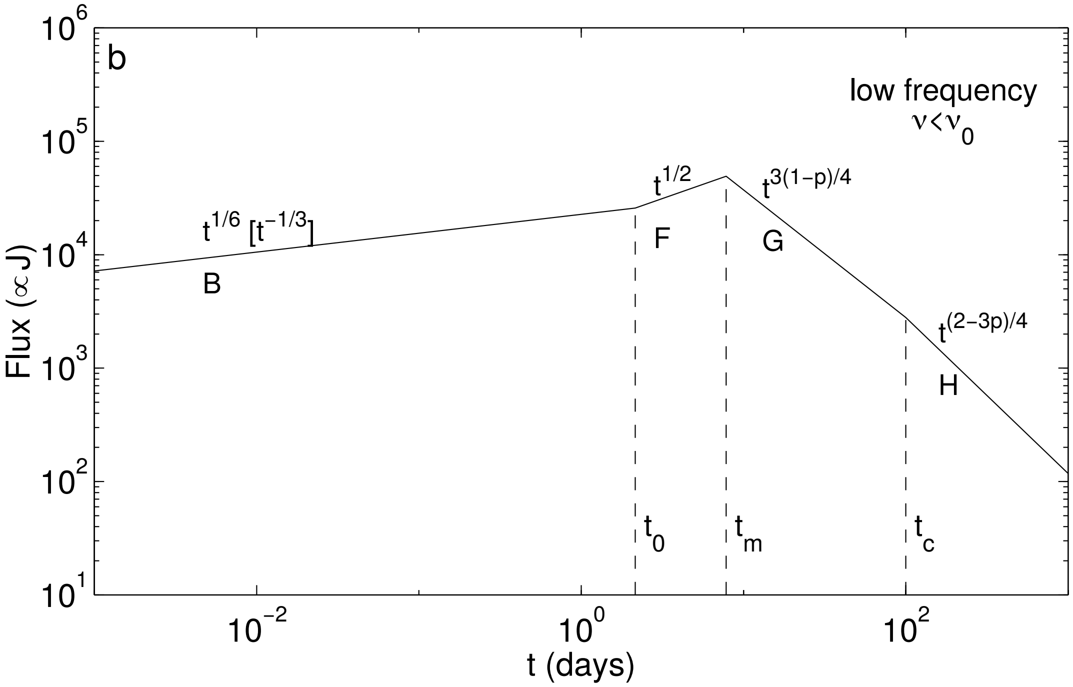

Figure A.2. The afterglow light curve for low frequencies. Figure from Sari et al. (1998). Ignore the time dependence in square brackets at early times for our discussion.

APPENDIX B
GW170817 SMOOTH-BROKEN POWER LAW MODEL $1\,\sigma$ ERROR REGION CALCULATION

The jet+cocoon emission can be modeled by the smooth-broken power law model (see Makhathini et al., 2021, and references therein) where, the flux density at a time t and at an observation frequency ν is given by:

$$F(t,\nu) = 2^{1/s}\left(\frac{\nu}{3\,\mathrm{GHz}}\right)^{\beta} F_p \left[\left(\frac{t}{t_p}\right)^{-s\alpha_1} + \left(\frac{t}{t_p}\right)^{-s\alpha_2}\right]^{-1/s} \tag{B.1}$$

where F_p is the peak flux density, t_p is the epoch at which the light curve peaks, s is the smoothness parameter, β is the spectral power law index, α_1 and α_2 represent the power-law index of rise and decay of the light curve.

Using the notation that δQ is the error in the quantity Q in the Equation B.1, we can derive the error on the flux density in terms of the parameters F_p, t_p, s, β, α_1 and α_2 as

$$\begin{aligned}\delta F(t,\nu) = \Bigg\{ &\left(\left|\frac{dF(t,\nu)}{dF_p}\right|\delta F_p\right)^2 + \left(\left|\frac{dF(t,\nu)}{dt_p}\right|\delta t_p\right)^2 + \left(\left|\frac{dF(t,\nu)}{d\alpha_1}\right|\delta \alpha_1\right)^2 \\ &+ \left(\left|\frac{dF(t,\nu)}{d\alpha_2}\right|\delta \alpha_2\right)^2 + \left(\left|\frac{dF(t,\nu)}{ds}\right|\delta s\right)^2 + \left(\left|\frac{dF(t,\nu)}{d\beta}\right|\delta \beta\right)^2 \Bigg\}^{\frac{1}{2}}\end{aligned} \tag{B.2}$$

where

$$\left|\frac{dF(t,\nu)}{dF_p}\right|\delta F_p = \delta F_p \left|\frac{F(t,\nu)}{F_p}\right| \tag{B.3}$$

$$\begin{aligned}\left|\frac{dF(t,\nu)}{dt_p}\right|\delta t_p = \delta t_p \Bigg| &2^{1/s}\left(\frac{\nu}{3\,\mathrm{GHz}}\right)^{\beta} F_p \left(\frac{-1}{s}\right)\left[\left(\frac{t}{t_p}\right)^{-s\alpha_1} + \left(\frac{t}{t_p}\right)^{-s\alpha_2}\right]^{((-1/s)-1)} \\ &\times \left[\frac{s\alpha_1}{t_p}\left(\frac{t}{t_p}\right)^{-s\alpha_1} + \frac{s\alpha_2}{t_p}\left(\frac{t}{t_p}\right)^{-s\alpha_2}\right]\Bigg|\end{aligned} \tag{B.4}$$

$$\begin{aligned}\left|\frac{dF(t,\nu)}{d\alpha_1}\right|\delta\alpha_1 = \delta\alpha_1 \Bigg| & 2^{1/s}\left(\frac{\nu}{3\,\mathrm{GHz}}\right)^{\beta} F_p\left(\frac{-1}{s}\right)\left[\left(\frac{t}{t_p}\right)^{-s\alpha_1}+\left(\frac{t}{t_p}\right)^{-s\alpha_2}\right]^{((-1/s)-1)} \\ & \times\left[\left(\frac{t}{t_p}\right)^{-s\alpha_1}\ln\left(\frac{t}{t_p}\right)(-s)\right]\Bigg|\end{aligned} \tag{B.5}$$

$$\begin{aligned}\left|\frac{dF(t,\nu)}{d\alpha_2}\right|\delta\alpha_2 = \delta\alpha_2 \Bigg| & 2^{1/s}\left(\frac{\nu}{3\,\mathrm{GHz}}\right)^{\beta} F_p\left(\frac{-1}{s}\right)\left[\left(\frac{t}{t_p}\right)^{-s\alpha_1}+\left(\frac{t}{t_p}\right)^{-s\alpha_2}\right]^{((-1/s)-1)} \\ & \times\left[\left(\frac{t}{t_p}\right)^{-s\alpha_2}\ln\left(\frac{t}{t_p}\right)(-s)\right]\Bigg|\end{aligned} \tag{B.6}$$

$$\begin{aligned}\left|\frac{dF(t,\nu)}{ds}\right|\delta s = \delta s \Bigg| & \left\{\frac{-1}{s^2}\ln(2)F(t,\nu)\right\} \\ & + \Bigg\{F(t,\nu)\Bigg[\left(\frac{1}{s^2}\ln\left(\left(\frac{t}{t_p}\right)^{-s\alpha_1}+\left(\frac{t}{t_p}\right)^{-s\alpha_2}\right)\right) \\ & - \frac{\left(\left(\frac{t}{t_p}\right)^{-s\alpha_1}\ln\left(\frac{t}{t_p}\right)(-\alpha_1)+\left(\frac{t}{t_p}\right)^{-s\alpha_2}\ln\left(\frac{t}{t_p}\right)(-\alpha_2)\right)}{s\left(\left(\frac{t}{t_p}\right)^{-s\alpha_1}+\left(\frac{t}{t_p}\right)^{-s\alpha_2}\right)}\Bigg]\Bigg\}\Bigg|\end{aligned}$$

and finally

$$\left|\frac{dF(t,\nu)}{\beta}\right|\delta\beta = \delta\beta\left|F(t,\nu)\ln\left(\frac{\nu}{3\,\mathrm{GHz}}\right)\right| \tag{B.7}$$